Syracuse University

SURFACE at Syracuse University

Dissertations - ALL

SURFACE at Syracuse University

5-12-2024

Directional Dopant Migration by ‘Atomic Trapping’ in Core/multi-shell Quantum Dots

Chun Chu
Syracuse University

Follow this and additional works at: https://surface.syr.edu/etd

Part of the Chemistry Commons

Recommended Citation

Chu, Chun, "Directional Dopant Migration by ‘Atomic Trapping’ in Core/multi-shell Quantum Dots" (2024). *Dissertations - ALL*. 1952.
https://surface.syr.edu/etd/1952

This Dissertation is brought to you for free and open access by the SURFACE at Syracuse University at SURFACE at Syracuse University. It has been accepted for inclusion in Dissertations - ALL by an authorized administrator of SURFACE at Syracuse University. For more information, please contact surface@syr.edu.

Abstract

The study of transition metal ion-doped semiconductor nanocrystals (NCs) has attracted increasing attention due to their unique optical, electronic, and magnetic properties which sparked considerable interest towards a wide range of applications in material science, renewable energy and biological systems. Besides the size- and shape-dependent behavior, doped nanomaterials exhibit new and/or enhanced optical properties, which are sensitive to the dopant location or dopant distribution throughout the solid crystal lattice. Our work primarily focuses on understanding and elucidating the mechanism of dopant ion migration inside the NCs during post-synthetic treatments, such as shell passivation and high-temperature annealing. Mn(II) dopants migration behavior in Mn(II) doped CdS-based core/shell quantum dots (QDs) and Mn(II) doped ZnSe-based core/shell nanowires were established in the previous work of the Zheng group.

This dissertation will expand the study of dopant migration behavior in semiconductor QDs, specifically, to elucidate the effect of an inserted alloyed layer, with a small cationic size mismatch of dopant ions, for directional dopant migration and diffusion. Our research reveals that the intentionally inserted alloyed layer, with a small cationic size mismatch with Mn(II) dopants, could serve as an atomic "trap" to facilitate the directional dopants migration pathways, including both outward and inward migration in core and shell doped core/multi-shell QDs. The detailed mechanistic study reveals that dopants migration behavior between different tetrahedral sites inside a II-VI group semiconductor lattice are sensitive to the migration temperature and microenvironment within the NCs. Furthermore, a larger Cd(II) substitutional doping site (92 pm) with larger local lattice distortion is critical for efficient Mn dopant (80 pm) trapping and migration. Density functional theory (DFT) calculation reveals a higher energy barrier for a

Mn(II) dopant hopping from the smaller Zn substitutional tetrahedral site (74 pm) as compared to a larger Cd substitutional tetrahedral site in the migration model. The ratio of relative rate constant (k_{ZnS}/k_{CdS}) indicates that the rate of Mn migration is about three-orders of magnitude larger in the CdS lattice compared to ZnS lattice for the temperature range investigated in this study (180 – 230 °C).

Furthermore, we also illustrated the progress and challenges of the Mn(II) dopants migration behavior between the perovskite NCs and the II-VI chalcogenides such as CdS or ZnS NCs. The large difference between the ionic nature of perovskite and covalent nature of chalcogenides, along with their coordination structure (corner-sharing octahedral for perovskite, and core-sharing tetrahedral for metal chalcogenides), as well as the disparate growth kinetics (rapid for perovskite and slow for chalcogenides), pose substantial challenges for the synthesis of heterostructures. Although the optical results indicate that substantial further research is required, these initial steps are promising and paving the way for further exploration of dopant behavior in perovskite based heterostructures.

Directional Dopant Migration by 'Atomic Trapping' in Core/multi-shell Quantum Dots

By,

Chun Chu

B.S., Shenyang University of Chemical Technology, 2003

M.S., Beijing University of Chemical Technology, 2010

M.Phil., Syracuse University, 2021

Dissertation

Submitted in partial fulfillment of the requirements for the degree of

Doctor of Philosophy in Chemistry

Syracuse University

June 2024

Copyright © Chun Chu 2024

All Rights Reserved

Acknowledgements

When I first came to Syracuse University in 2019, I was excited to pursue my Ph.D., but at the same time, I was afraid of living in a different culture and facing uncertainties in totally unfamiliar surroundings. Fortunately, things have improved over time as I joined my favorite department and worked with the kindest people.

I would like to thank my advisor, Professor Weiwei Zheng, for his guidance, support, and continuous teaching throughout the past five years of working in his group. This thesis would not have been possible without Dr. Zheng's knowledge, patience, and motivation. It has been a great honor to be a member of Zheng's group and study in the Chemistry Department at Syracuse University.

I want to express my deepest gratitude to all my committee members, including Professors Quinn Qiao, Mathew M. Maye, John M. Franck, Yan-Yeung Luk, and Xiaoran Hu, for serving on my dissertation committee and for offering their time, knowledge, and valuable suggestions. I would also like to thank Professors Mathew M. Maye and John M. Franck for their continued support of my graduate committee throughout my five years in the Chemistry Department. Additionally, I want to thank Professor Arindam Chakraborty and Professor Robert W. Meulenberg for the fruitful collaborations in my research project.

I would like to thank my colleagues in the Zheng group for their support and collaboration over the past few years. In particular, I want to thank Hanjie Lin and Walker MacSwain for working alongside me and supporting me consistently. I would also like to thank all new lab members, Vanshika, Dylan and Hamid for becoming a great team. I am grateful to the previous members, Dr. Elan Hofman, Dr. Andrew Davis, and Dr. Shuya Li for their kind help in my growth as a chemist. Their support and help have paved the way for my future academic career.

Last but not least, I want to thank my close friends and my family, specifically my parents, sister, brother, and nephews, for their unconditional love and support throughout my life. I love all of you!

Table of Contents

List of Figures

List of Schemes

List of Tables

List of Abbreviations

0D	Zero-dimensional
1D	One-dimensional
2D	Two-dimensional
CB	Conduction band
$Cd(DDTC)_2$	Cadmium diethyldithiocarbamate
$CdCl_2$	Cadmium chloride
$Cd(NO_3)_2 \cdot 4H_2O$	Cadmium nitrate tetrahydrate
CdZnS	Cadmium Zinc sulfide (alloy)
CdO	Cadmium oxide
CdS	Cadmium sulfide
CdSe	Cadmium selenide
CdTe	Cadmium telluride
Cu(I)/Cu(II)	Copper(I)/Copper(II)
Cs_2CO_3	Cesium carbonate
DDT	1-dodecanethiol
DFT	Density functional theory
DMF	N,N-dimethylformamide
DMS	Dilute magnetic semiconductor
DMSO	Dimethyl sulfoxide
E_g	Band gap energy
EDX	Energy-dispersive X-ray spectroscopy
EELS	Electron energy loss spectroscopy
EPR	Electron paramagnetic resonance
EXAFS	Extended X-ray absorption fine structure
FWHM	Full width at half maximum

H-D	Host-Dopant
HBr	Hydrobromic acid
HCl	Hydrochloric acid
HDA	Hexadecylamine
HNO_3	Nitric acid
HR-TEM	High resolution-transmission electron microscopy
ICP-OES	Inductively coupled plasma-optical emission spectrometry
ICP-MS	Inductively coupled plasma-mass spectroscopy
InAs	Indium arsenide
InP	Indium phosphide
InSb	Indium antimonide
$MnBr_2$	Manganese(II) bromide
$MnCl_2$	Manganese(II) chloride
Mn(II)	Manganese(II)
$Mn(CH_3CO_2)_2$	Manganese(II) acetate
$Mn(NO_3)_2 \cdot H_2O$	Manganese nitrate hydrate
Na(DDTC)	Sodium diethyldithiocarbamate
NC	Nanocrystal
nm	Nanometer
NPL	Nanoplatelet
NR	Nanorod
NW	Nanowire
OA	Oleic acid
OAm	Oleylamine
OAm-HX	Oleylammonium halide salt
ODE	1-Octadecene

$PbBr_2$	Lead(II) bromide
$PbCl_2$	Lead (II) chloride
PbS	Lead sulfide
PbSe	Lead selenide
PbTe	Lead telluride
PL	Photoluminescence
PL QY(s)	Photoluminescence quantum yield(s)
QD(s)	Quantum dot(s)
SEM	Scanning electron microscopy
SILAR	Successive ion layer adsorption and reaction
SrS	Strontium sulfide
SSP	Single source precursor
TEM	Transmission electron microscopy
T_b	Temperature boundary
T_d	Tetrahedral
UV	Ultraviolet
VB	Valence band
XAFS	X-ray absorption fine structure
XRD	X-ray diffraction
XPS	X-ray photoelectron spectroscopy
$Zn(DDTC)_2$	Zinc diethyldithiocarbamate
ZnO	Zinc oxide
ZnS	Zinc sulfide
ZnSe	Zinc selenide
ZnTe	Zinc telluride

Chapter 1: Introduction

1. Introduction

Semiconductor nanocrystals (NCs) have attracted widespread interest in the past few decades because of their unique size- and shape-dependent optical, electric, and magnetic properties, which cannot be obtained by their bulk counterparts.[25-29] As early as the 1980s/1990s, the study of semiconductor NCs emerged as an active research field with promising applications in materials science, green energy harvesting, biomedicine, *etc.*[30-42] Doping by the incorporation of impurity ions, named dopants, into semiconductor NCs (*i.e.,* doped NCs) can lead to modified and enhanced optical, electronic, and magnetic properties of the NCs.[43, 44] This is especially true if the dopant location and concentration can be well-controlled. This thesis details the dopant migration behavior in colloidal semiconductor NCs, aiming to precisely manipulate the dopant location by inserting an atomic trap and selecting appropriate doping sites within a core/shell NC lattice.

1.1 Semiconductor Nanocrystals

Semiconductor NCs are extremely tiny crystals with at least one of the three dimensions that range from 1 to 100 nanometers (nm) and constitute a major category of multi-functional materials. (Figure 1.1) These fascinating nanoscale materials display unique and extraordinary optical and electronic properties, which make semiconductor NCs promising candidates for different application areas, such as opto-electronic and spin-based devices,[45, 46] solar cells,[47-51] lasers,[52-55] light emitting diodes,[55-59] biological images,[25, 46, 60] *etc*.

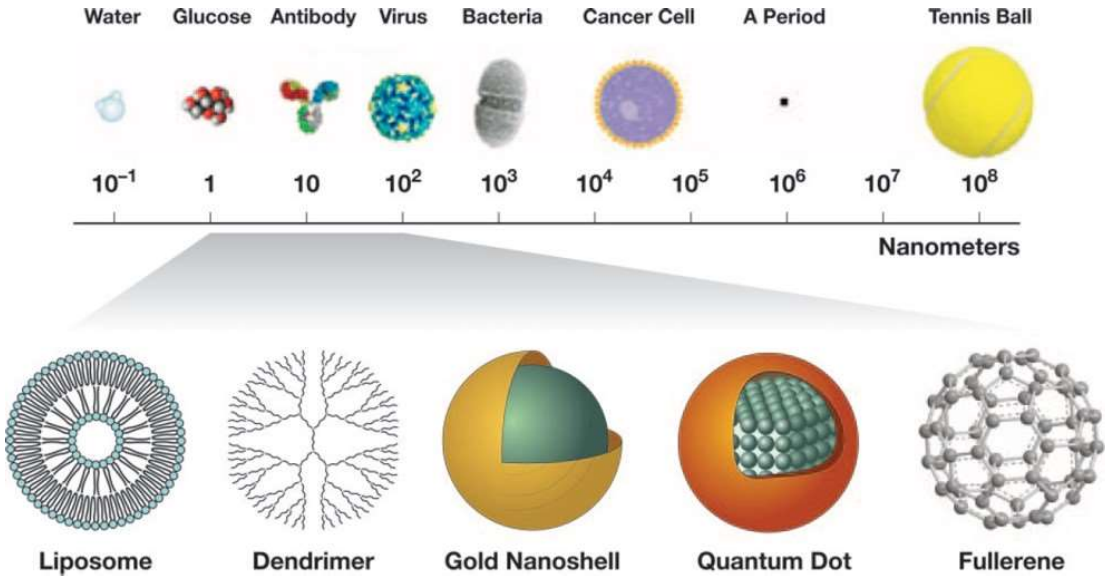

Figure 1.1 The illustration of different range of size for the nanomaterials and common materials.[1]

[1][Repurposed with permission from Society for Leukocyte Biology © 2005]

Semiconductor NCs, based on their shape and morphology, can be classified to zero-dimensional (0D) spherical NCs, one-dimensional (1D) NCs and two-dimensional (2D) NCs in which 0, 1, or 2 axes or axis are confined from 1 to 100 nm, respectively. 0D NCs usually have a spherical shape, as in quantum dots (QDs), or can be found as nanocubes; QDs are most commonly studied and synthesized.[61, 62] 1D rod-shaped NCs usually have elongated structures along c-axis, resembling nanorods (NRs) or nanowires (NWs).[63-66] 2D NCs usually have a flat and plate-like shape, often referred to as nanoplatelets (NPL) or nanosheets.[23, 67, 68] Materials in other shapes, such as tetrapod NCs, are also successfully synthesized and studied by researchers.[6]

1.1.1 Quantum confinement effect in Nanocrystals

As early as 1981, Ekimov and Onushchenko reported nanometer sized CuCl particles with a blue shift of the optical spectrum which was the first observation of the size-dependent optical properties of nanomaterials.[69] Later, Rosetti et al.[70] and Efros et al.[71] studied the relation between the changes of colors and the control of sizes of nanoparticles, followed by an in-depth discussion of quantum confinement effect by several researchers.[72-75] In bulk materials, the large number of atoms in solids result in the overlap and interaction of the atomic orbitals, which leads to the formation of energy bands. The energy bands in bulk materials are typically broad and continuous, allowing electrons to occupy a wide range of energy states within these energy bands. The composition dependent band gap energy (E_g), the minimum energy required for an electron be excited from the valence band (VB) to the conduction band (CB), is generally used as a characterization of bulk semiconductors.

Compared with bulk materials, NCs usually present exclusive size-dependent optical and electronic properties, which are caused by the quantum confinement effect. The quantum confinement effect becomes significant when the size of a NC decreases to the nanometer scale, comparable to or smaller than the exciton Bohr radius. This effect arises from the restriction of electrons and holes within NCs, leading to discrete energy levels and an increase in the bandgap energy. As a result, the optical and electronic properties, such as absorption, emission, and conductivity, can be tuned by varying the size of NCs.

The quantum confinement effect is not observable in bulk materials due to the wave functions of electrons distributed over a larger spatial range (*i.e.,* >> Bohr diameter). However, by reducing the size of materials to the nanoscale, such as in the QDs, NRs, and NWs, this effect becomes prominent, resulting in distinct and size-dependent optical and electronic properties (Figure 1.2). If the charge carriers, including negatively charged excited electrons and the positively charged holes, are confined within a finite size close to or below the Bohr exciton diameter, as in the case of the nanoscale nanomaterials, the confinement of electron motion leads to a limited number of discrete quantified energy states for the nanomaterials. Brus, et al. described the changes in the band gap as a function of particles' size, according to equation 1.1.[76]

$$E = \frac{\hbar^2\pi^2}{2R^2}\left[\frac{1}{m_e} + \frac{1}{m_h}\right] - \frac{1.8e^2}{\varepsilon_2 R} + \frac{e^2}{R}\sum_{n=1}^{\infty} \alpha_n \left(\frac{S}{R}\right)^{2n} \qquad \text{(eq. 1.1)}$$

Where E is the band gap, ħ is Planck's constant, R is the particle radius, m_e is the effective mass of the electron, m_h is the effective mass of the hole, ε_2 is the dielectric constant of the material, S is the distance between the solvent and exciton, and α is the polarizability. From equation 1.1, when the particle size decreases within the nanoscale, the band gap increases, and discrete energy levels are formed for the NCs with sizes close to and below the Bohr diameter. In 0D, 1D and 2D NCs, charge carriers including electrons and holes are free to move in zero, one and two unconfined directions, respectively. For example, in 1D material quantum wires, the movements of electrons are confined in two directions but can move freely along the unconfined long axes.[77]

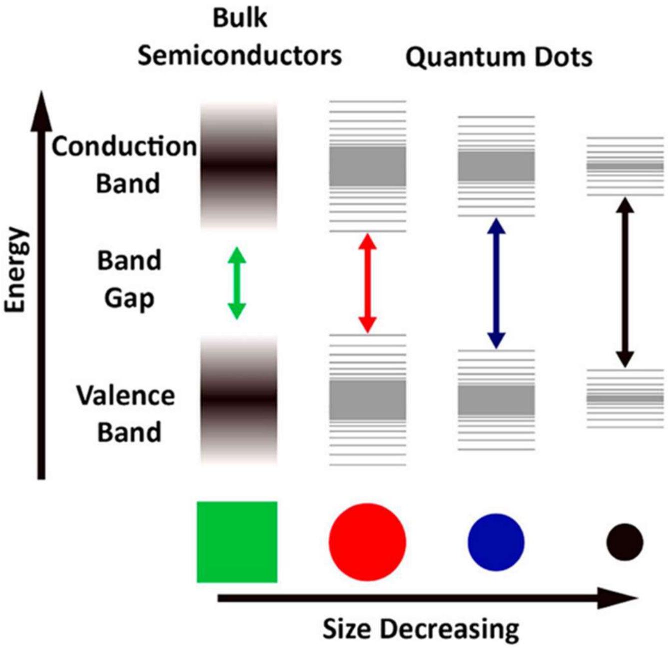

Figure 1.2 The illustration of quantum confinement effect.[2]

[2] [Reprinted (adapted) with permission from { Chen, G.; Roy, I.; Yang, C.; Prasad, P. N., Nanochemistry and Nanomedicine for Nanoparticle-based Diagnostics and Therapy. Chem. Rev. 2016, 116 (5), 2826-85.}. Copyright {2016} American Chemical Society.]

1.1.2 Optical properties of semiconductor Nanocrystals

Semiconductor NCs, such as 0D QDs possess intriguing optical properties that arise from tunable bandgap and quantum confinement effect which allows for the exhibition of a wide range of absorption and emission spectra. For example, as the size of the QD reduces, the effective bandgap increases due to the quantum confinement effect, leading to a blue shift toward to the smaller wavelength (higher energy) for the absorption and emission spectra.[78] (Figure 1.3) When the size of a QD is decreased, the bandgap energy increases, which means that smaller QDs absorb and emit higher-energy photons, resulting in the generation of a shorter wavelength of light, for example, blue or ultraviolet (UV) light. Conversely, when the bandgap energy decreases, this leads to emissions at longer wavelengths, such as red or infrared (IR) light.

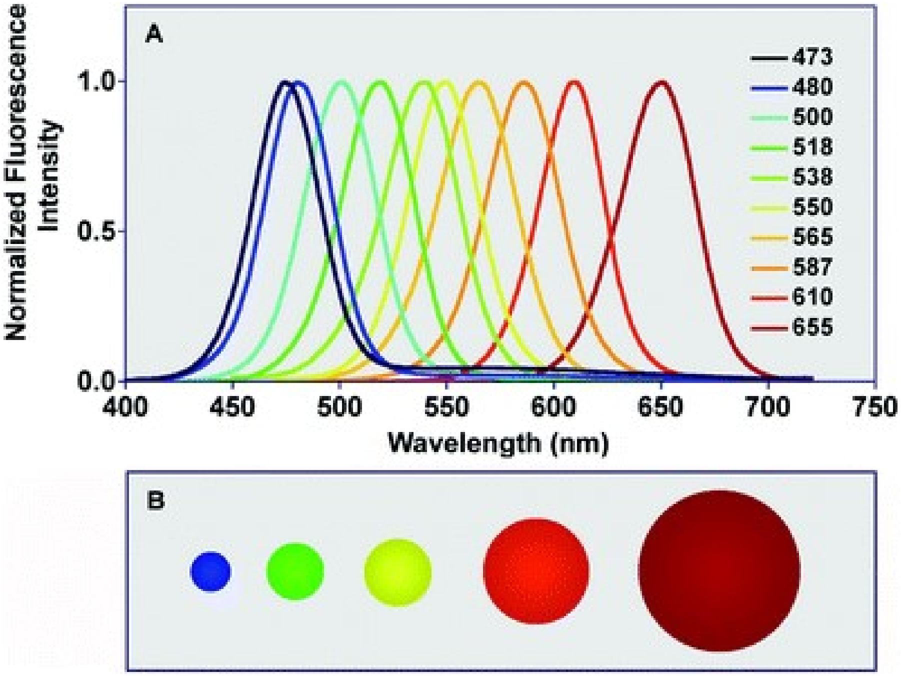

Figure 1.3 Size-tunable emission spectra of cadmium selenide quantum dots within a size range of 2.1 nm to 7.5 nm.[3]

[3][Repurposed with permission from Royal Society of Chemistry © 2004]

When a photon is absorbed, an exciton, which is an electron and hole pair, is created followed by radiative and/or non-radiative relaxation.[79] Figure 1.4 depicts the most common processes of an excited photo within the band gap of a QD. An electron is excited from the VB to CB and an electron and hole pair is generated. The exciton (electron-hole pair) undergoes radiative decay, non-radiative decay, and emits a photon during the process, then returns to the ground state and regenerates an exciton. The processes involving excitons can be detected first by optical instruments, interpretable through spectra, which can then be further analyzed to study the optical properties.

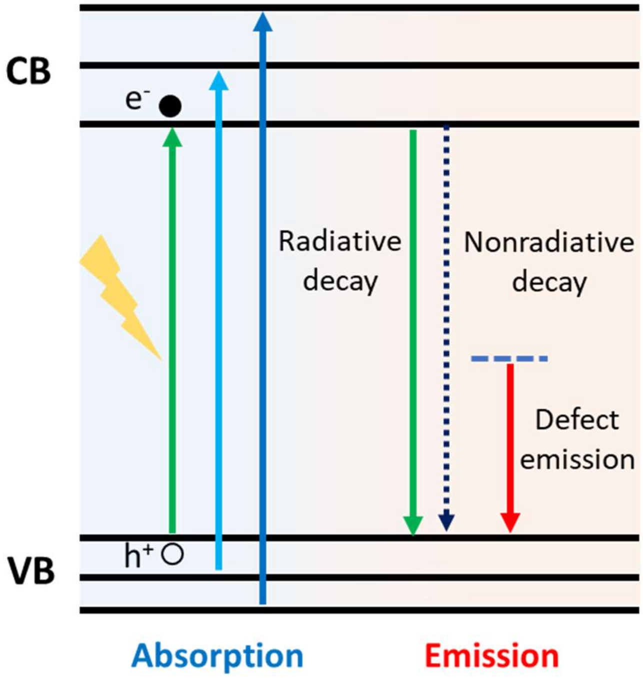

Figure 1.4 Scheme of most common processes involving the excited states of a quantum dot.

Emission bandwidth and quantum yield (QYs) are critical for evaluating the optical properties of QDs and their applicability. Despite the broad absorption spectra due to multiple excitations from incident photo energy higher than the bandgap, QDs exhibit narrow photoluminescence (PL) spectra because of the fast internal conversion and vibrational relaxation (~ps) leading to band edge PL from the bottom of the CB to the top of VB. Photoluminescence quantum yield(s) (PL QYs) is the efficiency of light emission after photo excitation in which photons are absorbed and converted into photo energy.

PL QY could be illustrated simply by an approximate ratio of light absorbed and light emitted.

$$QY_{QD} = \frac{the\ number\ of\ photons\ emitted}{he\ number\ of\ photons\ absorbed} \qquad \text{(eq. 1.2)}$$

Experimental determination of PL QYs could be measured and compared by using a fluorescent dye with a known high QY (*i.e.*, 95% QYs for rhodamine 6G) as a reference.

$$QY_{QD} = QY_R \frac{Absorbance_R}{Absorbance_{QD}} \frac{I_{QD}}{I_R} \frac{{n_{QD}}^2}{n_R} \qquad \text{(eq. 1.3)}$$

Where QY_R is the quantum yield of the reference dye, n is the refractive index of the solvent used to dissolve QDs (n_{QD}) or reference dyes (n_R), *I* is the integrated fluorescent intensity for reference and QDs measured at the same condition. [80, 81]

The value of the PL QY is typically between 0 to 100%. The PL QYs of QDs with high size uniformity and crystallinity could be extremely high, *i.e.*, above 80%, due to the strong overlap of wavefunctions between the electron and hole in the quantum confined structure.[82-84] However, semiconductor NCs have a high surface area-to-volume ratio compared with bulk material due to their nanoscale dimensions, which can lead to surface defects from many unsaturated and nonstoichiometric bonds of the surface atoms. The surface defects can act as trap states for charge carriers, which increases the possibilities of nonradiative relaxation events and therefore lead to limited PL QYs.[78]

1.2 Core/Shell Quantum Dots

Vast attempts have been made to expand the study for various types of nanoparticles with different chemical compositions and band structures, such as group II-VI, III-V, and IV-VI semiconductors, metals, alloys, metal oxides, and perovskites, with corresponding core/shell structures and doped NCs. For example, the II-VI semiconductor NCs include cadmium-based (*i.e.*, CdSe, CdS, CdTe) and lead-based NCs (*i.e.*, PbSe, PbS, PbTe). III-V semiconductor NCs contain indium-based NCs (*i.e.*, InAs, InP, InSb). Among all examples, II-VI cadmium chalcogenide NCs are the earliest developed semiconductors, which were reported tons of literatures about their applications and properties.[11, 66, 85-90]

Generally, a semiconductor NC is composed of an inorganic material surrounded by an organic outer layer of ligands. However, some drawbacks, such as instability, low quantum efficiency, and a high level of surface defects, have become an obstacle. To overcome these weaknesses, core/shell NCs, where another material is passivated onto the surface of the QDs, have been developed.

Core/shell NCs are composed of a core material surrounded by a shell of different material with an onion-like structure.[4] The core material is typically a semiconductor or a metallic material, while the shell is often a different semiconductor with various compositions. The shell could provide an extra protection layer to the core NCs from environmental effects, leading to an enhancement of stability of the NCs. The most common core/shell structures for 0D QDs are the concentric spherical core/shell nanoparticles in which a spherical core is completely surrounded by a shell.[91-93] The core/shell/shell NCs or core/multi-shell NCs with more than one shell composition has been also developed to achieve improved optical properties and higher QYs.[41, 94] (Scheme 1.1)

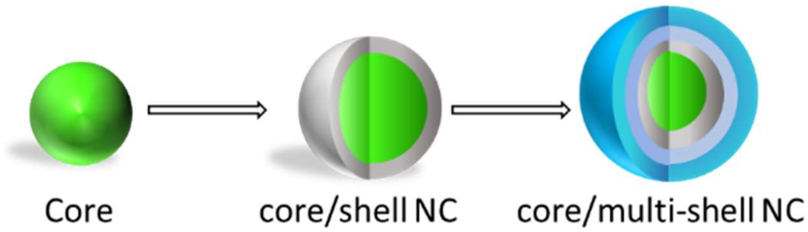

Scheme 1.1 The schematic of spherical core, core/shell, and core/shell/shell (core/multi-shell) NCs.

Depending on the band alignment of the core and shell lattice, different types of core/shell NCs can be obtained with modulated optical and electrical properties. There are three types of semiconductor core/shell NCs based on the band alignment and charge carrier dynamics between core material and shell material. (Figure 1.5) In type I core/shell NCs, the bandgap of the core is smaller than that of the shell, resulting in efficient radiative recombination within the core since both electrons and holes are localized in the core region. The wider band gap shell used in type I core/shell NCs is usually for the goal of separating the optically sensitive core from the environment and improving the overall optical properties. Type I core/shell NCs include CdSe/CdS,[5, 63, 95, 96] CdS/ZnS[97] and CdTe/CdS.[98] In contrast, in reverse type I core/shell NCs, the bandgap of shell lattice is smaller than and confined within the bandgap of core NCs. Therefore, the electrons and holes are partially or completely confined in the shell depending on the band alignments. The commonly studied examples of reverse type I core/shell NCs are CdS/CdSe[50, 51] and ZnS/CdSe.[99] In the type II core/shell NCs, the band alignment shows a staggered arrangement, either the conduction band (CB) edge and valence band (VB) edge are both lower or higher than that of the core. Based on the band alignment, one of the charge carriers is delocalized in the shell region (another one confined in the core), leading to spatial separation of electrons and holes. Examples for type II core/shell NCs are PbSe/CdSe,[100] CdS/ZnSe,[101] and

ZnTe/CdS.[102] And quasi-type II structures usually refer to those NCs with similar staggered band alignment of type II structure but with a very close band edge position for either conduction band or valence band.

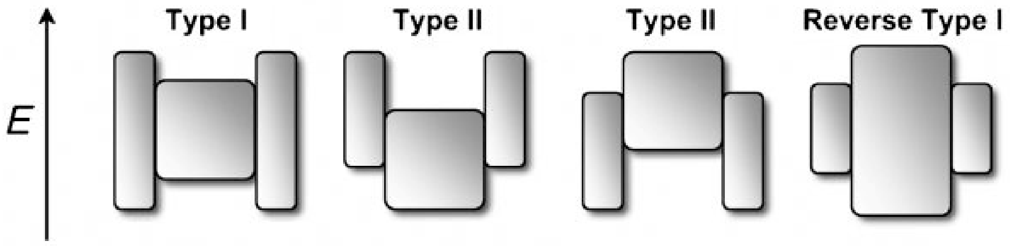

Figure 1.5 Band alignment for core/shell NCs.[4]

[4] [Reprinted (adapted) with permission from {Reiss, P.; Protiere, M.; Li, L., Core/Shell semiconductor nanocrystals. Small 2009, 5 (2), 154-68}. Copyright (2009) John Wiley and Sons Publishing]

1.2.1 Synthesis of core/shell quantum dots

Epitaxial shell growth is a process of depositing a crystalline shell layer onto the surface of a pre-existing NC core while maintaining a well-defined lattice structure and orientation between core and shell layer. In order to obtain core/shell NCs with epitaxial shells, the structure and lattice parameters of both the core and shell lattice, as well as reliable and robust synthetic routes should be considered. Epitaxial growth ensures that the shell material aligns with the crystallographic structure of the core, resulting in a coherent interface between the two materials. During shell growth process, the lattice matching and crystallographic alignment between the core and shell materials are critical factors. If the lattice constants and crystal structures of the core and shell materials are well-matched with a small lattice mismatch (generally < 10%), epitaxial growth can occur, leading to a clear interface with minimized lattice strain between the core and shell. This interface can influence the electronic, optical, and catalytic properties of the resulting core/shell NCs since it significantly impacts the materials' properties by altering their electronic structure, improving charge carrier dynamics, enhancing surface chemistry, and providing thermal and chemical stability. Shell passivation onto the core could significantly improve the stability by acting as a barrier from the influence of the NC environment. For example, CdSe/ZnS core/shell QDs with type I core/shell structure electronically insulate the CdSe cores to make the structure more stable, while the S^{2-} anion, could afford a higher threshold to photooxidative degradation due to the much lower oxidation potential of S^{2-} compared to Se^{2-}.[103 104 105]

Synthetic strategies can vary depending on the desired material, size, morphology and composition of NCs. Colloidal synthesis is a widely used wet chemistry method for preparing NCs with controllable crystallinity and morphology. These methods usually involve the formation, nucleation, and growth of NCs in a solution or suspension, where the solvents, surfactants, and precursor compounds undergo a coordination reaction to form the desired shape of the NCs. Compared with a solid state reaction, colloidal synthesis can provide a more uniform and more tunable size and shape of the NCs. The selection of precursors, ligands, temperature, and reaction time are key factors to control the nucleation and growth of NCs.

There are several colloidal synthetic approaches to fabricating core/shell NCs, including successive ion layer adsorption and reaction (SILAR) and single source precursor (SSP) methods. The SILAR method is a well-developed approach used in the synthesis of core/shell materials. As the name illustrates, SILAR is a technique in which different precursors absorb onto the core layer by layer. Originally, the SILAR method was developed for depositing thin film onto the solid substrate until Peng's group introduced it into the growth of high-quality core/shell NCs. Peng's group reported a large scale of CdSe/CdS core/shell NCs were synthesized by using air-stable precursors via SILAR approach. The alternative injection of cationic and anionic precursors into the reaction solution avoid homogeneous nucleation of shell

NCs and control the shell growth monolayer by monolayer, leading to high quality core/shell NCs with a nearly monodisperse shell growth onto the core and high PL QYs.[4, 106] (Figure 1.6)

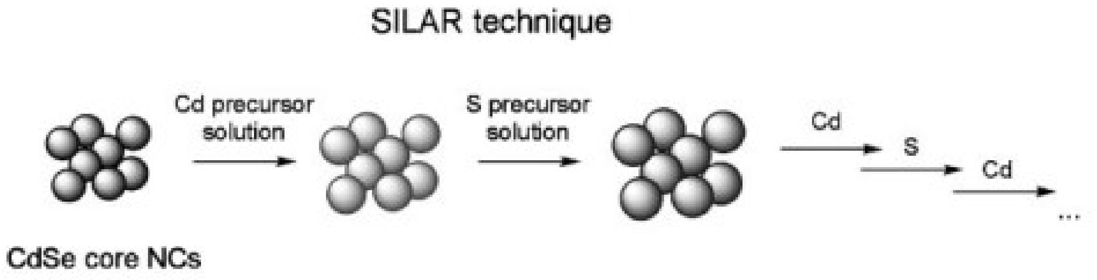

Figure 1.6 Schematic of shell growth onto a core via SILAR method.[4]

[4][Reprinted (adapted) with permission from {Reiss, P.; Protiere, M.; Li, L., Core/Shell semiconductor nanocrystals. Small 2009, 5 (2), 154-68}. Copyright (2009) John Wiley and Sons Publishing]

Single source precursor (SSP) strategy is a simple but attractive way to make a core/shell material. A SSP contains all the elements that are required to coat a shell, such as metal thiocarbamate, or a metal organic cluster. Because of the highly reactive SSP for the shell lattice, the temperature for the core/shell synthesis using the SSP method is usually lower than that of the SILAR method. In the process of CdSe/CdS core/shell NCs synthesis, cadmium diethyldithiocarbamate ($Cd(DDTC)_2$) was used as a SSP to grow CdS shell onto a pre-synthesized CdSe core under a moderate temperature (*i.e.*, 200 °C).[107] Peng's group reported that $Cd(DDTC)_2$ as well as zinc diethyldithiocarbamate ($Zn(DDTC)_2$) were used for shell growth of high quality CdSe/CdS and CdS/ZnS core/shell NCs under different range of temperature.[5](Figure 1.7)

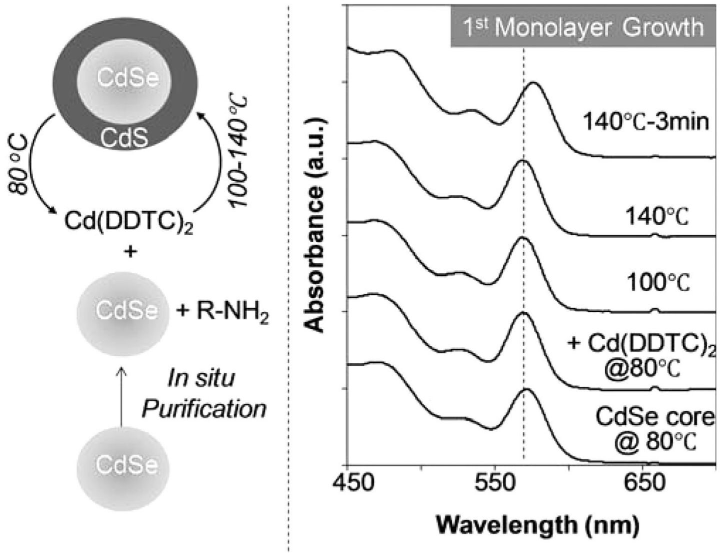

Figure 1.7 Left panel: schematic of a core/shell synthesis process by using single source precursor. Right panel: absorption spectra of CdSe core and the first monolayer of CdS growth onto the core.[5]

[5] [Reprinted (adapted) with permission from {Nan, W.; Niu, Y.; Qin, H.; Cui, F.; Yang, Y.; Lai, R.; Lin, W.; Peng, X., Crystal structure control of zinc-blende CdSe/CdS core/shell nanocrystals: synthesis and structure-dependent optical properties. J. Am. Chem. Soc. 2012, 134 (48), 19685-93.}. Copyright {2012} American Chemical Society.]

1.2.2 Interface engineering of core/shell quantum dots

The core/shell interface plays a critical role in determining the physical and chemical properties. The lattice mismatch between core and shell usually generates a large strain or distortion within NC lattice. In epitaxial growth, the strain caused by lattice mismatch alters the band edges significantly. The Nie group examined the changes of band alignment caused by lattice strain in CdTe/ZnSe core/shell NCs.[108] The electrons and holes should be confined within the core and formed a type I core/shell structure based on the band alignment of their bulk counterparts. However, they found that a quasi-type II core/shell structure was formed because of the shift of the band gap in which a large lattice strain was induced during the shell passivation.

Interestingly, it has been found that an alloy interface can be formed between the core and shell in order to reduce the lattice stain. (Figure 1.8) The lattice stress at the interface of the core and shell arises from the lattice mismatch of two materials during epitaxial growth. The ~12% lattice mismatch between the wurtzite structure of CdSe and ZnS NCs generates a large lattice strain at the interface which causes lattice distortion and relaxation during shell growth. The alloyed $Cd_{1-x}Zn_xSe_{1-y}S_y$ interface is formed by vacancy formation, lattice relaxation, and ion migration to reduce this large lattice strain, which can influence the optical and magnetic properties.[6]

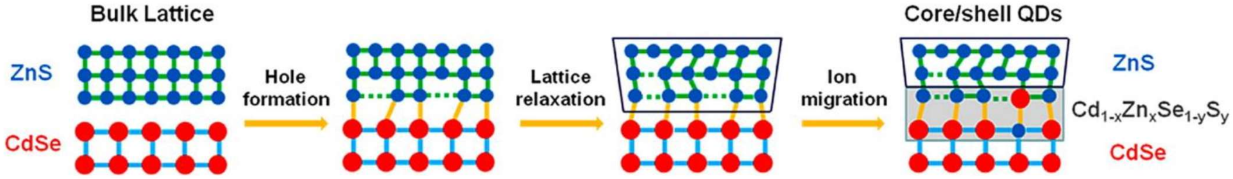

Figure 1.8 Schematic of alloy formation to reduce the lattice strain within CdSe/ZnS core/shell NCs.[6]

[6][Reprinted (adapted) with permission from {Zheng, W.; Wang, Z.; van Tol, J.; Dalal, N. S.; Strouse, G. F., Alloy formation at the tetrapod core/arm interface. Nano Lett. 2012, 12 (6), 3132-7.}. Copyright {2012} American Chemical Society.]

Core/shell/shell NCs, also known as core/multi-shell NCs, are utilized in cases of larger lattice mismatches between the core and shell crystals. Therefore, an additional shell layer with lattice parameters intermediate between that of the core and shell are used to reduce lattice strain, enhance core/shell stability, and improve optical properties. For example, CdSe/CdS/ZnS and CdSe/ZnSe/ZnS core/shell/shell QDs were achieved with a largely improvement of crystallinity and stability.[109]

1.3 Doping in Semiconductor Nanocrystals

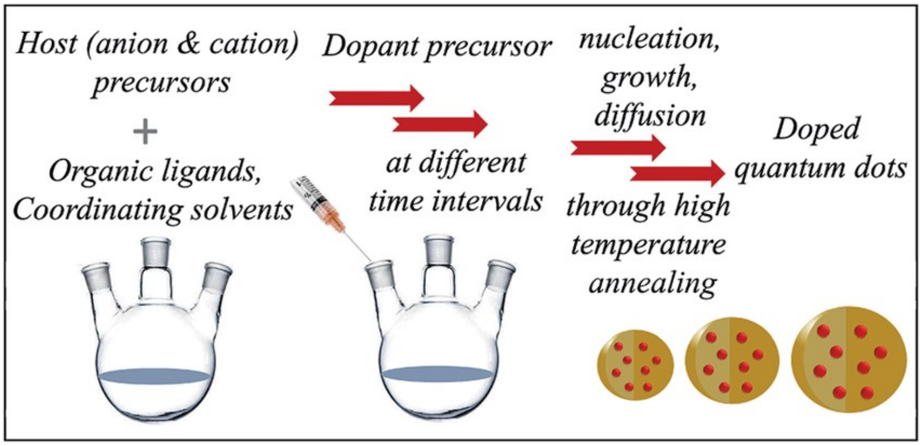

Figure 1.9 Schematic of colloidal synthesis of doped NCs.[7]

Introducing transition metal ions, known as dopants, into the crystal lattice is a critical approach to add new properties and/or enhance the optical properties of NCs. Doping with transition metal ions with unpaired electrons in NCs is a process that modifies the intra energy band alignment within the NCs so as to expand their wide range of interesting spintronic and magnetic properties.[110-115] Doped NCs with various doping levels can be obtained through a colloidal synthetic approach. (Figure 1.9) This process involves heating a solution of organic ligands, dopant precursor, and host cation/anion precursors in a flask and controlling the reaction time and temperature to achieve a controllable size and morphology of the resulting doped NCs.[7] Impurity atoms can be incorporated into the crystal lattice with a high concentration, up to their solubility limit, such as **10%** or more doping concentrations in Mn doped II-VI semiconductors.[116] However, a few percents doping concentration can affect the properties of the NCs significantly. For example, Banin et al. reported enhancing optical properties by Ag and Cu doping in InAs NCs, which can be applied to transistors and solar cells.[117] Another advantage is that doped NCs could have improved photo and thermal stability.[9]

1.3.1 Doping for modified and enhanced optical and electronic properties

Incorporating a transition-metal ion into a semiconductor host typically could result in the creation of a dopant-related energy level within the mid-gap region of the host. These mid-gap states play a pivotal role in causing significant alterations to the material properties, with the characteristics of these mid-gap states predominantly influencing the properties exhibited by a doped semiconductor nanocrystal.[118, 119] For instance, the luminescence observed in Cu-doped ZnSe NCs is attributed to a localized deep trap state bound to the dopant ion, while the plasmonic properties in Cu^{2+} doped Cu_2S ($Cu_{2-x}S$) NCs are governed by holes occupying delocalized states.[120, 121] In many doped NCs, dopants will exhibit a Poisson distribution within the NC ensemble. To control the radial position of Mn dopants in the CdS/ZnS core/shell QDs, Cao's group developed a stepwise doping strategy including nucleation/growth of core QDs, dopant growth, and shell coating.[122] By introducing Mn dopant ions into the core, at the core/shell interface, or in ZnS shell of the core/shell QDs, different optical properties and PL QYs were obtained.[12] Son *et al.* reported that the energy transfer dynamics and charge carrier localization in doped NCs was highly dependent on the doping location and concentration,[123] which indicates the host-to-dopant energy transfer efficiency can be finely tuned by the depth of Mn dopants in the ZnS shell of the CdS/ZnS core/shell QDs.

Pristine semiconductor NCs exhibit size-dependent absorption and emission behavior, usually with small Stoke shifts, which leads to significant spectra overlap between absorption and emission spectra. The spectra overlap causes self-absorption of emission by other NCs in the ensemble, which leads to low PL QYs of the NCs.[109, 124] Doped NC could minimize the self-absorption effect due to the host to dopant energy or electron transfer, where the dopant emission usually occurs on a longer wavelength size with reduced or zero overlap with the host absorption spectra.[125, 126] Mn^{2+} ions have been widely studied as dopants for semiconductor NCs since the first successful incorporation of Mn^{2+} ions into a nanocrystalline ZnS lattice was reported by Bhargava et al. in 1994.[125] A scheme of the interstate band alignment after Mn^{2+} doping into a CdS lattice is shown in scheme 1.2. A modified light emission occurred because of the energy transfer from the host lattice to the electronic states of the Mn^{2+} ions, leading to a broad yellow-orange dopant emission in the ~500 - 700 nm region. [110, 127] As a paramagnetic impurity, the Mn emission is caused by energy transfer from spin forbidden $^4T_1$ to $^6A_1$ state, with significantly longer lifetime (~ms) compared with that of host semiconductor NCs (~ns).[115, 128-132]

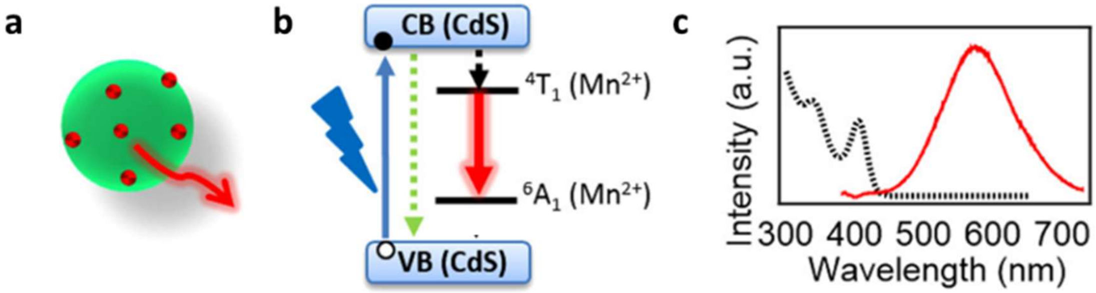

Scheme 1.2 (a-b) Schematic of the interstate band alignment (c) The corresponding optical absorption and emission spectra of the Mn^{2+} doped CdS NCs.[14, 17]

[14][Reprinted (adapted) with permission from {Hofman, E.; Khammang, A.; Wright, J. T.; Li, Z. J.; McLaughlin, P. F.; Davis, A. H.; Franck, J. M.; Chakraborty, A.; Meulenberg, R. W.; Zheng, W., Decoupling and Coupling of the Host-Dopant Interaction by Manipulating Dopant Movement in Core/Shell Quantum Dots. J. Phys. Chem. Lett. 2020, 11 (15), 5992-5999.}. Copyright {2020} American Chemical Society.]

[17][Reprinted (adapted) with permission from {Hofman, E.; Robinson, R. J.; Li, Z. J.; Dzikovski, B.; Zheng, W., Controlled Dopant Migration in CdS/ZnS Core/Shell Quantum Dots. J. Am. Chem. Soc. 2017, 139 (26), 8878-8885.}. Copyright {2017} American Chemical Society.]

As the ligand shell induces significant strain in doped QDs. Pradhan et al. found that the Mn emission could be tuned from 565 nm to 610 nm by altering the outer ligand shell and the dopant's position within the QDs.[133] If Mn atoms are located closer to the surface, a red shift in Mn emission could be observed. Nag et al. tuned the Mn emission from 580 nm to 620 nm by adjusting the distance of the Mn center from the surface.[134] The emission maximum from a Mn dopant center situated in different location within a QD is expected to shift due to the variation in local strain, resulting in a broader linewidth for the ensemble QDs. In addition, the tunable lattice strain offers the possibility of adjusting the Mn emission, especially in the QDs due to their large surface-to-volume ratio. For example, the Nie group found that lattice strain can significantly change bandgap energies when a ZnSe shell is epitaxially grown onto a CdTe core, which leads to largely changes in band alignment and optical properties.[108] In their bulk form, CdTe/ZnSe heterostructures typically exhibit a type-I structure based on the band alignment. However, at the nanoscale, the growth of a ZnSe shell applies a strong compressive force onto the CdTe core due to the large lattice mismatch (5.668 Å in ZnSe, and 6.482 Å in CdTe). This results in the compression of the CdTe lattice and an expansion of the ZnSe lattice to reduce the lattice strain, leading to a quasi-type II core/shell band alignment. Ithurria et al. studied the effects of shell applied pressure within Mn doped CdS/ZnS heterostructures varied by different shell thicknesses and doping depths. Different shell pressure around a Mn dopant center could affect the crystal field splitting energy of dopant ion energy level,[135, 136] and consequently, the position of the Mn PL can be tuned by varying the shell thickness. In their work, the Mn dopant ions were incorporated with various radial positions between 1.65 and 3.3 nm by controlling ZnS shell thickness between CdS core and Mn dopants from 0 to 6 monolayer(s).

The incorporation of transition metal dopant ions into semiconductors introduces novel magnetic characteristics to the crystal structure, leading to the formation of dilute magnetic semiconductor (DMS) NCs. These are known for their substantial magneto-optical effects, which arise from the strong sp-d exchange interactions between the host carriers and transition dopant ions.[137] Consequently, the utilization of paramagnetic transition metal dopants in semiconductor nanomaterials has significant interest because of their potential applications in the field of spintronics and quantum information processing. Efros et al., theoretically studied the voltage-controlled spin valves for applications in single spin nanomaterials.[138] Gamelin's group reported the observation of carrier mediated ferromagnetic interactions in Mn doped ZnO NCs.[139, 140] They demonstrated that manganese-doped zinc oxide NCs exhibit a substantial, reversible increase in magnetization at room temperature when electrons are added. This increasing magnetization originates from new ferromagnetic coupling between Mn ions overcoming the inherent antiferromagnetic interactions from the nearest neighbor Mn dopants. Despite small electron-manganese exchange energies, this pronounced magnetization effect arises through competing electron-mediated ferromagnetic couplings between Mn^{2+} ions within individual NCs.[139]

1.3.2 Synthetic methodology of doped Nanocrystals

The modification and/or improvement of properties in NCs from the introduction of dopants is only possible when the effective dopant incorporation occurs. Effective doping refers to the dopants substituting host atoms within a crystal lattice rather than simply being absorbed onto the surface. When dopants are merely absorbed on the surface, self-purification and/or dopant ejection can occur due to the higher formation energy of impurity incorporation compared to bulk materials, which result in undopable NCs.[141]

The synthetic methodology for doped NCs can vary depending on the specific dopant, host material, desired properties, and the targeted application. Dopants can be simply induced into a lattice by co-precipitation methods, in which dopant precursors are added to the reaction mixture along with the precursors for the host material. The reaction conditions are adjusted to promote the incorporation of dopant ions into the growing NCs. Dopant ions can be incorporated into semiconductor NCs through several advanced colloidal synthetic approaches, such as using single source precursors,[142-144] doping during nanocrystal nucleation[10, 133] and/or growth[122], and diffusing dopant ions into the nanocrystal lattice post-synthesis.[16, 145] (Scheme 1.3)

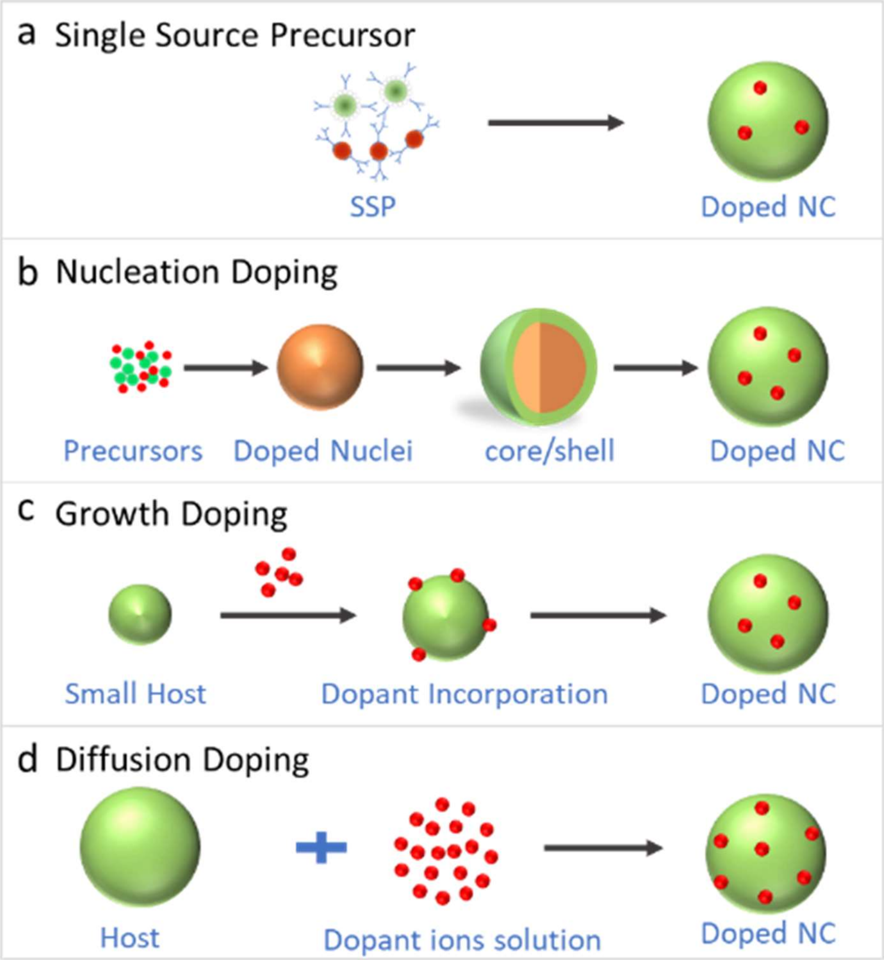

Scheme 1.3 Schematic of general strategies of doped NC. Schematic representation of (a) single source precursors, (b) nucleation-doping, (c), growth-doping, and d) diffusion doping. Red and orange dots represent dopant ions and precursors. Green dots represent host precursors and ions.

Among the various strategies for NC doping, the single-source precursor (SSP) approach enables a controlled and systematic transformation through thermal decomposition of metalloorganic molecules containing both cations and anions within a complex. Through a straightforward heating process, the SSP undergoes thermal instability, leading to its decomposition and the subsequent formation of NCs. The strategic design of the SSP method allows for precise control over the resulting NCs' stoichiometry, phase, and morphology. A critical consideration with SSP reaction involves comparing the binding energy between the inorganic NC elements and the binding energies between the metalloorganic complex and coordinating ligands. If the binding energy of the NC is similar and/or falls below that of metalloorganic complex to coordinating ligands, there is a risk of nonselective decomposition, potentially hindering the formation of NCs.[107, 143, 146] Zheng et al. reported that Cr-doped ZnSe QDs could be achieved by using a $Li_4[Zn_{10}Se_4(SePh)_{16}]$ SSP. The SSP reacted with added dopant precursor and ligands at a high temperature to produce dispersive spherical doped QDs with doping level of 0.4% - 4.0%.[142] Besides doping transition metal ions into chalcogenide semiconductor NCs, the SSP approach could also be used in the incorporation of dopant lanthanide ions in II-VI NCs. A successful doping of Ce^{3+} and Eu^{2+} in monodisperse ~10 nm colloidal SrS NCs by using strontium diisopropyldithiocarbamate ($Sr(DPTC)_2$), cerium diethyldithiocarbamate ($Ce(DDTC)_4$) (for Ce^{3+}:SrS NCs), and europium diethyldithiocarbamate ($Eu(DDTC)_4$) (for Eu^{2+}:SrS NCs) combining ion diffusion doping and growth doping was reported.[8] (Figure 1.10) Using the same strategy, replacing the $Sr(DPTC)_2$ SSP with calcium diisopropyldithiocarbamate ($Ca(DPTC)_2$), together with dopant SSP, $Ce(DDTC)_4$ and $Eu(DDTC)_4$, Ce^{3+}:CaS and Eu^{2+}:CaS NCs were obtained.

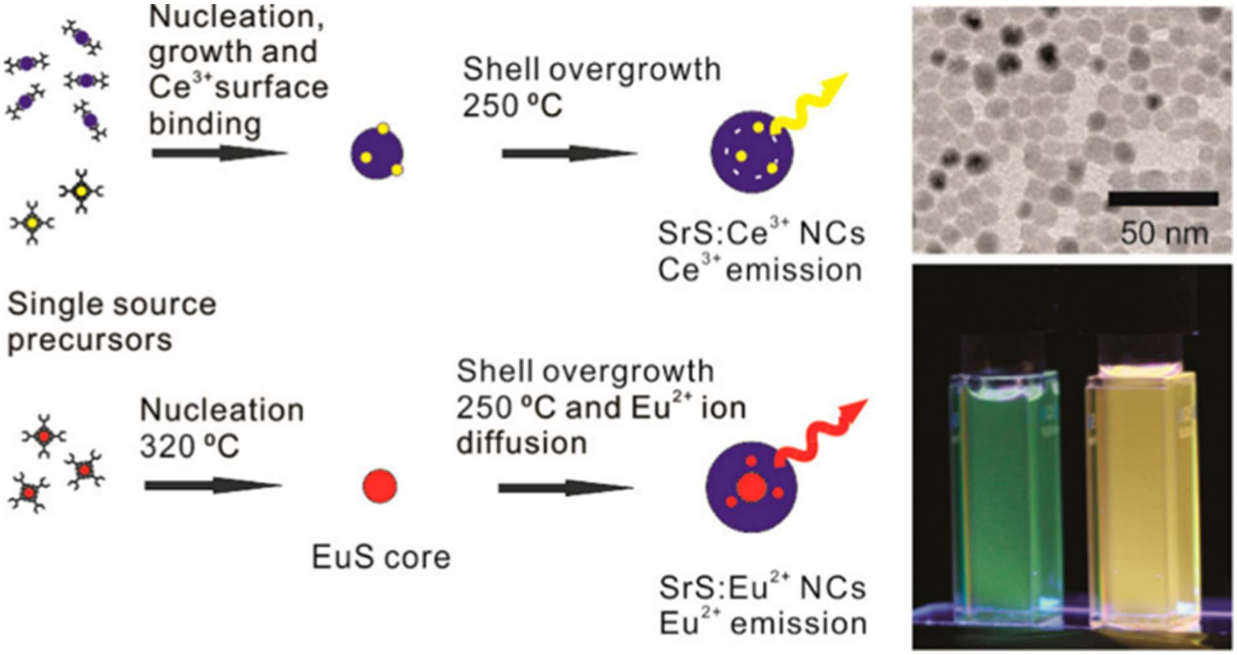

Figure 1.10 Schematic illustration of the synthesis of Ce^{3+}:SrS NCs and Eu^{2+}:SrS NCs. Top: the synthesis of Ce^{3+}:SrS NCs using SSP approach. Bottom: the synthesis of Eu^{2+}:SrS NCs using SSP with ion diffusion doping strategy.[8]

[8][Reprinted (adapted) with permission from {Zhao, Y.; Rabouw, F. T.; Puffelen, T. v.; Walree, C. A. v.; Gamelin, D. R.; de Mello Donegá, C.; Meijerink, A., Lanthanide-Doped CaS and SrS Luminescent Nanocrystals: A Single-Source Precursor Approach for Doping. J. Am. Chem. Soc. 2014, 136 (47), 16533-16543.}. Copyright {2014} American Chemical Society.]

Peng's group developed nucleation-doping and growth-doping approaches for controlling dopant location within NCs.[11] (Figure 1.11) For the nucleation-doping approach, a dopant precursor (*i.e.,* manganese stearate) and selenium in tributyl phosphine were mixed in an amine-rich solution and reacted under a high temperature to form MnSe nuclei. The reaction was slow and gradually occurred within a few hours to changing the solution color yellow after the addition of zinc acetate, which indicates a ZnSe shell or interface formed onto the MnSe core.[11] Mn doped ZnSe NCs were obtained through adjusting shell growth temperature and precursor reactivity, due to Mn ions diffusing towards the shell. For the nucleation doping strategy, the reaction conditions, such as temperature and reaction time, and precursor reactivity can be controlled so that dopant ions nucleate first to form a small core, followed by growth of the host lattice as the shell. This method produces an initial small ZnSe host NCs. Subsequently, dopant precursors Cu ions are introduced into the core to form Cu:ZnSe without further growth of the host. The regrowth of the ZnSe core encapsulates the dopant ions within the host lattice, ultimately yielding center doped NCs.[11]

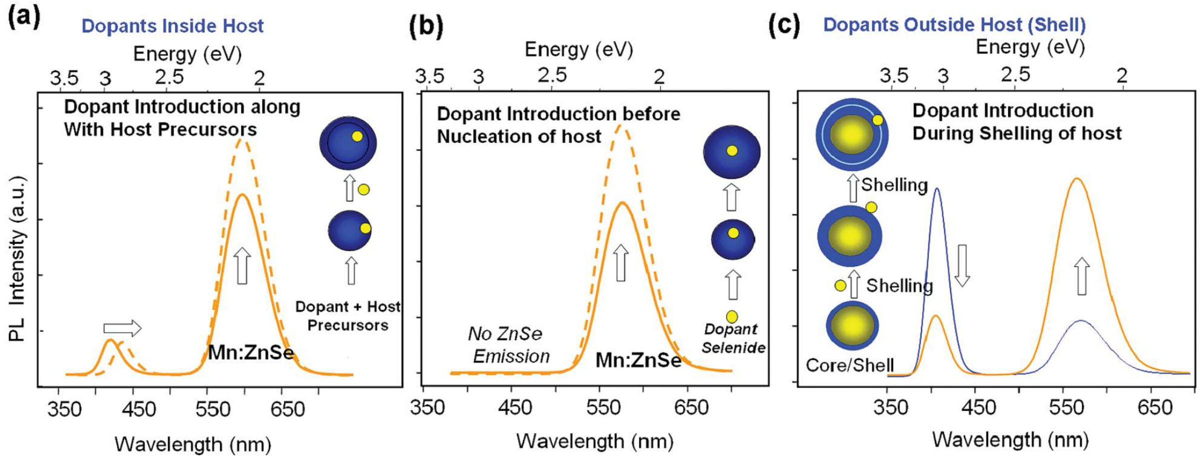

Figure 1.11 Different doping process for Mn doped NCs. (a), the dopants were introduced with host precursors together at the start of the reaction. (b), dopants were introduced before the nucleation of host. (c), dopants were introduced into a shell during the shell growth. [9-12]

[9] [Reprinted (adapted) with permission from {Pradhan, N.; Sarma, D. D., Advances in Light-Emitting Doped Semiconductor Nanocrystals. J. Phys. Chem. Lett. 2011, 2 (21), 2818-2826.}. Copyright {2011} American Chemical Society.]

[10] [Reprinted (adapted) with permission from {Norris, D. J.; Yao, N.; Charnock, F. T.; Kennedy, T. A., High-Quality Manganese-Doped ZnSe Nanocrystals. Nano Lett. 2001, 1 (1), 3-7.}. Copyright {2001} American Chemical Society.]

[11] [Reprinted (adapted) with permission from {Pradhan, N.; Goorskey, D.; Thessing, J.; Peng, X., An alternative of CdSe nanocrystal emitters: pure and tunable impurity emissions in ZnSe nanocrystals. J. Am. Chem. Soc. 2005, 127 (50), 17586-7.}. Copyright {2005} American Chemical Society.]

[12] [Reprinted (adapted) with permission from {Yang, Y.; Chen, O.; Angerhofer, A.; Cao, Y. C., Radial-position-controlled doping in CdS/ZnS core/shell nanocrystals. J. Am. Chem. Soc. 2006, 128 (38), 12428-9.}. Copyright {2006} American Chemical Society.]

The precise control of dopant concentration, dopant distribution, and dopant location are critical for all doping strategies, which could finely manipulate the electronic, optical, and magnetic properties of the materials. The control of the dopant location and distribution is very challenging and yet to be fully studied and developed. It is critical to develop synthetic methodologies to precisely tune the dopant sites/distribution in a NC lattice. However, traditional doping methods, such as cation exchange and dopant diffusion, typically generated a random distribution of dopants within doped nanomaterials, which make it more difficult to precisely predict and/or examine the relationship between dopant location and properties; randomly distributed dopants prevent a high-level of control over the optical, electronic, and magnetic properties of nanomaterials. To control the dopant location inside NCs, Cao's group developed a three-step **growth doping approach** to precisely control dopant radial positions within CdS/ZnS core/shell NCs, which is determined by the diameter of the starting host materials and the controlled shell thickness.[12, 147] For the growth-doping strategy, at first small host CdS NCs were synthesized following by the lowering temperature for the reaction; under the lower temperature, the single molecular precursor (*i.e.,* $Mn(S_2CNEt_2)_2$) was introduced into the solution for growth on the surface without further growth of the host particles. After that, either further shell growth or regrowth of host NCs could be applied. Host particles, *i.e.*, CdS or CdS/ZnS NCs, were synthesized as the first step, and then Mn dopants were introduced on the surface of the host particles to form Mn doped NCs, followed by the shell growth step. By using this three-step strategy, Mn dopants could be placed inside the core, on the core/shell interface, and in the shell. (Figure 1.12) Later, Son's group explored the energy transfer dynamics between a differently located dopant ion and host particles.[123] They found that the energy transfer rate of exciton to Mn dopant was strongly dependent on the dopant location, with results showing the strongest energy transfer rate when the dopant ions were located the closest to the core.

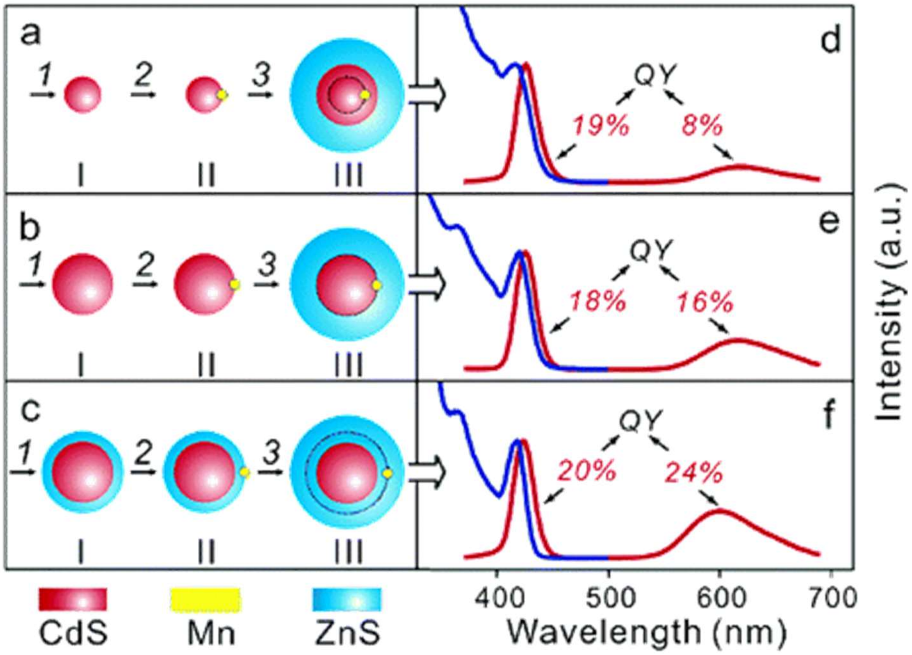

Figure 1.12 A scheme of Mn-doped CdS/ZnS core/shell NCs show a change of PL QYs with different Mn positions: Mn dopants be located (a) inside the CdS core, (b) at the core/shell interface, and (c) in ZnS shell.[12]

[12][Reprinted (adapted) with permission from {Yang, Y.; Chen, O.; Angerhofer, A.; Cao, Y. C., Radial-position-controlled doping in CdS/ZnS core/shell nanocrystals. J. Am. Chem. Soc. 2006, 128 (38), 12428-9.}. Copyright {2006} American Chemical Society.]

Diffusion doping originates from cation exchange reactions, where incoming dopant cations can replace existing cations in the solid if the dopant concentration and ligands permit. Ion diffusion doping can be considered a type of growth doping, where dopant diffusion is required for incorporation of the dopant ions into the host lattice rather than just surface adsorption. In the cation exchange method, pre-synthesized host NCs are immersed in a solution containing dopant ions. The dopant ions replace the host ions in the NC lattice through ion exchange reactions. This method allows precise control over the doping concentration by adjusting the duration and conditions of the ion exchange process. However, cation exchange doping has only been achieved for a small subset of rapidly diffusing cation pairs. For some cations with a slower diffusion rate, such as Mn^{2+}, the reaction requires elevated temperatures that lead to severe Ostwald ripening and loss of nanocrystal morphology.[148] Recent studies on nanomaterials have shown that ions can diffuse much faster and at lower temperatures in NCs compared to their bulk counterparts.[149, 150] This rapid diffusion kinetics results from the high surface-to-volume ratio and decreased activation energy for nucleation in nanomaterials. For efficient diffusion doping, two conditions must be satisfied: the lattice must be sufficiently dynamic to enable true mixing rather than solely heterostructure formation, and interparticle/intraparticle mass transfer must be prevented.[16] The Gamelin group synthesized high-quality colloidal $Cd_{1-x}Mn_xSe$ NCs by using the newly developed diffusion doping method.[16] The $Cd_{1-x}Mn_xSe$ NCs with negligible Ostwald ripening and crystallographic phase were obtained due to Mn^{2+} ions diffusing into the lattice through the controlling of the solution and lattice chemical potentials of cations.

1.3.3 Characterization of doped nanocrystals

Characterizing doped NCs, including dopant concentration and location inside NCs (surface site, core site, and specific depth), is essential for understanding their structural, optical, electronic, and magnetic properties. Several characterization techniques, including optical spectroscopy, electron paramagnetic resonance spectroscopy (EPR), X-ray diffraction (XRD), inductively coupled plasma-atomic emission spectroscopy (ICP-OES) or inductively coupled plasma-mass spectroscopy (ICP-MS), and transmission electron microscopy (TEM), can provide valuable insights into the nature and properties of doped NCs. For example, ICP can provide the type and concentration of dopant ions, while EPR can reveal the oxidation and spin state of paramagnetic dopants. However, there is no single technique that can provide all information on the dopants and doped NCs. Therefore, a combination of analytical tools is usually employed to provide detailed information about the composition and structure of doped NCs as well as their properties.

UV-Vis absorption spectroscopy and photoluminescence (PL) spectroscopy are commonly employed to investigate the optical properties of doped NCs in a wide range of wavelengths. For example, in Mn doped NCs, there is a 600 nm PL usually observed from Mn dopants as the result of the host-to-dopant energy transfer.[110, 126, 151] These techniques provide information about the absorption and emission characteristics, energy levels, and PL QYs of the doped NCs.

X-ray diffraction (XRD) is used to determine the crystal structure, crystallinity, and lattice parameters of doped NCs. By analyzing the diffraction patterns, information about the dopant incorporation, crystal phase, and crystalline quality can be obtained. The lattice contraction and expansion due to the presence of dopant atoms can be identified by XRD patterns. For example, the incorporation of small substitutional Mn dopants (80 pm) into the Cd sites (92 pm) of CdS NCs leads to the shift of XRD peaks to higher angle due to lattice contraction arising from shorter Mn-S bonds compared to Cd-S bonds.[17] In aluminum (Al) doped ZnO NCs, due to the large size differences between Al^{3+} (53 pm) and Zn^{2+} (74 pm), lattice contraction is observed when substitutional doping occurs, while lattice expansion would be expected for the interstitial doping.[152, 153] Besides, XRD diffraction peak position gives the easy way to calculate the sizes of NCs (diameter) by using Debye-Scherrer equation.[154]

$$L = \frac{k\lambda}{B\,\mathrm{co}} \qquad \text{(eq. 1.4)}$$

Where L is the coherence crystalline length of the particle, B represents the full width at half maximum (FWHM), k represents the Scherrer constant (0.98), λ stands for the wavelength of X-ray.

X-ray photoelectron spectroscopy (XPS) is a surface-sensitive technique that provides information about the elemental composition and chemical states of atoms present on the surface of doped NCs. It can be used to investigate the presence and chemical environment of dopant atoms, as well as their oxidation states.[106, 155] X-ray absorption fine structure (XAFS) is also a powerful tool to interrogate the local coordination environment of the dopant ions, providing valuable information regarding the distance between elements of interest and surrounding atoms, as well as granting aspects pertaining to local lattice perturbations caused by lattice mismatch(s). In addition, XAFS studies allow us to probe the electronic and atomic structure of each element within the NCs, and use changes in signal to validate the dopant migration to the surface or interface region.[117, 156-158] For example, using extended X-ray absorption fine structure (EXAFS) spectroscopy to illustrate the nature of the interface in a core/shell NC with dopant serve as an internal probe, *i.e.*, Cu doped CdSe/CdS core/shell QDs, is a direct technique to study the local structure and microenvironment around a dopant.[159]

Transmission electron microscopy (TEM) and scanning electron microscopy (SEM) can provide size, shape, and internal structure of NCs. High-resolution TEM (HRTEM) can further reveal the lattice structure and defects within the NCs, which allow it to be a universal tool to clarify the size distribution and morphology.[117, 160-162] Additionally, electron energy loss spectroscopy (EELS) and energy-dispersive X-ray spectroscopy (EDS) techniques can be employed in conjunction with TEM to analyze the elemental composition, electronic structure and local chemical bonding environment.[163] It can reveal the presence of dopant atoms within the

NC lattice and provide insights into their distribution and ordering. EDS provides rapid survey analysis to determine elemental composition. However, EELS offers more detailed information about chemical bonding and phases.[163, 164]

Electron paramagnetic resonance (EPR) spectroscopy has been used to study the electron spin resonance of paramagnetic dopants in doped NCs. EPR can provide information about the local magnetic environment, spin interactions, and defects in the NC lattice. The EPR spectra of dopant ions in NCs can provide insights into their local environment and coordination. The spectral parameters, such as g-factor and hyperfine splitting, can provide information about the symmetry, bonding, and coordination of the dopant ions within the NC lattice. EPR could also provide additional information about dopant concentration and defects on the surface. For example, in Mn^{2+} ions doped II-IV chalcogenide semiconductors, EPR spectra consists of a sextet hyperfine splitting pattern arising from the S = 5/2, I = 5/2, L = 0 ground state ($^6A_1$) for Mn^{2+} ions represents Mn ions occupying an approximate tetrahedral sites in a II-IV lattice as shown in figure 1.13.[13, 165] The distinguish g- and A-values could be assigned to different Mn^{2+} microenvironment, occupying the surface or core of the QDs.[13, 166] The different g-value and A-values stand for unique crystal fields which could represent Mn ions were incorporated into a different cation site.[6] For examples, the g-values for CdS (g = 2.0029),[167] CdSe (g = 2.003),[168] ZnS (g = 2.002),[169, 170] ZnSe (g = 2.0024),[171] and the A-value for CdS (A = 69.4 G), CdSe (A = 65.9 G), ZnS (A = 68.2 G), ZnSe (A = 64.3 G).[6, 172] Whereas the large hyperfine splitting constant, like 90 G, correspond to isolated Mn with different bonding environments present near the surface.[170, 173] The broad signal in EPR originates from the dipole-dipole interactions between Mn^{2+} ions and the increasing Mn concentration make its relative contribution increase.[165, 174]

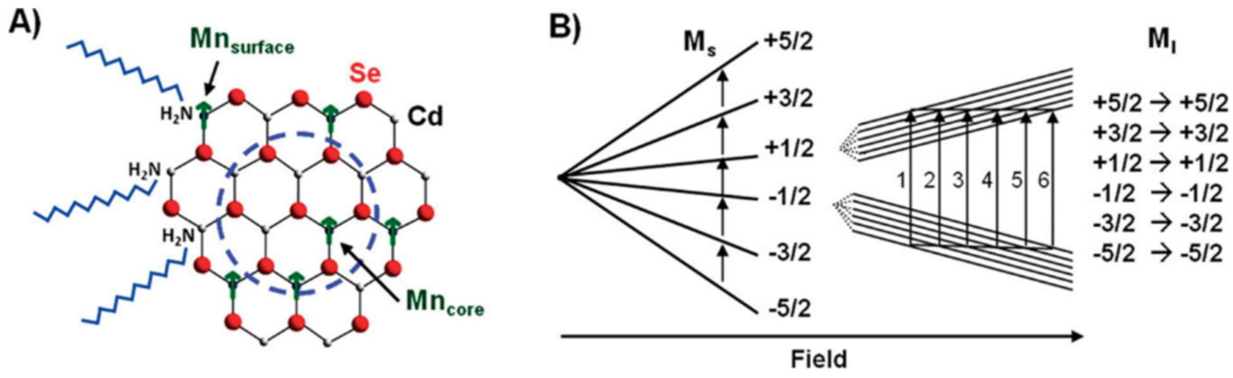

Figure 1.13 (A) A scheme of Mn ions doping into the core and surface site in a Mn:CdSe QD. (B) Schematic illustration of a sextet hyperfine splitting pattern arising from the $S = 5/2$, $I = 5/2$, $L = 0$ ground state ($^6A_1$) for Mn^{2+} ions occupying an approximate tetrahydro site in CdSe lattice.[13]

[13] [Reprinted (adapted) with permission from {Zheng, W.; Wang, Z.; Wright, J.; Goundie, B.; Dalal, N. S.; Meulenberg, R. W.; Strouse, G. F., Probing the Local Site Environments in Mn:CdSe Quantum Dots. J. Phys. Chem. C 2011, 115 (47), 23305-23314.}. Copyright {2011} American Chemical Society.]

There are many challenges to precisely probe the dopant location or the dopant site. Under some conditions, such as a very low dopant concentration in small NCs, there are significant challenges for the analysis for doped NCs, especially mapping the dopant distribution inside NCs.

1.4 Dopant Diffusion and Migration Behaviors within Nanocrystals

Incorporating dopants is a fascinating method to modify and improve the optical, electrical, and magnetic properties of the resulting NCs. Since Bhargava et al. published their report on Mn doping in semiconductor ZnS hosts showing a significant increase in dopant emission intensity in 1994,[125] there have been many efforts to dope various transition metal ions (such as Mn, Cu, Co, Ni, etc.) into different II-VI semiconductor hosts.[127, 175-178]In addition to the physical and chemical properties of dopants, the dopant location and distribution can significantly affect the final properties of doped NCs because of the distance-dependent host-dopant coupling. The specific dopant location-dependent properties can vary depending on the type of host lattice, dopant, and the doping concentration. Dopants located at specific lattice sites can introduce energy levels within the bandgap, affecting the electronic structure and modifying the material's conductivity and/or semiconducting behavior. Dopant location can also influence charge carrier mobility and recombination rates, impacting the material's overall electronic performance. For example, in many QD systems, the QYs of the Mn dopant PL peak around 600 nm are heavily dependent on dopant sites and distribution inside the host lattice. The host-dopant energy transfer by the overlap of exciton wavefunctions of the host lattice and the dopant can lead to new optical properties of doped QDs, which have been found to be heavily dependent on dopant sites and distribution inside the host lattice. Cao et al. found that the optical properties of Mn doped CdS/ZnS core/shell NCs is dopant location-dependent which strongly related to the radial-position of the Mn with the assumption of no doping migration in the core/shell NCs.

Without considering more complicated dopant-dopant interactions and potential phase segregation, several elemental processes including surface adsorption, dopant diffusion/incorporation, and dopant ejection could be involved during the doping procedure, which significantly affect the dopant location and distribution within the lattice.[179]

Impurities may not be successfully introduced into specific lattice due to the process of self-purification, an intrinsic mechanism where impurities are expelled from the lattice. For example, Mn ions can be introduced into a ZnSe NC lattice at high concentrations but introducing any concentration of Mn ions to a CdSe lattice is difficult.[10, 173] The initial adsorption of dopants onto the nanocrystal surface is influenced by the surface morphology, nanocrystal shape, and ligands present in the growth solution.[110] In a kinetic model, the binding energy of dopants with surface ions is the key factor that determine the success of a doping process. For

Mn doped in II-VI semiconductors, the zinc blend crystal structures allow for more effective doping than wurtzite or rock-salt structures due to the binding energy for Mn doping being the largest with the (001) plane of Zinc blend compared with wurtzite or rock-salt lattices.[10, 125, 180] For the lower binding energy in wurtzite structure, polychalcogenide precursors are required to form pre-bonded Mn ions in clusters which would induce a more complicated growth mechanism.[143, 173] In our group's previous work, the temperature- and host composition-dependent dopant migration and ejection process within CdS/ZnS core/shell NCs was studied. It was found that Mn migration toward the CdZnS alloyed interface of the CdS/ZnS core/shell QDs below a temperature boundary (T_b) at ~200 °C, weakens the host-dopant interactions. However, above T_b, dopant ejection can occur accompanied by global alloying of QDs (*i.e.,* CdZnS QDs). Surprisingly, re-strengthened host-dopant coupling was observed even with a decreased doping concentration, which could be understood as the nearly flat band alignment of the globally alloyed of QDs.[14] (Figure 1.14)

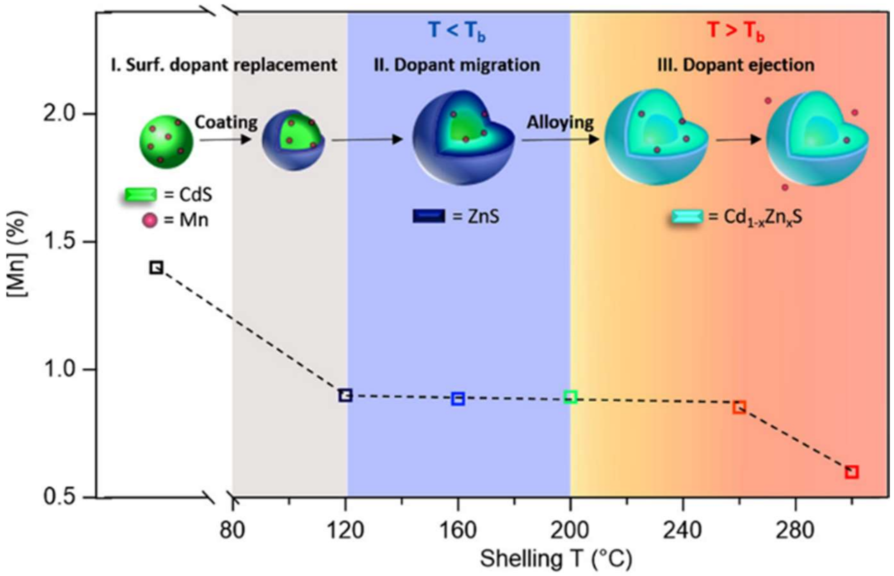

Figure 1.14 Mn doping concentration in Mn doped CdS core and CdS/ZnS core/shell QDs during the shell coating process. Inset: Schematic illustration of three time dependent stages

related to dopant behavior. stage 1: dopant replacement during shell coating, stage 2: dopant migration toward the alloy interface when temperature is below T_b, and stage 3: dopant ejection when temperature is above T_b.[14]

[14] [Reprinted (adapted) with permission from {Hofman, E.; Khammang, A.; Wright, J. T.; Li, Z. J.; McLaughlin, P. F.; Davis, A. H.; Franck, J. M.; Chakraborty, A.; Meulenberg, R. W.; Zheng, W., Decoupling and Coupling of the Host-Dopant Interaction by Manipulating Dopant Movement in Core/Shell Quantum Dots. J. Phys. Chem. Lett. 2020, 11 (15), 5992-5999.}. Copyright {2020} American Chemical Society.]

1.4.1 Dopant ion or atom diffusion in solid lattice

Ion or atom diffusion in a solid lattice involves the movement (hopping) of a cation or atom from one lattice site to another through lattice vacancies, interstitial sites, or grain boundaries. In **vacancy diffusion mechanism**, a dopant moves through the crystal lattice by hopping from one lattice site to a nearby vacant site. **Interstitial diffusion** occurs when ions or atoms move into interstitial sites between existing lattice atoms. Grain boundary diffusion involves the movement of ions or dopants along the boundaries between adjacent crystalline grains (Figure 1.15).[15] The most investigated mechanism for ion diffusion in solid lattice is the cation exchange reaction for the synthesis of nanomaterials.[181-183] Cation exchange reactions provide a method to selectively replace cations in preformed NCs with desired guest cations. These reactions allow for the size, shape, and anion framework of the NCs to be retained while exchanging the cations.[184] Therefore, cation exchange reactions were studied widely on III-V, II-VI, and IV-VI semiconductor NCs, especially for NCs that do not have a more traditional synthetic route.

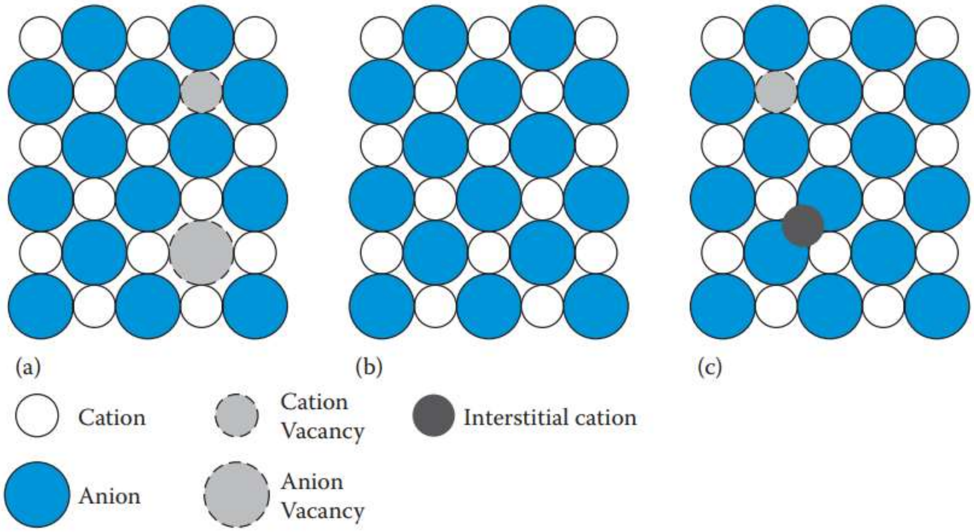

Figure 1.15 Schematic illustration of intrinsic point defects in a crystal of composition.[15]

MX: (a) Schottky pair; (b) perfect crystal; (c) Frenkel pair.

[15][Repurposed with permission from Taylor & Francis Group LLC - Books © 2016]

In a perfect NC, all atoms would be arranged in their ideal lattice position based on the crystal structure; however, this can only exist at the absolute zero of temperature (0 K). Under any real temperature above 0 K, defects occur in the NCs. The imperfections in the crystal lattice, such as vacancies, impurities, interstitials, and/or crystallographic dislocations will improve the occurrence of defects. Dopant atoms may replace host atoms at lattice sites, leading to substitutional defects. In semiconductors, the introduction of dopants causes the formation of extrinsic defects within the crystal lattice, as well as lattice strains resulting in distortion due to the size mismatch between host lattice sites and dopants. The presence of dopants can further alter the local atomic environment, and disrupt the ideal crystal structure, giving rise to defects such as vacancies, dislocations, or stacking faults. For example, after adding Ca^{2+} ions to a NaCl crystal, two Na^+ ions could be replaced by one Ca^{2+} ion, leading to one cation vacancy formation.[15]

1.4.2 Diffusion kinetics and thermodynamics (T, E, C)

Understanding the thermodynamic behavior underlying dopant migration is fundamentally important in materials science, solid-state physics, and device engineering. The thermodynamics of dopant diffusion and migration governs the energetics and kinetics of the migration process, including factors such as temperature, concentration gradients, defect interactions, and lattice structure.[179, 185, 186] Studying these thermodynamic aspects provides valuable insights into the mechanisms and driving forces behind dopant migration. Ion diffusion becomes more fascinating in nanomaterials where there is an increase in surface area and surface-to-volume ratios at the nanoscale, which influences the diffusion kinetics significantly.[15, 187, 188] As the dimensions of materials shrink to the nanoscale, the available diffusion paths within lattices become shorter, leading to accelerated diffusion rates.

The significant amount surface atoms in nanomaterials lead to a higher surface energy compared to their bulk counterparts, which is the excess energy at the surface compared to the interior atoms. Surface energy increases with the particle size decreases, altering the overall energetics of the nanomaterial; this can stabilize certain phases that are not thermodynamically preferred in bulk materials. Compared to the bulk, the large surface-to-volume ratio of nanoparticles possess a substantial fraction of surface atoms, leading to these altered thermodynamic behaviors. For example, a tunable equilibrium composition of $Cd_{1-x}Mn_xSe$ NCs could be prepared under thermodynamic control instead of kinetic control due to the kinetic mismatches between Mn^{2+} and Cd^{2+} chemistries.[181] Mn^{2+} ions can be controlled to diffuse into CdSe NCs without significant Ostwald ripening by managing the chemical potentials of Cd^{2+} and Mn^{2+} in the solution and lattice (Figure 1.16).[181, 185] Under thermodynamic control, the diffusion of impurities is controlled in a quasi-equilibrium condition, driven by entropy. But under kinetic control, impurities were co-added with host ions, partially binding onto the surface through competition with host ions, eventually to be internalized in the lattice via further lattice growth. In addition, the high energy density of interfaces in nanomaterials contributes to thermodynamic effects. Interfaces have excess free energy, which must be considered in predicting phase equilibria. Interfacial free energy and stresses arising from lattice mismatches at internal interfaces can stabilize or destabilize certain phases in nanomaterials. For example, kinetic and thermodynamic stability allow nanomaterials to maintain metastable phases for various applications.

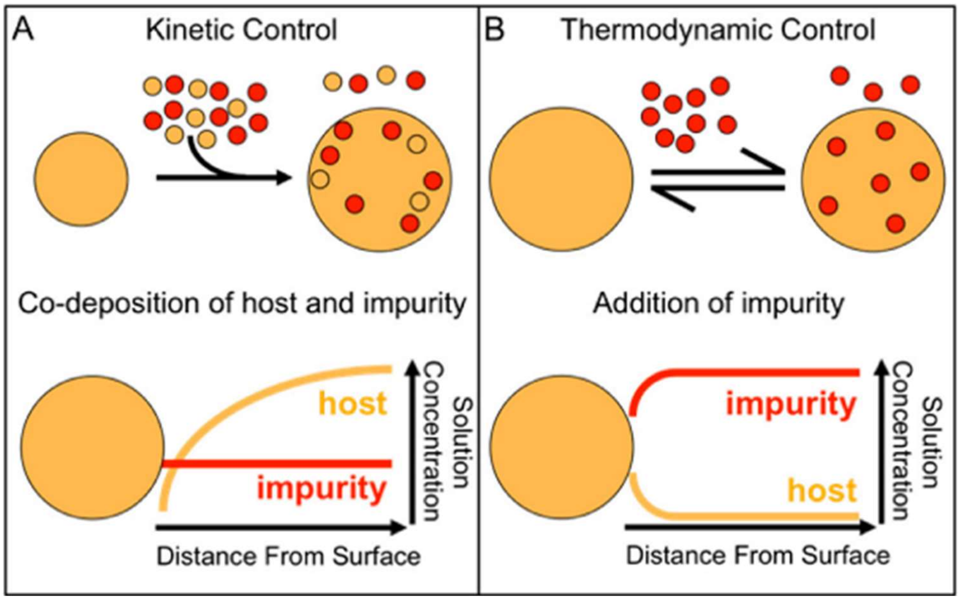

Figure 1.16 Introduction of dopant ions into the host lattice under (a) kinetic control and (b) thermodynamic control.[16]

[16][Reprinted (adapted) with permission from {Vlaskin, V. A.; Barrows, C. J.; Erickson, C. S.; Gamelin, D. R., Nanocrystal diffusion doping. J. Am. Chem. Soc. 2013, 135 (38), 14380-9.}. Copyright {2013} American Chemical Society.]

Dopant diffusion occurs within a lattice with appropriate conditions, including doping concentration, interlayer properties, and reaction/annealing temperature. When such dopants show low-temperature diffuse behavior, they could be defined as 'fast diffusers' with a larger diffusion coefficient. The diffusion coefficient is defined by the Arrhenius equation,

$$D = D_0 e^{(-E_a/RT)} \qquad \text{(eq. 1.5)}$$

Where D_0 is the pre-exponential factor, E_a is the activation energy, R is the universal gas constant, and T is the absolute temperature.[189] Rehman et al. studied the diffusion of Mn ion dopant into ZnS nanostructures and revealed that the diffusion rate of Mn ion is varied due to competition with the growth rate of the NCs.[190] They estimated the diffusion length of Mn using equation 1.6. In the equation, a denotes the step size of Mn ion in ZnS lattice, and Es is the diffusion activation energy. The diffusion rate is proportional to the temperature and disproportionate with activation energy.

$$X = \frac{1}{\sqrt{2}} a e^{(-E_s/RT)} \qquad \text{(eq. 1.6)}$$

The diffusion rate of Mn ions within NCs could be considered as negligible under a typical growth temperature of NCs, *i.e.,* around 300 °C. Jamil and Shaw reported that Mn ions diffusion in CdTe NCs is only 0.1 to 0.3 nm after 1 hour at 300 °C.[110, 187] Under the general colloidal synthesis route, which typically range between 200 and 300 °C, dopant diffusion in solid NC lattices is a very slow process.

1.4.3 Dopant migration behavior in doped core/shell quantum dots

Dopant migration can significantly affect the properties and performance of doped core/shell QDs. Dopant migration is the directional diffusion of dopants within a crystalline lattice. Our group has pioneered the research of dopant migration behaviors in semiconductor NCs to achieve the precise control of the dopant location inside core/shell NCs.[14, 17, 65] In 2017, Hofman *et al.* found that the Mn(II) dopant migration could be facilitated by forming an alloyed interface (*i.e.,* CdZnS) between the CdS core and the ZnS shell inside the core/shell NCs, which reduce the lattice strain caused by the large lattice mismatch (13%) (Figure 1.17).[17]

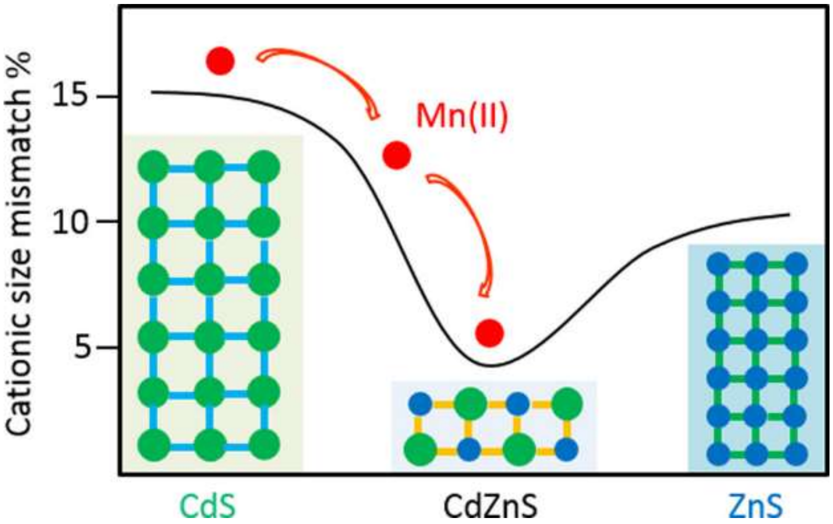

Figure 1.17 Schematic illustration of Mn dopant ions migration from CdS core lattice toward CdZnS alloy interface to reduce the lattice strain.[17]

[17][Reprinted (adapted) with permission from {Hofman, E.; Robinson, R. J.; Li, Z. J.; Dzikovski, B.; Zheng, W., Controlled Dopant Migration in CdS/ZnS Core/Shell Quantum Dots. J. Am. Chem. Soc. 2017, 139 (26), 8878-8885.}. Copyright {2017} American Chemical Society.]

It was found that Mn dopant migration towards the alloyed interface formed between the CdS core and the ZnS shell inside CdS/ZnS core/shell QDs is driven thermodynamically to reduce the lattice strain caused by cationic mismatch between the dopant and host cationic sites. During the shell passivation process, outward dopant migration led to weakened host-dopant coupling due to the larger effective separation between exciton and dopant ions. (i.e. smaller wavefunction overlap between exciton and dopant ions).[14, 17] This discovery indicates manipulating dopant location is highly possible by tuning the local NC lattice parameter and composition. Although the dopant ion migration was found to be thermodynamically driven in CdS/ZnS core/shell QDs, whether the dopant migration can be further controlled by intentionally inserted shell(s) with less size mismatch with dopant is still unknown.

1.5 Summary

1.5.1 Questions remained and challenges of directional dopant migration in nanocrystals

The migration behavior of dopants in nanomaterials, such as II-IV chalcogenides, still provides several questions, despite several reports on the subject.[181, 186, 187, 189-194] While the temperature and lattice mismatch between dopants and host substitutional sites were found to affect dopant migration behavior in a few selective semiconductor NCs, the mechanisms governing dopant diffusion are not yet fully understood. Carefully designing synthetic approaches and post-synthetic treatment processes is critical for precisely controlling doping level and dopant distribution. However, optimizing parameters such as temperature, reaction time, the nature of precursors, and the interactions arising from surface defects and environment is challenging. Additional challenges arise from the lack of a direct probing technique to characterize and verify the dopant concentration and position with possible dopant diffusion, segregation, and self-ejection processes during nanocrystal growth and post-synthetic treatment.

Another question that remains is the dopants behavior in perovskite-based core/shell NCs. Core/shell perovskite NCs have significantly greater environmental stability compared to ionic core perovskite NCs.[195-198] However, given the ionic nature of the perovskite structure and the covalent nature of II-IV chalcogenides, the combination of perovskite with II-IV chalcogenides could leverage the advantages of both materials. In addition, transition metal dopants usually occupy tetrahedral coordination sites in II-VI metal chalcogenide NC lattices, while transition metal dopants in perovskites are doped into octahedral B-sites (ABX_3). The behavior of dopants within this kind of core/shell heterostructure remains largely undeveloped.

The movement of ions within a solid lattice still presents challenges due to several unsettled factors. The first and most notable challenge is the difficulty of achieving precise control over the spatial distribution of dopants within the NC lattice.[16, 199] Dopant ions tend to migrate, eject, or diffuse through the lattice and/or interact with the environment.[200] The various doping strategies and precursors, as well as the post-synthesis treatments, could all alter the doping level and movement of dopants, resulting in a non-uniform distribution. These variabilities can significantly affect the optical and electronic properties, making it difficult to obtain a direct optical illustration to specifically probe the location of dopant ions. Thermal energy is another key factor that affects dopant behaviors within NCs. Under different temperature ranges, dopant ions exhibit a large difference in diffusion coefficients, which will significantly affect the dopant diffusion rate in a solid-state lattice. For example, the diffusion rate of Mn(II) ions could be considered negligible under 300°C, but the rate increases significantly above that temperature.[110, 187] Besides temperature, other parameters, such as reaction time, the nature of the precursors, and various ligands, all play a crucial role in dopant behavior. Dopant migration behavior can also be affected by the chemical environment; for instance, the presence of surfactants and/or solvents in the reaction container can interact with the surface of the QDs and even the size and oxidation states of dopant ions themselves, affecting the diffusion path and process.[201, 202]

1.5.2 Influence of cationic size mismatch between dopants and substitutional sites

The cationic size mismatch between dopant and host cations can significantly influence doping concentration, dopant behavior, and the distribution of dopant ions within the host lattice. In core/shell QDs, an alloyed interface automatically forms between the core and shell lattices to reduce lattice strain caused by the large lattice mismatch.[6, 14, 17, 65] For example, in Mn-doped ZnSe/CdS/ZnS core/shell nanowires (NWs), modifying the composition and creating a cation alloyed CdZnS interface can offer optimal doping sites for Mn ions, minimizing the size mismatch between dopants and the host lattice.[178] Considering the ionic radii of dopant and host cations in Mn-doped CdS/ZnS core/shell QDs, Mn^{2+} (80 pm) exhibits a notable mismatch of approximately 13% with Cd^{2+} (92 pm) and a lesser mismatch of around 5% with Zn^{2+} (74 pm). However, a CdZnS alloyed interface can provide preferable doping site due to a smaller size mismatch with Mn dopants. Consequently Mn ions tend to migrate towards the alloyed interface which is crucial for influencing dopant distribution and location within NC lattice.[17]

A considerable size mismatch between the dopant ion and the host cation it replaces can induce significant lattice strain, leading to crystal lattice distortions. These distortions can potentially affect the material's structural stability, trigger phase transformations, or even create new phases, thus altering the material's intrinsic properties. In an ionic lattice, metal cations occupy sites or polyhedra best fitting their size. Cations might reside in seemingly too-small sites by displacing anions and enlarging the structure, as seen in eutectic structures. Conversely, cations typically avoid overly large sites unless the structure can adapt by reorienting or distorting the anion framework to decrease the site size, a phenomenon observed in various distorted perovskite structures.[15] Our experiments indicates that Mn ions favor smaller mismatch cationic sites for stable doping without migration tendencies. In contrast, when Mn ions are doped into sites with larger mismatches, directional dopant migration is observed under the influence of dopant traps at high temperatures.

1.5.3 Aims of this thesis

This dissertation explores the fundamental understanding underlying dopant ion migration behavior during post-synthetic shell passivation of NCs, specifically by intentionally inserting alloyed atomic traps and doping in the different substitutional sites. We aim to achieve directional dopant migration in NCs by systematically investigating the effect of initial doping sites and the change of the microenvironment from the inserted interface of core/multi-shell QDs. The primary focus of the thesis is on introducing an efficient atomic trap to control directional dopant migration, including both outward and inward dopant movement. In Chapter 2, I describe an outward dopant migration that could be achieved and controlled by inserting an alloyed interface with a smaller cationic size mismatch with Mn as an “atomic trap” within core/shell QDs. In Chapter 3, I will discuss the controlled inward dopant migration through the effects of inserting atomic trap. Furthermore, it was found that the initial doping site and environment is critical for efficient dopant trapping and migration. Specifically, a larger Cd(II) substitutional site (92 pm) for the Mn(II) dopant (80 pm), with larger local lattice distortion, allows for efficient atomic trapping and dopant migration, while Mn(II) dopant ions can be very stable with no significant migration when occupying a smaller Zn(II) substitutional site (74 pm). In Chapter 4, the migration behavior of Mn(II) dopants within CdS/perovskite core/shell and perovskite/CdS core/shell NCs will be discussed. Finally, Chapter 5 will provide a comprehensive conclusion of the project, summarizing key findings and including an outlook on the extended topic for Future study.

Chapter 2

Controlled Outward Dopant Migration in Mn Core Doped Core/Multi-Shell QDs

Reprinted (adapted) with permission from (Chu, C.; Hofman, E.; Gao, C.; Li, S.; Lin, H.; MacSwain, W.; Franck, J. M.; Meulenberg, R. W.; Chakraborty, A.; Zheng, W., Inserting an "atomic trap" for directional dopant migration in core/multi-shell QDs. *Chem Sci* **2023,** *14* (48), 14115-14123.) Copyright (2023) Chemical Science © Royal Society of Chemistry.

Diffusion of atoms or ions in solid crystalline lattice is crucial in many areas of solid-state technology, such as semiconductor manufacturing, batteries, sensors, metallurgy, and heterogeneous catalysis. However, controlling ion diffusion and migration is challenging in nanoscale lattices. In this work, we intentionally insert a CdZnS alloyed interface layer, with small cationic size mismatch with Mn(II) dopant ions, as an “atomic trap” to facilitate ***outward*** dopant migration inside core/ multi-shell QDs to reduce the strain from the larger cationic mismatch between dopants and host sites. The outward dopant migration was achieved by inserting CdZnS alloyed interface in Mn core-doped Mn:CdS/ZnS core/shell QDs (*i.e.*, Mn:CdS/CdZnS/ZnS core/multi-shell QDs). The controlled dopant migration by “atomic trapping” inside QDs provides a new way to fine tune the properties of doped nanomaterials.

2.1 Introduction

At the heart of materials chemistry is the ability to control materials' properties by tuning their chemical composition as reflected by the importance of alloying in metallurgy and doping in modern semiconductor technology.[161, 200, 203] Incorporating dopants inside a nanocrystal (NC) lattice is a fascinating method to modify and improve the optical, electrical, and magnetic properties of the NCs.[22, 28, 110, 111, 141, 161, 200, 203-211]

In addition to the chemical and physical properties of dopants, the dopant location and distribution can also have profound effects on the final properties of doped NCs because of the distance-dependent host-dopant coupling from the wavefunction overlap.[14, 212] For example, in Mn doped metal chalcogenide NCs, the dopant photoluminescence (PL) peak around 600 nm arising from host-to-dopant energy transfer, is strongly influenced by the dopant locations inside the NCs as the energy transfer relies on the spatial overlap between the wavefunctions of the host exciton and dopants.[12, 43, 122, 123, 147, 213] Therefore, the quantum yield (QY) of the Mn dopant PL peak is heavily dependent on the radial position and distribution of Mn ions inside the host lattice.[14, 110, 214] Despite significant developments in the synthesis of doped NCs, dopant behavior after incorporation inside NCs is not well understood. Specifically, the control of dopant location and distribution inside NCs through directional dopant migration is still largely unexplored. Therefore, it is fundamentally important to understand the spatial distribution of dopants in NCs from a synthetic control aspect, and a necessity to understand how dopant manipulation affects the resulting properties.

Theoretically, facilitated dopant diffusion is possible, especially at relatively high temperatures, since the high thermal energy of dopant ions leads to higher hopping frequencies inside the host lattice.[15] In addition, dopant behaviors could be complicated in the host lattice, considering that thermal self-annealing effects can also induce outward movement of dopants in NCs. For example, dopant ejection could happen with extended thermal annealing of Mn doped QDs at high temperatures.[14, 215] However, manipulating dopant location by migration or diffusion inside NC lattice after dopant incorporation is challenging due to the high activation energy of ion diffusion.[110, 151] Additional challenges to control and study the dopant migration behavior pertains to limited analytical techniques available to the detection of the location and distribution of low concentration dopant ions (generally less than five percent) in NCs with high spatial and temporal resolution at the nanoscale.[43, 216-218] Dopant ions inside NC lattice are extrinsic point defects, which could entail a significant local distortion of the structure, especially with a large size mismatch with the host substitutional sites. Therefore, thermodynamically, the point defects can migrate to more ideal substitutional sites with smaller size mismatch.[15] However, whether the directional dopant migration can be controlled by intentionally inserted dopant "trap" layers with less size mismatch is unknown.

In this work, we systematically control the Mn dopant migration by inserting an alloyed interface with a smaller cationic size mismatch with Mn as an "atomic trap" within core/shell QDs for directional Mn dopant migration and therefore dopant location and distribution inside QDs. O*utward* Mn dopant migration behavior was achieved by intentionally inserting a CdZnS alloyed layer into the core-doped core/multi-shell QDs (Scheme 2.1). It is fundamentally important to understand the mechanism of directional dopant migration behavior within NC lattices, which plays a critical role in finely manipulating the properties of the doped NCs.

2.2 Experimental

2.2.1 Chemicals, stock solutions and precursors

Chemicals: $Cd(NO_3)_2 \cdot 4H_2O$ (≥99.0%, Sigma-Aldrich), sulfur powder (99.998%, Sigma-Aldrich), cadmium oxide (CdO, 99.99%, Sigma-Aldrich), zinc oxide (ZnO, ≥99.0%, Sigma-Aldrich), Nitric acid (HNO_3 ,65%, Fisher), oleylamine (OAm, 70%, Sigma-Aldrich), 1-dodecanethiol (DDT, ≥98%, Sigma-Aldrich), oleic acid (OA, 90%, Sigma-Aldrich), 1-octadecene (ODE, 90%, Alfa Aesar), toluene (≥99.5%, Fisher), acetone (≥99.5%, Fisher), ethanol (≥99.5%, VWR), and hexane (>98%, Alfa Aesar) were used as received.

Stock solutions and precursors:

a) ***Sulfur-OAm*** *solution for the synthesis of the CdS core QDs*. 19.5 mg (0.6 mmol) sulfur powder was added into a three-neck flask containing 3 mL OAm. The solution was degassed for 30 minutes at room temperature and then heated to 100 °C under Argon (Ar) and kept stirring at 100 °C for about 3 hours. Then the solution was cooled to room temperature and reheated before injection.[17, 122]

b) ***Sulfur-ODE*** *solution for the synthesis of metal sulfide shells (i.e., CdS, ZnS, and CdZnS shell)*. 32.0 mg (1.0 mmol) sulfur powder was added into a vial which contained 10 mL ODE. The solution was degassed for 30 minutes at room temperature and sonicated at least 2 hours after refilling with Ar.[17, 122]

c) ***Zn precursor*** for the growth of ZnS shell. 81.5 mg (1.0 mmol) zinc oxide was mixed with 9 mL ODE and 1 mL OA in a three-neck flask. After degassing for 1 hour at 100 °C, the solution was heated to 310 °C under Ar. Cooled the solution to the room temperature after it was completely clearly. Reheated the solution to a clear solution before the injection.[17, 122]

d) ***Cd/Zn precursor*** for the growth of CdZnS alloyed shell. 32.0 mg (0.25 mmol) cadmium oxide and 20.3 mg (0.25 mmol) zinc oxide were dissolved in 3.6 mL ODE and 1.25 g OA. After degassing for 1 hour at 100 °C, the solution was heated to 310 °C under Ar. After the solution turned clear, the solution was cooled to room temperature.[17] Reheated the solution to a clear solution before the injection.

2.2.2 Synthesis of Mn core-doped Mn:CdS and Mn:CdS/CdZnS/ZnS core/multi-shell QDs.

Mn(II) doped CdS QDs were synthesized through a colloidal hot-injection technique as previously described.[17] Briefly, 41.2 mg (0.130 mmol) of $Cd(NO_3)_2 \cdot 4H_2O$, 5.82 mg (0.033 mmol) of $Mn(NO_3)_2 \cdot H_2O$, 0.167 mL of DDT, and 10 mL of OAm were mixed in a three-neck flask. The mixture was degassed for 40 min at room temperature and another 10 min at 100 °C. The mixture was refilled with Ar and kept at 110 °C for 30 min. Then, 0.667 mL of a 0.2 M solution of sulfur in OAm was swiftly injected into the flask when the mixture was heated to 160 °C. After the injection, the temperature was set at 120 °C and degassed for 10 min. The temperature was then raised to 240 °C for nanocrystal growth for 5-10 min. The reaction was quenched by removing the heating mantle and submerging the flask in a cold-water bath. After the reaction had been cooled below 100 °C, the product was dissolved in toluene and then crashed out by adding ethanol. The QDs were separated from solutions by centrifugation with a speed set to 5000 rpm at 15 °C for 5 min. The supernatant was discarded and the QDs in the precipitant were redissolved in toluene or hexane, and the cleaning process was repeated 3 more times before shell coating.

A Successive Ion Layer Adsorption and Reaction (SILAR) procedure was used to synthesize core/multi-shell QDs.[17, 122] The as cleaned Mn:CdS core QDs were dissolved in ~1 mL hexane and then transferred into a new three-neck flask with 6 mL of ODE and 2 mL of

OAm. After degassing at 90 °C for 30 minutes, the solution was heated to 100 °C, and continued to degas for another 10 minutes. Next, the solution was refilled with Ar, then the temperature was increased to 180 °C for the following shell growth. For the first CdZnS shell growth, the sulfur-precursor is dropwise injected by the Cd/Zn-precursor alternatively by the volume needed for 1 monolayer (ML) shell. For the following ZnS shell coating, alternating injections of the sulfur-precursor and the zinc-precursor were performed until the desired number of MLs was reached. A 10 °C increment of the reaction temperature was used after each ML shell growth throughout the multi shell growth procedure.

The QDs were cleaned once using toluene/ethanol and redissolved in toluene for optical measurements. For TEM, XRD, and EPR measurements, 4-6 additional washes using toluene/ethanol were performed.

2.2.3 Characterizations

Sample size, morphology, and dispersity were analyzed by transmission electron microscopy (TEM) using a JEOL JEM-2100F TEM which was operated at 200 kV. Powder X-ray diffraction (XRD) patterns were taken on a Bruker D2 Phaser with a LYKXEYE 1-dimensional silicon strip detector using Cu Kα radiation (λ =1.5406 Å). The elemental analysis of the samples was conducted by a PerkinElmer Avio-220 Max inductively coupled plasma-optical emission spectrometry (ICP-OES). For ICP-OES measurements, the powdered samples were completely dissolved in 65% HNO_3, heated to remove excess NO_x, and then diluted with 2% HNO_3 solution.

Agilent Cary 60 UV-vis spectrophotometer was used to collect absorption spectra of the samples in a 1 cm quartz cell. PL measurements were conducted with a Horiba FluroMax Plus spectrofluorometer. Time-resolved emission measurements were performed using an Edinburgh

FLS-980 fluorescence spectrometer equipped with 365 nm picoseconds pulsed lasers (EPLSs) and microsecond flashlamp (μF_2) to measure PL lifetime from a few nano seconds to seconds. Room temperature EPR spectra was performed by a Bruker ELEXSYS-II E500 spectrometer with a microwave frequency of 9.7 GHz.

2.3 Results and Discussion

2.3.1 Mn core-doped core/multi-shell QDs with outward dopant migration by inserting an alloyed "trap" for Mn dopants

In this chapter, Mn core-doped core/shell (Mn:CdS/ZnS QDs) and core/multi-shell (Mn:CdS/CdZnS/ZnS QDs) were designed and the outward dopant migration behavior was studied under the influence of an inserted CdZnS layer as an "atomic trap" within core/multi-shell QDs. (Scheme 2.1)

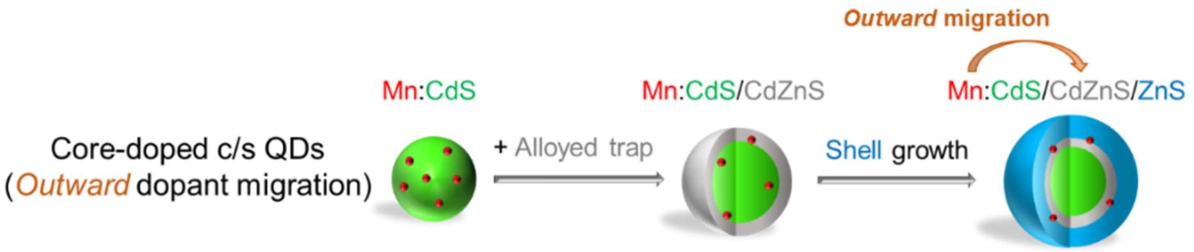

Scheme 2.1 Schematic of Mn core-doped core/multi-shell QDs with outward dopant migration by inserting an alloyed "trap" for Mn dopants.

2.3.2 Structural and morphological characterizations

To facilitate the outward Mn dopant migration, Mn core-doped CdS QDs (*i.e.*, Mn:CdS QDs) were synthesized first, followed by the growth of the CdZnS alloyed trap layer and up to 4 monolayers (MLs) ZnS shell (*i.e.*, Mn:CdS/CdZnS/$ZnS_{(1\text{–}4\ \mathrm{MLs})}$ core/multi-shell QDs) using a successive ionic layer adsorption and reaction (SILAR) method.[106] Mn:CdS/ZnS core/shell QDs without the alloyed shell were also synthesized in control experiments to verify the effect of the alloyed trap layer for dopant migration behavior (see Experimental section). The Mn:CdS QDs have an average size of 3.0 ± 0.3 nm from transmission electron microscopy (TEM) data. After additional 1 ML CdZnS and 4 ML ZnS shell growth, the size of the Mn:CdS/CdZnS/ZnS core/multi-shell QDs increased to 5.6 ± 0.3 nm (Figure 2.1a–c and Figure 2.2a). On average, there is ~0.5 nm increase in diameter for the addition of each shell ML for both Mn:CdS/CdZnS/ZnS and Mn:CdS/ZnS core/multi-shell QDs (Figure 2.2).

Powder X-ray diffraction (XRD) measurements reveal that the Mn:CdS core, Mn:CdS/ZnS$_{(1–5\ \mathrm{MLs})}$ core/shell, and Mn:CdS/CdZnS$_{(1\ \mathrm{ML})}$/ZnS$_{(1–4\ \mathrm{MLs})}$ core/multi-shell QDs possess a cubic phase (Figure 2.1d and Figure 2.3a). XRD patterns of the samples show a gradual peak shift from the cubic CdS to the cubic ZnS phase as the growth of the successive ZnS shell of the QDs. A dampening of the shift toward the ZnS cubic phase occurred when the CdZnS shells were grown on top of the core QDs (*i.e.*, Mn:CdS/CdZnS$_{(1\ \mathrm{ML})}$ QDs) due to the intermediate lattice parameters of the CdZnS, when compared to pure CdS or ZnS lattice based on the Vegard's law,[219] resulting in a smaller total shift (Figure 2.1d and f). In addition, gradual narrowing of the full width at half maximum (FWHM) of the (111) diffraction peaks of the QDs during the successive shell growth (Figure 2.3b) is consistent with the larger QDs obtained after shell passivation.

Inductively coupled plasma-optical emission spectrometry (ICP-OES) measurements indicate the Mn doping concentration is 1.2% for Mn:CdS QDs, which represents ~6 Mn(ii) ions on average in a 3.0 nm Mn:CdS QD distributed statistically between the core and surface of the QD. The Mn(ii) concentration decreases to 0.6% after the addition of the ZnS shell and remains unchanged for the remainder of the CdS/ZnS core/shell QDs. The sudden drop could be attributed to the detachment of the loosely bound surface Mn(ii), resulting in ~3 Mn(II) ions per QD.[122] Interestingly, the Mn:CdS/CdZnS/ZnS$_{(1\text{-}4\ \text{MLs})}$ samples showed a slightly higher Mn(II) concentration of ~0.9%, which represents ~4 Mn(II) ions per core/multi-shell QD with an inserted CdZnS alloyed layer. The increased doping concentration for QDs with an added alloyed layer compared to Mn:CdS/ZnS core/shell QDs with pure, unalloyed ZnS shells can be understood by the CdZnS alloyed shell layer having a more accommodating lattice size for the Mn(II) to assimilate into.[6, 178] It has been reported that the increased Mn(II) dopant concentration within the Zn$_x$Cd$_{1-x}$S alloyed host lattice compared with that in CdS and ZnS QD lattice is due to the reduced cationic size mismatch between the Mn ion and alloyed host lattice.[6, 178]

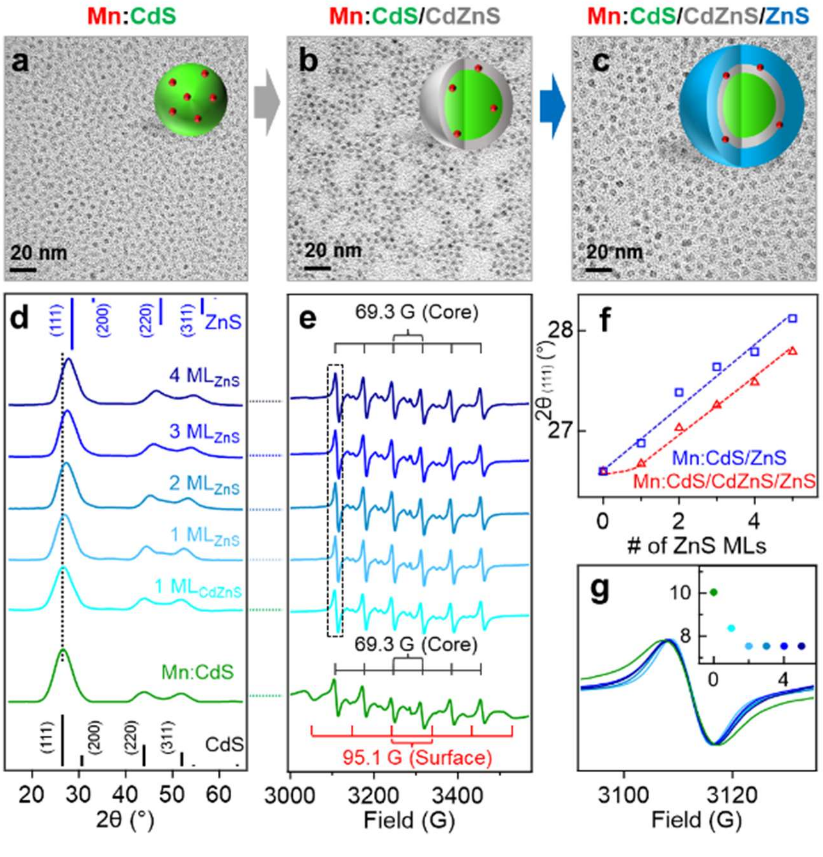

Figure 2.1 (a–c) TEM images of Mn:CdS core, Mn:CdS/CdZnS core/shell, and Mn:CdS/CdZnS/ZnS$_{(4\ \text{MLs})}$ core/multi-shell QDs. (d) XRD patterns and (e) X-band EPR spectra

of Mn:CdS/CdZnS/$ZnS_{(1–4\ MLs)}$ core/multi-shell QDs. (f) The (111) diffraction peak position of the Mn:CdS/ZnS and Mn:CdS/CdZnS/ZnS core/multi-shell QDs as a function of the ZnS shell thickness. (g) The representative first sextet EPR hyperfine peak to display decreasing spectral linewidth with increasing shell thickness, inset shows the EPR hyperfine peak linewidth (in G) as a function of shell monolayers.

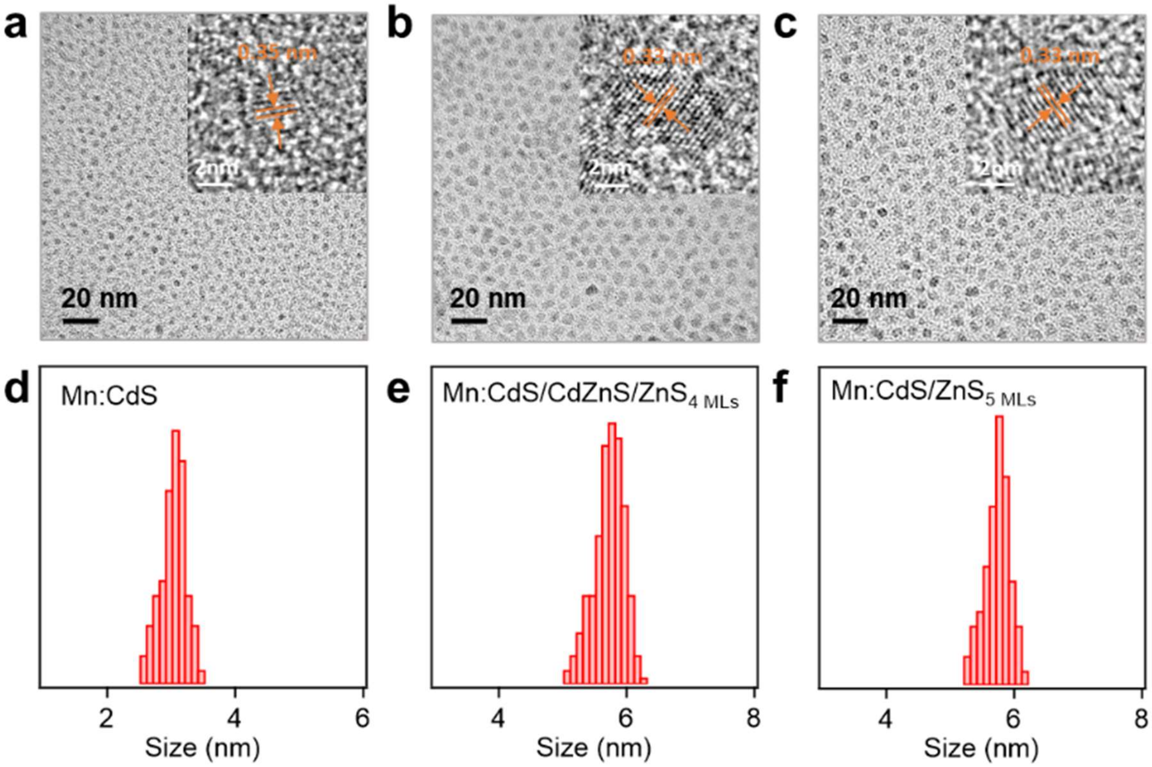

Figure 2.2 TEM Images and histogram of selected (a and d) Mn:CdS core QDs, (b and e) Mn:CdS/CdZnS/$ZnS_{4\ MLs}$ core/multi-shell QDs, (c and f) Mn:CdS/$ZnS_{5\ MLs}$ core/shell QDs. The insets are the high-resolution TEM images showing d-spacing of the (111) lattice plane of the corresponding QDs. (The size of the Mn:CdS core QDs is 3.0 ± 0.3 nm. For Mn:CdS/$ZnS_{5\ MLs}$ core/shell QDs, 5 MLs of ZnS were coated onto the Mn:CdS core with a final size of 5.7 ± 0.3 nm. For Mn:CdS/CdZnS/$ZnS_{4\ MLs}$ core/multi-shell QDs, 1 ML of CdZnS and 4 MLs of ZnS were coated onto the Mn:CdS core with the size of the QDs of 5.6 ± 0.3 nm after shell growth.)

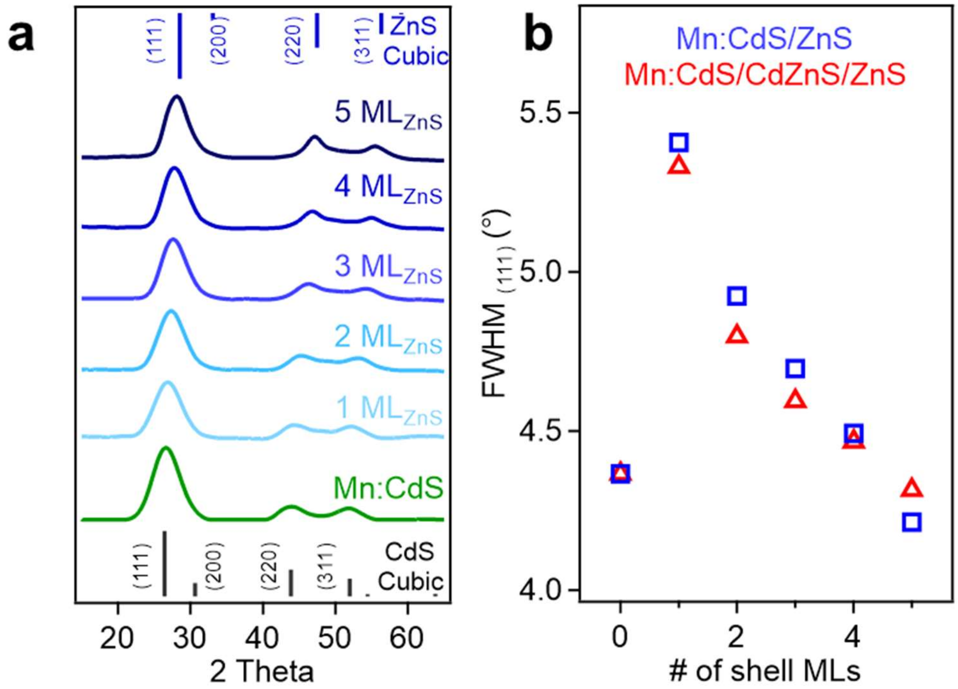

Figure 2.3 (a) XRD patterns of Mn:CdS/ZnS core/shell QDs. (b) XRD analysis of full width at half maximum (FWHM) of the (111) diffraction peak of the Mn:CdS/ZnS and Mn:CdS/CdZnS/ZnS core/multi-shell QDs as a function of the shell thickness.

2.3.3 Optical and EPR spectra for monitoring the dopant location and migration behavior

Electron paramagnetic resonance (EPR) spectrum indicates that Mn ions substitute into both the core and surface lattice of Mn:CdS core QDs with hyperfine splitting constants (A) of 69.3 G and 95.1 G, respectively[6, 13, 43] (Figure 2.1e). During shell passivation, the surface peaks disappeared and only one six-line pattern spectrum with A = 69.3 G remains which indicates successful surface passivation of the Mn:CdS QDs. Interestingly, the linewidth of the EPR hyperfine splitting decreases from 10.0 G for Mn:CdS, to 8.4 G for Mn:CdS/CdZnS, to 7.5 G for Mn:CdS/CdZnS/ZnS$_{(4\ \mathrm{MLs})}$ (Figure 2.1g). Considering no significant change in the average Mn-Mn distance before and after dopant migration in the QDs (~1.6 nm, See Table 2.1, 2.2 with the calculation, and Scheme 2.2), the narrower linewidth of the hyperfine splitting indicates less local strain on the Mn(II) dopant sites during shell passivation,[14, 147] which could imply the change of dopant location to the cationic sites with less cationic size mismatch and strain in the core/multi-shell QDs. EPR spectra of the control Mn:CdS/ZnS$_{(1\text{-}5\ \mathrm{MLs})}$ samples show similar core and surface Mn signals with hyperfine splitting constants of 69.1 G and 96.3 G, respectively (Figure 2.4). However, there is little change of the linewidth of the EPR hyperfine peak (from 10.0 G for the Mn:CdS core to 9.8 G for the Mn:CdS/ZnS core/shell QDs) (Figure 2.4b-c), which indicates a less dramatic change in the Mn dopant bonding environment in Mn:CdS/ZnS$_{(1\text{-}5\ \mathrm{MLs})}$ compared to the Mn:CdS/CdZnS/ZnS$_{(1\text{-}4\ \mathrm{MLs})}$ samples with an inserted alloyed layer.

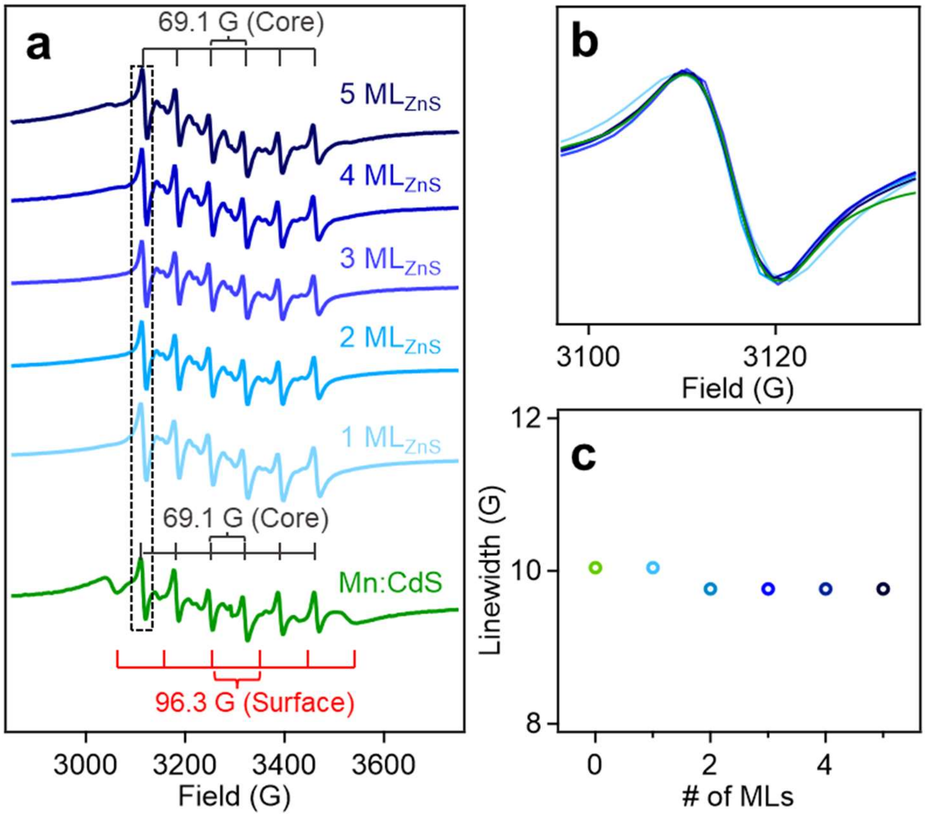

Figure 2.4 (a) Room Temperature X-Band EPR spectra of Mn:CdS/ZnS$_{(1\text{-}5\ \mathrm{MLs})}$ core/shell QDs. Two discrete sites for the Mn(II) occupied a substitutional Cd(II) site within the CdS core (hyperfine splitting constant A is 69.1 G) and surface (A = 96.3 G). During the shell passivation, only the core site, hyperfine splitting constant A = 69.1 G was observed. (b) The representative

first sextet hyperfine peak of EPR spectra to display slightly decreasing spectral linewidth and (c) the EPR spectra linewidth as a function of shell monolayers.

Table 2.1 The average distance between Mn ions inside Mn:CdS core QDs.

Sample	[Mn]	Number of Mn ions per QD (n)	Average volume occupied by Mn ions (V) /nm^3	Average volume occupied per Mn ion (V_{Mn}) /nm^3	Average distance between Mn ions (d_{Mn}) /nm
Mn:CdS	1.2%	6	14.14	2.36	1.65

Table 2.2 The average distance between Mn ions inside Mn:CdS/CdZnS QDs and Mn:CdS/ZnS QDs with outward dopant migration behavior.

Sample	[Mn]	Number of Mn ions per QD (n)	Assuming dopant radial position from the center of a QD/nm	Average surface area occupied per Mn ion (A_{Mn}) /nm^2	Average distance between Mn ions (d_{Mn}) /nm
Mn:CdS /CdZnS	0.9%	4	At the core/shell interface (1.5 nm)	7.07	1.50
			At the midpoint of CdZnS shell (1.63 nm)	8.30	1.63
			At the outer surface of CdZnS shell layer (1.75 nm)	9.62	1.75
Mn:CdS /ZnS$_{(1\ ML)}$	0.6%	3	At the core/shell interface (1.5 nm)	9.42	1.73
			At the midpoint of ZnS shell (1.63 nm)	11.06	1.88
			At the outer surface of ZnS shell layer (1.75 nm)	12.83	2.02

Note: ***Calculation of the average distance between Mn ions within QDs before and after dopant migration.***

For the Mn core-doped CdS QDs, we first calculated the volume (V) of a QD using the equation 2.2,

$$V = \frac{4}{3}\pi r^3 \quad \text{(eq. 2.2)}$$

Where r is the radius of a spherical Mn:CdS QD.

From the Mn doping concentration, we can obtain the number of Mn ions per QD (n). Therefore, the average volume occupied by each Mn ion in the Mn:CdS QDs (V_{Mn}) is:

$$V_{Mn} = \frac{V}{n} = \frac{\frac{4}{3}\pi r^3}{n} = \frac{4}{3}\pi {r_{Mn}}^3 \quad \text{(eq. 2.3)}$$

Therefore, the radius of a sphere of Mn ion (r_{Mn}) occupied is:

$$r_{Mn} = \sqrt[3]{\frac{V_{Mn}}{\frac{4}{3}\pi}} \quad \text{(eq. 2.4)}$$

Using equation 1 to 3, the average Mn-Mn distance in the Mn:CdS QD could be estimated as 2 * r_{Mn}.

After dopants outward migration toward the alloyed layer in Mn:CdS/CdZnS/ZnS and Mn:CdS/ZnS QDs, Mn ions would occupy in a thin shell layer above the CdS core. The surface area of a Mn:CdS/CdZnS$_{(1ML)}$ QD or a Mn:CdS/ZnS$_{(1ML)}$ QD can be calculated using equation 2.5,

$$A_{shell} = 4\pi {r_{QD}}^2 \quad \text{(eq. 2.5)}$$

The average area occupied by each Mn ion can be calculated using equation 2.6. It should be noted that decreased doping concentration after shell coating and the number of Mn ions per core/shell QD is represented as n'.

$$A_{Mn} = A_{shell}/n' \quad \text{(eq. 2.6)}$$

The radius of the circle occupied by a Mn ion (R_{Mn}) is,

$$R_{Mn} = \sqrt{\frac{A_{Mn}}{4\pi}} \quad \text{(eq. 2.7)}$$

Then the average Mn-Mn distance in the shell can be estimated as 2 * R_{Mn}.

ZnS shell coated Mn:CdS/CdZnS QDs, *i.e.* Mn:CdS/CdZnS/$ZnS_{(1\text{-}4\ MLs)}$, have the same dopant concentration, and therefore the same average distance between Mn ions, regardless of the ZnS shell MLs.

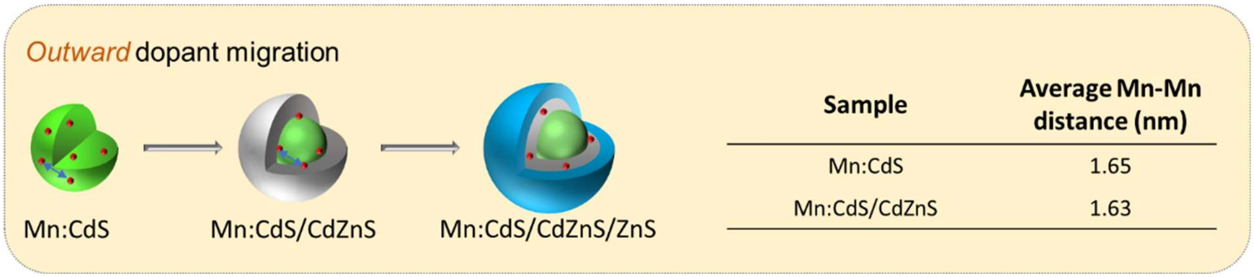

Sample	Average Mn-Mn distance (nm)
Mn:CdS	1.65
Mn:CdS/CdZnS	1.63

Scheme 2.2 Schematic of average Mn-Mn distance before and after outward dopant migration inside core-doped QDs.

Figure 2.5a-2.5b displays the absorption and PL spectra of the Mn:CdS core, Mn:CdS/$ZnS_{(1\text{-}5\ MLs)}$ core/shell, and Mn:CdS/$CdZnS_{(1\ ML)}$/$ZnS_{(1\text{-}4\ MLs)}$ core/multi-shell QDs. The first exciton absorption peak for Mn:CdS core QDs at 405 nm experiences a slight redshift (2 nm) upon the addition of the first ZnS ML onto the core in Mn:CdS/ZnS core/shell QDs (Figure 2.5a). The small spectrum shift could be attributed to the delocalization of the core electrons into the thin CdZnS alloyed interface that is formed between the CdS core and the ZnS shell lattice to reduce the surface strain for the epitaxial growth of the ZnS shell. A larger redshift of the first exciton absorption peak (20 nm shift, from 405 to 425 nm) is observed with the intentional growth of one CdZnS ML directly onto the Mn:CdS QDs for the Mn:CdS/CdZnS/ZnS core/multi-shell QDs (Figure 2.5b), which is consistent with the increased delocalization of the core electrons to the CdZnS alloyed shell with a smaller bandgap compared to that of ZnS lattice.[4]

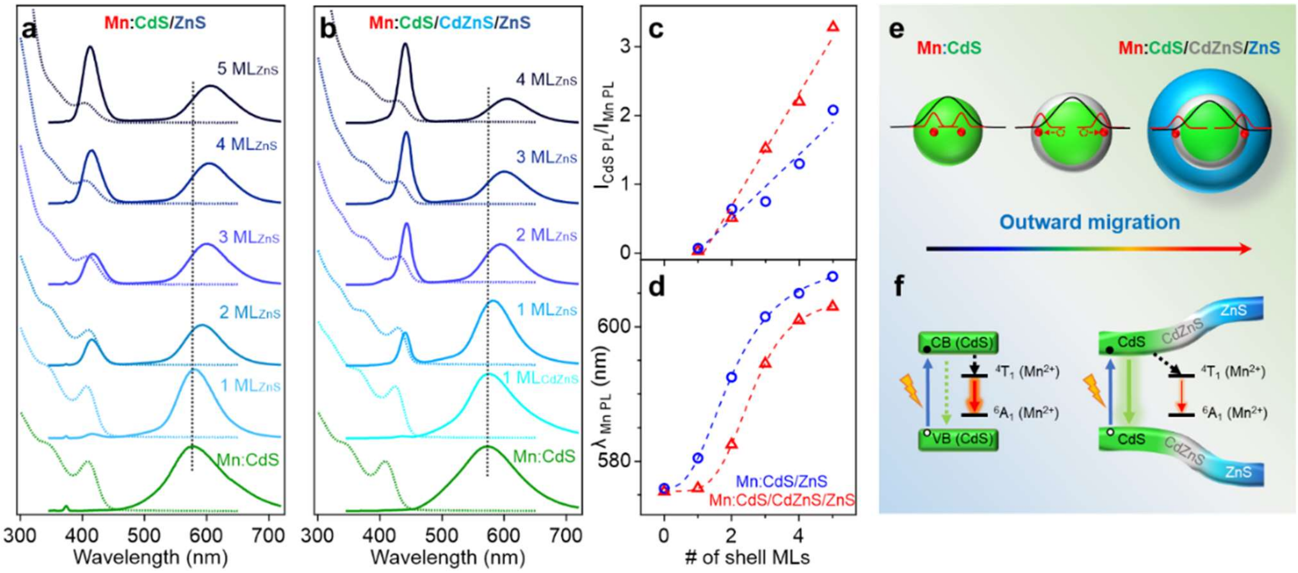

Figure 2.5 (a and b) Normalized absorption (dotted lines) and PL (solid lines) spectra of Mn:CdS/ZnS$_{(1–5\ \mathrm{MLs})}$ and Mn:CdS/CdZnS/ZnS$_{(1–4\ \mathrm{MLs})}$ core/multi-shell QDs, respectively. (c) The PL Intensity ratio of CdS host lattice and Mn(II) and (d) the changes of Mn(II) PL peak position as a function of ZnS and CdZnS/ZnS shell thickness for Mn:CdS/ZnS$_{(1–5\ \mathrm{MLs})}$ and Mn:CdS/CdZnS/ZnS$_{(1–4\ \mathrm{MLs})}$ core/multi-shell QDs, respectively. (e) Schematic of the dopant outward migration by inserted CdZnS alloyed trap layer and (f) the band alignment of the Mn:CdS/CdZnS/ZnS core/multi-shell QDs.

A single broad emission peak centered at 575 nm (FWHM: 112 nm) is observed in the emission spectrum of the Mn:CdS core QDs (Figure 2.5a-b), indicating the presence of surface trap-states overlapping with the Mn(II) emission. An immediate narrowing of the Mn(II) PL FWHM was observed after the first ML shell passivation in both CdS/ZnS and CdS/CdZnS/ZnS QDs (Figure 2.6), indicating the successful surface passivation to remove surface trap-states in the core/shell QDs. A new PL peak from the core CdS QDs at around 420 and 438 nm was observed after the growth of the first ZnS and CdZnS shell for Mn:CdS/ZnS and Mn:CdS/CdZnS/ZnS QDs, respectively.

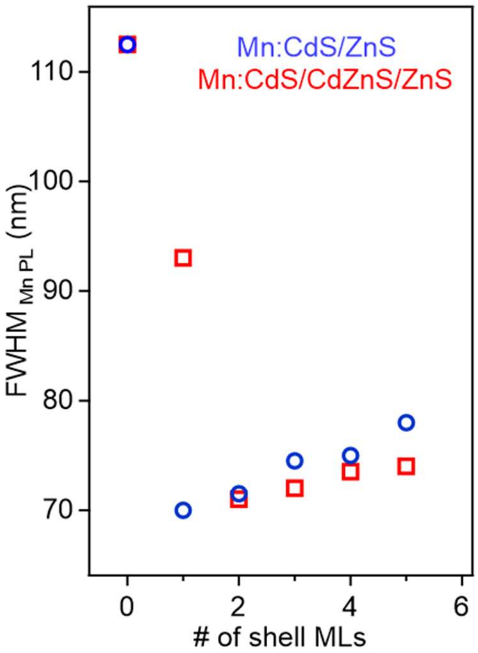

Figure 2.6 FWHM of Mn PL peak for Mn:CdS/ZnS$_{(1\text{-}5\ \mathrm{MLs})}$ and Mn:CdS/CdZnS/ZnS$_{(1\text{-}4\ \mathrm{MLs})}$ core/multi-shell QDs.

Interestingly, the PL ratio of the CdS host and Mn dopants continually changes during shell passivation. Prior to the shelling, the host-dopant coupling is strong as indicated by the single emission band (*i.e.,* $I_{\mathrm{CdS}}/I_{\mathrm{Mn}} = 0$). After the growth of 5 shell MLs, the final CdS to Mn PL ratio ($I_{\mathrm{CdS}}/I_{\mathrm{Mn}}$) reached 2.08 and 3.40 for the Mn:CdS/ZnS$_{(1\text{-}5\ \mathrm{MLs})}$ and Mn:CdS/CdZnS$_{(1\ \mathrm{ML})}$/ZnS$_{(1\text{-}4\ \mathrm{MLs})}$ QDs, respectively (Figure 2.5c). The changes in the PL ratio of CdS QDs and Mn reflects different energy transfer rates between the excitons and Mn ions, which can be understood using equation 2.1:[151]

$$\frac{I_{Mn}}{I_{QD}} = n\Phi_{Mn}\frac{k_{ET}}{k_{UD-R}}\frac{\lambda_{QD}}{\lambda_{Mn}} \qquad \text{(eq. 2.1)}$$

Where I_{Mn} and I_{QD} are intensities of Mn and host band-gap PL of the doped QDs, respectively; n is the number of Mn ions doped inside one NC; λ_{QD} is the wavelength of the host QD PL, λ_{Mn} is the wavelength of the Mn emission; Φ_{Mn} is the emission efficiency of a Mn ion;

$k_{\mathrm{UD\text{-}R}}$ is the radiative relaxation rate constant of undoped NCs; and k_{ET} is the rate constant for the energy transfer from an exciton to a Mn ion. Considering small changes in the host and dopant PL position, and constant doping concentrations in core/shell NCs, the k_{ET} between host QDs and Mn(II) dopants can be held proportional to the PL ratio amid the Mn and host lattice ($k_{\mathrm{ET}} \propto I_{\mathrm{Mn}}/I_{\mathrm{BG}}$).[43, 147, 220] k_{ET} is related to the overlap between the wavefunctions of the exciton and Mn dopants,[220] and thus the distance between exciton and Mn ions. Therefore, the ratio of Mn(II) to host PL reflects the degree of host-to-dopant energy transfer rate and can be used as an "optical gauge" to monitor dopant location and dopant migration behavior inside core/shell QDs.[17] The dramatically increased PL ratio of CdS and Mn in Mn:CdS/CdZnS$_{(1\ \mathrm{ML})}$/ZnS$_{(4\ \mathrm{ML})}$ core/multi-shell QDs (from 0 to 3.40) indicates the decreased energy transfer efficiency (K_{ET}) and the host-dopant coupling due to the larger separation between the core and dopant ions during *outward* dopant ion migration (Figure 2.5e and f).

The driving force of Mn(II) ions migration to the CdZnS shell is that the size of the Mn(II) ions (80 pm) is between that of Cd(II) (92 pm) and Zn(II) (74 pm).[221] Considering the nearly linear composition-dependent lattice parameter of the alloy phase based on Vegard's law,[222] the alloyed shell would then have intermediate lattice parameters with a cation size between that of Cd(II) and Zn(II). The Mn(II) migration from the CdS core to the alloyed shell is thermodynamically favored since it minimizes the lattice strain caused by the large size difference (13%) between Cd(II) and Mn(II) (Scheme 2.3).[178] The moderately increased $I_{\mathrm{CdS}}/I_{\mathrm{Mn}}$ (2.08) in the Mn:CdS/ZnS$_{(5\ \mathrm{ML})}$ core/shell QDs without inserting the CdZnS alloyed layer could be understood by Mn migration to a thin alloyed interface ($Cd_xZn_{1-x}S$) formed by ion diffusion and exchange to release the strain caused by lattice mismatch (7% between CdS and ZnS), which is consistent with a small blueshift of the host PL. The elevated $I_{\mathrm{CdS}}/I_{\mathrm{Mn}}$ ratio in Mn:CdS/CdZnS$_{(1}$

$_{ML)}$/ZnS$_{(4\ ML)}$ core/multi-shell QDs can be attributed to the greater distance travelled by the dopant ions in the presence of an inserted alloyed “trap” shell.

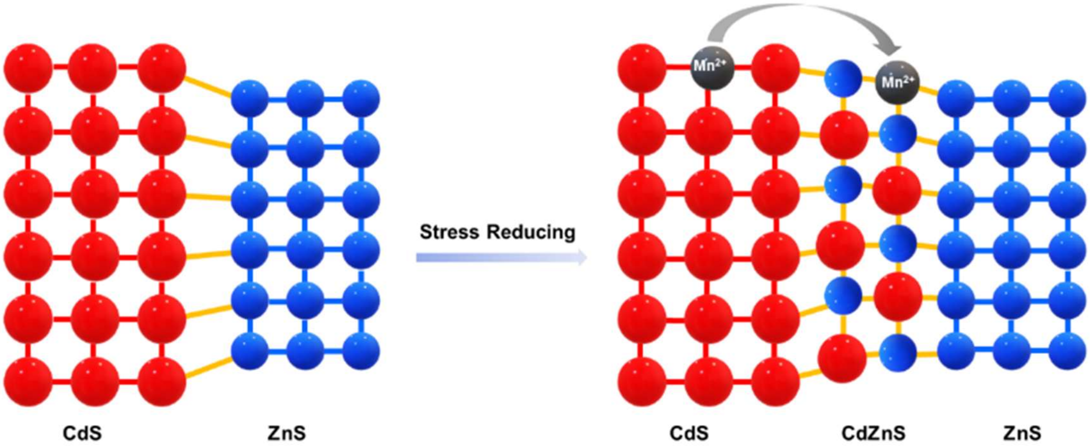

Scheme 2.3 Schematic of inserting an alloyed CdZnS layer to reduce the lattice strain between CdS and ZnS lattice.

It should be noted that the nonradiative relaxation and surface defect emission could compete with the host-dopant energy transfer.[223] To verify that the change of the Mn-to-host PL ratio (as an “optical gauge” for dopant location) is due to dopant migration inside core/shell QDs instead of simple elimination of surface traps on the core QDs during shell coating, we performed a control experiment of undoped core/multi-shell QDs with the same core and shell composition and sizes. During the ZnS shell passivation, PL QYs for both the doped and undoped QDs increased from ~5% to ~30% with the increase of the shell thickness (Figure 2.7). The total PL QYs of Mn doped CdS/CdZnS/ZnS and CdS/ZnS QDs are similar to that of undoped QDs with the same shell thickness. Therefore, the changes in the ratio between host and Mn PL in the Mn:CdS/CdZnS/ZnS QDs can be explained by the different host-dopant energy transfer efficiency within the core/shell QDs due to the dopant migration towards alloyed layer, as the distance and wavefunction overlap between the core CdS and Mn dopant ions changes (Figure 2.5e).

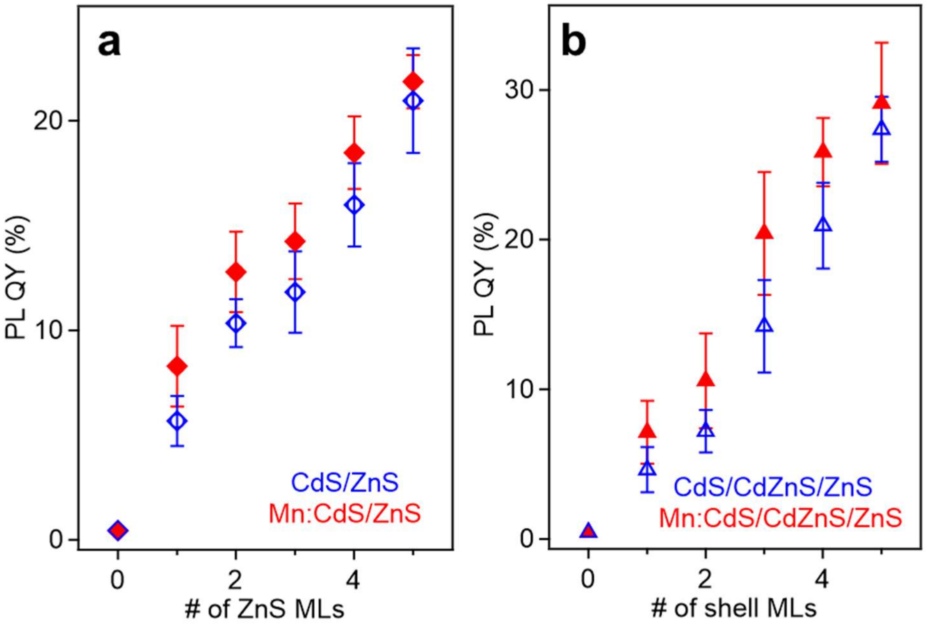

Figure 2.7 PL QYs of (a) undoped CdS/ZnS$_{(1\text{-}5\ \mathrm{MLs})}$ and doped Mn:CdS/ZnS$_{(1\text{-}5\ \mathrm{MLs})}$ core/multi-shell QDs without an inserted alloy dopant trap, and (b) undoped CdS/CdZnS/ZnS$_{(1\text{-}4\ \mathrm{MLs})}$ and doped Mn:CdS/CdZnS/ZnS$_{(1\text{-}4\ \mathrm{MLs})}$ core/multi-shell QDs with an inserted CdZnS alloy dopant trap as a function of ZnS monolayers, respectively.

Interestingly, it was found that the PL QYs of Mn doped core/shell QDs are slightly higher than their undoped counterparts regardless of the presence of the CdZnS alloyed trap layer. The slightly higher PL QY of Mn doped QDs compared with undoped ones is attributed to the fast host-dopant energy transfer that efficiently competes with nonradiative relaxation pathways, which is consistent with a previous report.[123]

The radial position of the Mn dopants inside the core/shell QDs can also be monitored by the Mn PL peak position because Mn PL is very sensitive to the shell applied pressure (proportional to shell thickness) based on the spherically symmetric elastic continuum model.[136]

Dubertret *et al.* found that the additional pressure from the outside ZnS shell on the Mn dopants in Mn doped CdS/ZnS core/shell QDs slightly narrows the crystal field splitting of the Mn(II) d-d transition (from $^4T_1$ to $^6A_1$), causing a redshift in the Mn(II) PL.[136] The Mn PL of the Mn:CdS/ZnS core/shell QDs exhibit a rapid red-shift (~30 nm) followed by gradual plateauing during the shelling process. However, no significant red-shift of Mn PL peak occurred after initial CdZnS alloyed shell passivation, and had a smaller total Mn PL red-shift of 28.5 nm for the ZnS shelled Mn:CdS/CdZnS$_{(1\ ML)}$/ZnS$_{(4\ ML)}$ core/multi-shell QDs (Figure 2.5d). The decreased red-shift caused by the inserted CdZnS shell indicates a decrease in total shell-induced pressure on the dopants, which is consistent with "*outward*" dopant migration within the core/multi-shell QDs.

2.4 Conclusion

In this work, outward dopant migration behavior was achieved using an alloyed layer with a small cationic size mismatch with the dopant ions in Mn core-doped core/multi-shell QDs. The inserted alloyed shell (CdZnS) with smaller cationic size mismatch with the dopants can serve as an "atomic trap" to the dopant ions to reduce the strain from the larger cationic mismatch between Mn(ii) ions and host sites. This work represents the first controlled outward dopant migration behavior in NC lattice by intentionally inserting an "atomic trap" for dopant ions. Controlled dopant migration inside NC lattice provides a new way to fine tune the properties of doped QDs.

Chapter 3

Controlled Inward Dopant Migration by Inserting an "Atomic Trap" in Mn Shell Doped Core/Multi-Shell QDs

Reprinted (adapted) with permission from (Chu, C.; Hofman, E.; Gao, C.; Li, S.; Lin, H.; MacSwain, W.; Franck, J. M.; Meulenberg, R. W.; Chakraborty, A.; Zheng, W., Inserting an "atomic trap" for directional dopant migration in core/multi-shell QDs. *Chem Sci* **2023,** *14* (48), 14115-14123.) Copyright (2023) Chemical Science © Royal Society of Chemistry.

Diffusion of atoms or ions in solid crystalline lattice is crucial in many areas of solid-state technology. However, controlling ion diffusion and migration is challenging in nanoscale lattices. In this work, we intentionally insert a CdZnS alloyed interface layer, with small cationic size mismatch with Mn(II) dopant ions, as an “atomic trap” to facilitate directional (outward and inward) dopant migration inside core/multi-shell QDs to reduce the strain from the larger cationic mismatch between dopants and host sites. Furthermore, it was found that the initial doping site/environment is critical for efficient dopant trapping and migration. Specifically, a larger Cd(II) substitutional site (92 pm) for the Mn(II) dopant (80 pm), with larger local lattice distortion, allows for efficient atomic trapping and dopant migration, while Mn(II) dopant ions can be very stable with no significant migration when occupying a smaller Zn(II) substitutional site (74 pm). Density functional theory calculations revealed a higher energy barrier for a Mn(II) dopant hopping from the smaller Zn substitutional tetrahedral (T_d) site as compared to a larger Cd substitutional T_d site. The controlled dopant migration by “atomic trapping” inside QDs provides a new way to fine tune the properties of doped nanomaterials.

3.1 Introduction

Doped semiconductor NCs are acknowledged as a crucial class of nanomaterials, attracting interest for investigations ranging from fundamental understanding to applications in renewable energy.[9, 45, 52, 56, 97, 110, 188, 200, 224, 225] The incorporation of intentional impurities, known as dopants, to regulate the characteristics of materials lies in the center of nanomaterials. Impurity doping in semiconductor QDs (QDs) has attracted numerous interests for manipulating and enhancing their properties, offering a versatile avenue for technological advancements. The intentional introduction of impurity ions into the quantum dot lattice has gained increasing attention due to its ability to obtain desirable characteristics, such as optical,[10, 125, 226] magnetic,[143, 227, 228] electrical,[121] and electronic[229, 230] properties.

Despite significant developments in the synthesis of doped NCs, dopant behavior after incorporation inside NCs is not well understood. Specifically, the control of dopant location and distribution inside NCs through directional dopant migration is still largely unexplored. Therefore, it is fundamentally important to understand the spatial distribution of dopants in doped NCs from a synthetic control aspect, and a necessity to understand how dopant manipulation affects the resulting properties. Dopant ions inside NC lattice are extrinsic point defects, which could entail a significant local distortion of the structure, especially with large size mismatch with host substitutional sites. Therefore, thermodynamically, the point defects can migrate to more ideal substitutional sites with smaller size mismatch. However, manipulating dopant location by migration or diffusion inside NC lattice after dopant incorporation is challenging due to the high activation energy of ion diffusion. Theoretically, facilitated dopant diffusion is possible especially at relatively high temperatures since the high thermal energy of dopant ions leads to higher hopping frequencies inside the host lattice.[15] Furthermore, high temperature conditions can lead to higher concentrations of intrinsic defects such as vacancies, which typically provide a lower-energy pathways for diffusion through a structure that does not involve the energy penalties associated with continuously displacing ions from normal ion sites.

Additional challenges to control and study the dopant migration behavior pertain to limited analytical techniques available to detect the location and distribution of dopant ions in NCs with high spatial and temporal resolution at the nanoscale. Electron paramagnetic resonance (EPR) is a powerful technique to detect transition metal dopants with unpaired electrons and can even reveal spin interactions that are sensitive to the local microenvironments in lattice. For example, EPR can distinguish the surface and core Mn dopant sites in many II-VI group NC lattice.[6, 13, 43] However, EPR cannot provide detailed information of the dopant location(s) including the depth of a dopant ion inside a NC.

Previously our group developed a sensitive "optical gauge", *i.e.,* the changes in the PL ratio of host CdS QDs and Mn dopants, to probe dopant location and distribution of Mn dopant ions in Mn:CdS QDs during ZnS shell passivation.[17] The changes in the PL ratio of CdS QDs and Mn reflects different energy transfer rate between the exciton and Mn ions, which can be understood using equation 2.1.[151] Considering small changes in the host and dopant PL position, and constant doping concentration in core/shell NCs, the k_{ET} between host QDs and Mn(II) dopants can be held proportional to the PL ratio amid the Mn and host lattice ($k_{\mathrm{ET}} \propto I_{\mathrm{Mn}}/I_{\mathrm{BG}}$).[43, 147, 220] k_{ET} is related to the overlap between the wavefunctions of the exciton and Mn dopants,[220] and thus the distance between exciton and Mn ions. Therefore, the ratio of Mn(II) to host PL reflects the degree of host-to-dopant energy transfer rate and can be used as an "optical gauge" to monitor dopant location and dopant migration behavior inside core/shell QDs.

As a proof of concept, previously, we used the PL ratio of host CdS QDs and Mn dopants to visualize gradual *outward* dopant migration behavior from CdS core lattice towards the formed alloyed interface (CdZnS) in the Mn core-doped Mn:CdS/ZnS core/shell QDs during shell passivation.[17] It was believed that the Mn(II) could migrate to substitutional sites with smaller cationic size mismatch to reduce the strain from the larger cationic mismatch between Mn(II) ions (80 pm) and substitutional Cd(II) ion sites (92 pm). The *outward* dopant migration led to the weakened host-dopant energy transfer due to the larger effective separation between exciton and dopant ions. (*i.e.,* smaller wavefunction overlap between exciton and dopant ions), which is evidenced by the gradually decreased $I_{\mathrm{Mn}}/I_{\mathrm{BG}}$ in the PL spectra. Nevertheless, dopant behaviors could be complicated in the host lattice, considering thermal self-annealing effects can also induce outward movement of dopants in NCs. For example, dopant ejection could happen with extended thermal annealing of Mn doped QDs.[14, 215] Therefore, to confirm the role of cationic size mismatch for the dopant behavior, it is critical to achieve the control of the *inward* dopant migration in NC lattice. So far, the controlled *inward* Mn dopant migration behavior is still unexplored. In addition, whether the directional (both *inward* and *outward*) dopant migration and the migration rate can be further controlled by intentionally inserted dopant “trap” layers with less size mismatch is unknown.

In this work, we systematically controlled the Mn dopant migration by inserting an alloyed interface as an “atomic trap” within core/muti-shell QDs for inward Mn dopant migration and therefore dopant location and distribution inside QDs. Our hypothesis is that the inserted CdZnS alloyed shell with small cationic size mismatch with Mn can provide a better substitutional site for Mn dopants, which can serve a dopant “trap” to initiate fast dopant migration under moderate temperatures. *Inward* Mn dopant migration behaviors were achieved by intentionally inserting a CdZnS alloyed layer into the shell doped core/multi-shell QDs (Scheme 3.1). More importantly, it was found that the initial doping site and environment is critical for efficient "atomic trapping" and dopant migration. Specifically, a larger initial substitution site for Mn(II) dopants, for example Cd(II) site (92 pm), with larger local lattice distortion, allows for efficient atomic trapping and dopant migration, while Mn(II) dopant ions can be very stable with no significant migration occurring when occupying a slightly smaller substitutional site, such as Zn(II) site (74 pm). Theoretical simulations indicate a significantly high energy barrier for dopant hopping through a triangle face of a small substitutional tetrahedral (T_d) site. It is fundamentally important to understand the mechanism of directional dopant migration behavior within NC lattice, which plays a critical role in finely manipulating the properties of the doped NCs.

3.2 Experimental

3.2.1 Chemicals, stock solutions and precursors

Chemicals: $Cd(NO_3)_2 \cdot 4H_2O$ (≥99.0%, Sigma-Aldrich), $Mn(CH_3CO_2)_2$ (>98%, Alfa Aesar), sulfur powder (99.998%, Sigma-Aldrich), cadmium oxide (CdO, 99.99%, Sigma-Aldrich), zinc oxide (ZnO, ≥99.0%, Sigma-Aldrich), HNO_3 (65%, Fisher), oleylamine (OAm, 70%, Sigma-Aldrich), 1-dodecanethiol (DDT, ≥98%, Sigma-Aldrich), oleic acid (OA, 90%, Sigma-Aldrich), 1-octadecene (ODE, 90%, Alfa Aesar), toluene (≥99.5%, Fisher), acetone (≥99.5%, Fisher), ethanol (≥99.5%, VWR), and hexane (>98%, Alfa Aesar) were used as received.

Stock solutions and precursors:

a) ***Sulfur-OAm*** *solution for the synthesis of the CdS core QDs*. 19.5 mg (0.6 mmol) sulfur powder was added into a three-neck flask containing 3 mL OAm. The solution was degassed for 30 minutes at room temperature and then heated to 100 ℃ under Argon (Ar) and kept stirring at 100 ℃ for about 3 hours. Then the solution was cooled to room temperature and reheated before injection.[17, 122]

b) ***Sulfur-ODE*** *solution for the synthesis of metal sulfide shells (i.e., CdS, ZnS, and CdZnS shell)*. 32.0 mg (1.0 mmol) sulfur powder was added into a vial which contained 10 mL ODE. The solution was degassed for 30 minutes at room temperature and sonicated at least 2 hours after refilling with Ar.[17, 122]

c) ***Zn precursor*** for the growth of ZnS shell. 81.5 mg (1.0 mmol) zinc oxide was mixed with 9 mL ODE and 1 mL OA in a three-neck flask. After degassing for 1 hour at 100 ℃, the solution was heated to 310 ℃ under Ar. Cooled the solution to the room temperature after it was completely clearly. Reheated the solution to a clear solution before the injection.[17, 122]

d) ***Cd/Zn precursor*** for the growth of CdZnS alloyed shell. 32.0 mg (0.25 mmol) cadmium oxide and 20.3 mg (0.25 mmol) zinc oxide were dissolved in 3.6 mL ODE and 1.25 g OA. After degassing for 1 hour at 100 ℃, the solution was heated to 310 ℃ under Ar. After the solution turned clear, the solution was cooled to room temperature.[17] Reheated the solution to a clear solution before the injection.

e) ***Cd precursor*** for the growth of CdS shell. 32.0 mg (0.25 mmol) cadmium oxide was dissolved in 1.8 mL ODE and 0.62 g OA. After degassing for 1 hour at 100 ℃, the solution was heated to 280 ℃ under Ar. After the solution turned clear, the solution was cooled to room temperature. Reheated the solution to a clear solution before the injection.[17, 122]

f) ***Mn precursor*** (Mn acetate in OAm) for shell doping. OAm (8 mL) was added into a three-neck flask and degassed at room temperature for 10 minutes followed by degassing at 120 °C for additional 10 minutes. 7 mg (0.04 mmol) anhydrous Mn $(CH_3CO_2)_2$ was quickly added into the flask at room temperature. After degassing at room temperature for 10 minutes and an additional 10 minutes at 120 °C, the solution was cooled to room temperature.[17, 122] Note: The Mn precursor solution should be freshly made just before the injection.

3.2.2 Synthesis of Mn shell-doped and undoped core/multi-shell quantum dots

a) Synthesis of undoped CdS core QDs. Undoped CdS QDs were synthesized through a colloidal hot-injection technique as previously described with slight modification.[17] Briefly, 41.2 mg (0.130 mmol) of Cd $(NO_3)_2 \cdot 4H_2O$, 0.167 mL of DDT, and 10 mL of OAm were mixed in a three-neck flask. The mixture was degassed for 40 min at room temperature and another 10 min at 100 °C. The mixture was refilled with Ar and kept at 110 °C for 30 min. Then, 0.667 mL of a 0.2 M solution of sulfur in OAm was swiftly injected into the flask when the mixture was heated to 160 °C. After the injection, the temperature was set at 120 °C and degassed for 10 min. The temperature was then raised to 240 °C for nanocrystal growth for 5-10 min. The reaction was quenched by removing the heating mantle and submerging the flask in a cold-water bath. After the reaction had been cooled below 100 °C, the product was dissolved in toluene and then crashed out by adding ethanol. The QDs were separated from solutions by centrifugation with a speed set to 5000 rpm at 15 °C for 5 min. The supernatant was discarded and the QDs in the precipitant were redissolved in toluene or hexane, and the cleaning process was repeated 3 more times before shell coating.

b) Shell growth. A Successive Ion Layer Adsorption and Reaction (SILAR) procedure was used to synthesize core/multi-shell QDs.[17, 122] The as cleaned CdS core QDs were dissolved in ~1 mL hexane and then transferred into a new three-neck flask with 6 mL of ODE and 2 mL of OAm. After degassing at 90 °C for 30 minutes, the solution was heated to 100 °C, and continued to degas for another 10 minutes. Next, the solution was refilled with Ar, then the temperature was increased to 180 °C for the following shell growth. For the first CdZnS shell growth, the sulfur-precursor is dropwise injected by the Cd/Zn-precursor alternatively by the volume needed for 1 monolayer (ML) shell. For the following ZnS shell coating, alternating injections of the sulfur-precursor and the zinc-precursor were performed until the desired number of MLs was reached. A 10 °C increment of the reaction temperature was used after each ML shell growth throughout the multi shell growth procedure. The QDs were cleaned once using toluene/ethanol and redissolved in toluene for optical measurements. For TEM, XRD, and EPR measurements, 4-6 additional washes using toluene/ethanol were performed.

c) For CdS/CdZnS/Mn:ZnS/ZnS core/multi-shell QDs with Mn doped into ZnS shell, the as-cleaned CdS core QDs were dissolved in ~1 mL hexane and then transferred into a new three-neck flask with 6 mL of ODE and 2 mL of OAm. After degassing at 90 °C for 30 minutes, the solution was heated to 100 °C, and degassed for another 10 minutes. Next, the solution was refilled with Ar, then the temperature was increased to 180 °C for the following shell growth using a SILAR procedure.[17, 122] For the first CdZnS shell growth, the sulfur-precursor was dropwise injected by the Cd/Zn-precursor alternatively by the volume needed for 1 ML shell. The Mn-Zn-precursor was injected dropwise for the Mn:ZnS shell. The CdS/CdZnS/Mn:ZnS QDs were cleaned using toluene/acetone to remove unreacted Mn and shell precursors and the cleaned QDs were transfer into a new three-neck flask for the following ZnS shell coating. For the following ZnS shell coating, alternating injections of the sulfur-precursor and the zinc-precursor were performed until the desired number of MLs was reached. A 10 °C increment of the solution temperature occurred after each ML shell growth throughout the multi shell growth procedure.

d) For the synthesis of the CdS/CdZnS/Mn:CdS/ZnS core/multi-shell QDs with Mn doped into CdS shell, the same procedure using the SILAR method was used except the Mn doped CdS layer was grown in the second shell by dropwise injecting the mixture of CdO and Mn-precursor. For control experiments without CdZnS alloyed trap layer, a CdS or ZnS layer was grown to replace the CdZnS layer in **CdS/CdS/Mn:CdS/ZnS** and **CdS/ZnS/Mn:ZnS/ZnS core/multi-shell QDs**, respectively. The same sample purification method was adopted for the shell doped core/multi-shell QDs as for the Mn core-doped core/multi-shell QDs.

3.2.3 Characterizations

Sample size, morphology, and dispersity were analyzed by transmission electron microscopy (TEM) using a JEOL JEM-2100F TEM which was operated at 200 kV. Powder X-ray diffraction (XRD) patterns were taken on a Bruker D2 Phaser with a LYKXEYE 1-dimensional silicon strip detector using Cu Kα radiation (λ =1.5406 Å). The elemental analysis of the samples was conducted by a PerkinElmer Avio-220 Max inductively coupled plasma-optical emission spectrometry (ICP-OES). For ICP-OES measurements, the powdered samples were completely dissolved in 65% HNO_3, heated to remove excess NO_x, and then diluted with 2% HNO_3 solution.

Agilent Cary 60 UV-vis spectrophotometer was used to collect absorption spectra of the samples in a 1 cm quartz cell. PL measurements were conducted with a Horiba FluroMax Plus spectrofluorometer. Time-resolved emission measurements were performed using an Edinburgh FLS-980 fluorescence spectrometer equipped with 365 nm picoseconds pulsed lasers (EPLSs) and microsecond flashlamp (μF_2) to measure PL lifetime from a few nano seconds to seconds.

Room temperature EPR spectra was performed by a Bruker ELEXSYS-II E500 spectrometer with a microwave frequency of 9.7 GHz.

3.2.4 Theoretical quantum chemical calculations

All quantum chemical calculations were performed using density functional theory (DFT) using the B3LYP functional using LANL2Z basis set and LANL effective core potentials. The tetrahedral (T_d) sites occupied by Mn(II) for ZnS and CdS lattice were obtained from the respective crystal structures. The minimum-energy path (MEP) for dopant migration from an occupied T_d site to an adjacent vacant T_d site was calculated using the TERACHEM quantum chemistry package which was then used to calculate the energy barrier for the dopant migration.

3.3 Result and Discussion

In this work, Mn shell-doped core/multi-shell QDs were designed and the directional migration behaviors of Mn ions in the QD lattice were studied under the influence of an inserted CdZnS layer as an “atomic trap” within core/multi-shell QDs. The inward dopant migration was investigated by inserting alloyed interface (CdZnS) in Mn shell-doped CdS/Mn:CdS/ZnS (i.e., CdS/CdZnS/Mn:CdS/ZnS) and CdS/Mn:ZnS/ZnS (i.e., CdS/CdZnS/Mn:ZnS/ZnS) core/multi-shell QDs. To expand the atomic trapping strategy for directional dopant migration, we then explored the inward Mn migration behavior by inserting CdZnS alloyed shell in Mn shell-doped core/multi-shell QDs. The Mn(II) dopant behaviors when doped into both smaller substitutional Zn sites and larger substitutional Cd sites in the shell lattice were tested. (Scheme 3.1).

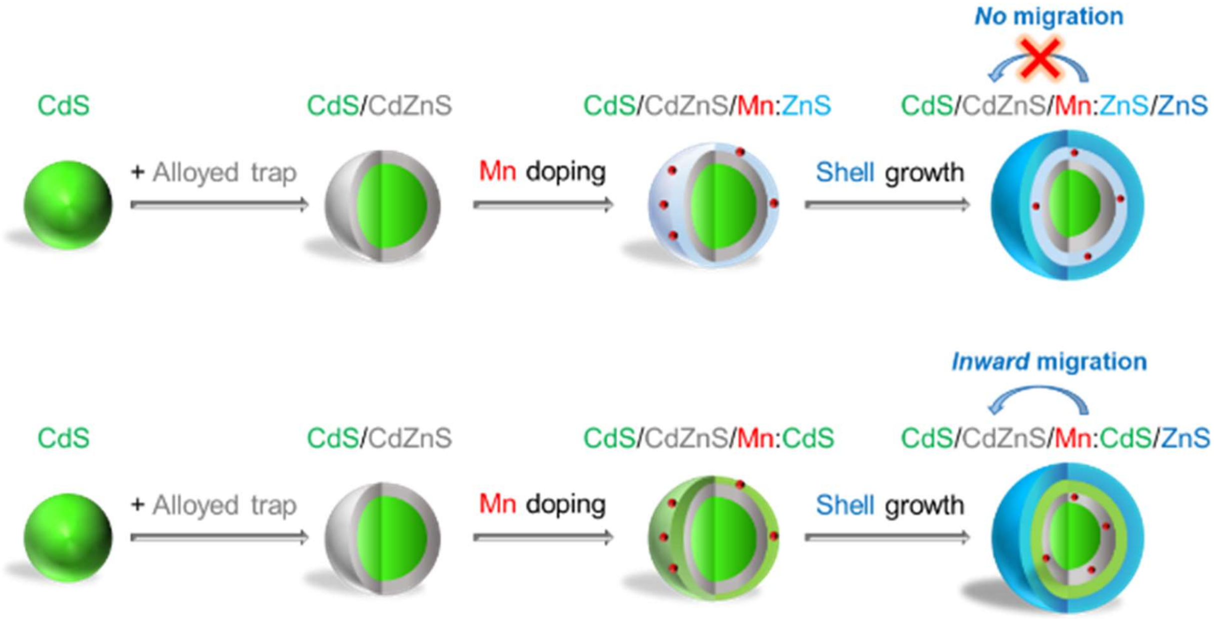

Scheme 3.1 Schematic of Mn shell-doped core/multi-shell QDs with inward dopant migration by inserting an alloyed "trap" for Mn dopants.

3.3.1 Mn doping into smaller substitutional Zn sites (74 pm) in ZnS shell

We first synthesized undoped CdS core QDs, followed by inserting a CdZnS alloyed shell before the dopant growth in the ZnS shell (*i.e.*, CdS/CdZnS$_{(1\ \mathrm{ML})}$/Mn:ZnS/ZnS$_{(1–3\ \mathrm{MLs})}$ core/multi-shell QDs) using a SILAR method. Successful shell growth was evidenced by the gradual size increase of QDs from 3.0 ± 0.3 nm of the CdS core QDs to 6.4 ± 0.3 nm after 1 ML CdZnS and 5 MLs ZnS shell coating from TEM images (Figure 3.1 a–c), as well as gradual XRD peak shift from cubic CdS to cubic ZnS phase with the increase of the ZnS shell thickness (Figure 3.1d, and Figure 3.2).

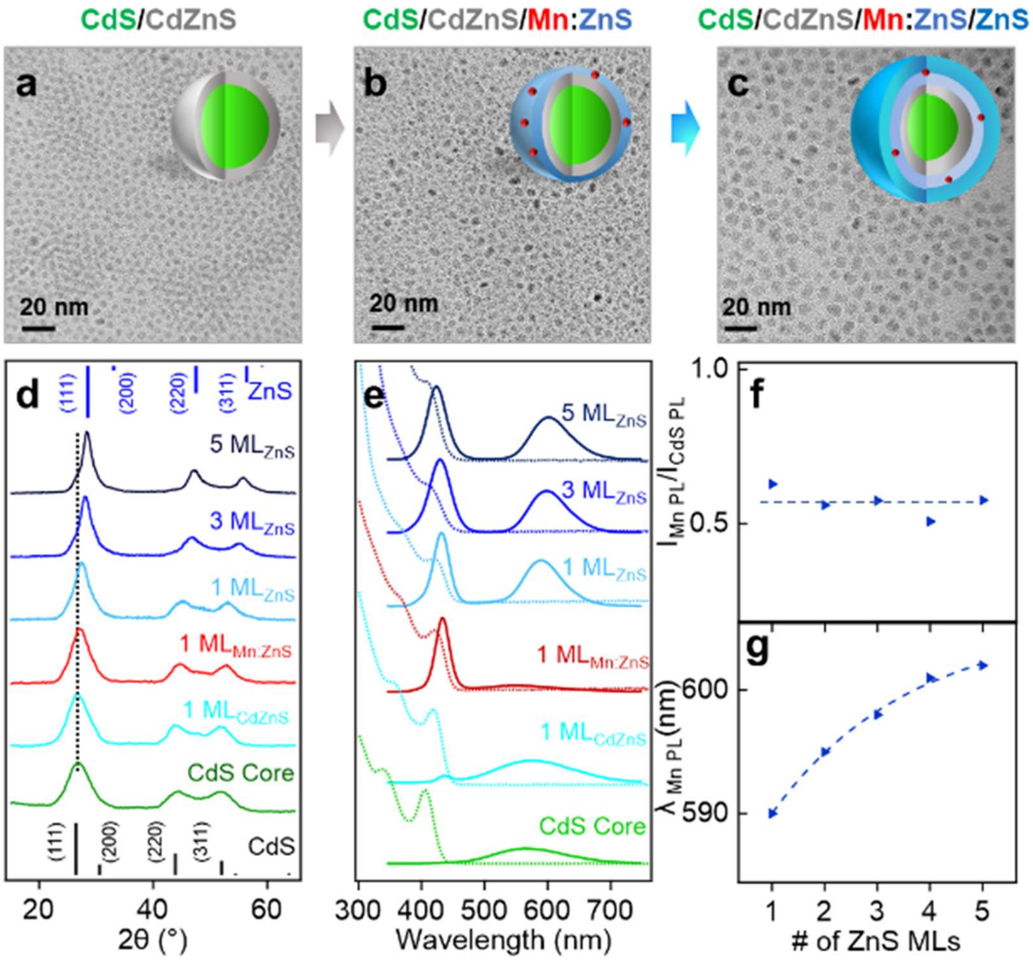

Figure 3.1 (a–c) TEM images of CdS/CdZnS, CdS/CdZnS/Mn:ZnS, and CdS/CdZnS/Mn:ZnS/ZnS core/multi-shell QDs. (d) XRD patterns and (e) normalized absorption (dotted lines) and PL (solid lines) spectra of CdS core and CdS/CdZnS/Mn:ZnS/ZnS$_{(1\text{–}5\ \text{MLs})}$ core/multi-shell QDs. (f) The PL Intensity ratio of Mn(II) and CdS host lattice ($I_{\text{Mn PL}}/I_{\text{CdS PL}}$) and (g) the Mn(II) PL peak position as a function of ZnS shell thickness.

Figure 3.1e shows the absorption and PL spectra of CdS/CdZnS/Mn:ZnS/ZnS core/multi-shell QDs. The CdS core QDs exhibit an absorption peak around 404 nm and a broad defect emission peak centered around 580 nm. A new bandgap emission peak from CdS QDs at around 420 nm was observed after the growth of the first CdZnS shell. 1 ML ZnS shell on the surface of CdS/CdZnS/Mn:ZnS QDs leads to a Mn PL around 587 nm. As the ZnS shell MLs increase, the

Mn PL peak redshifts indicating the shell thickness-dependent pressure applied on the Mn dopants (Figure 3.1e, g and Figure 3.3). Surprisingly, no significant change in the PL ratio of Mn and CdS ($I_{\mathrm{Mn}}/I_{\mathrm{CdS}}$) of the core/multi-shell QDs with different ZnS shell thickness occurred (Figure 3.1f), which indicates no significant dopant migration towards the inserted alloyed shell when Mn(II) dopants were directly doped into ZnS shell. Based on this result, we hypothesized that there might be a high energy barrier for dopant hopping when dopants occupy a smaller Zn(II) substitutional site (74 pm) for a Mn(II) dopant (80 pm). In contrast, a larger initial substitutional site could lead to a lower energy barrier for dopant hopping, which allows for efficient atomic trapping and dopant migration.

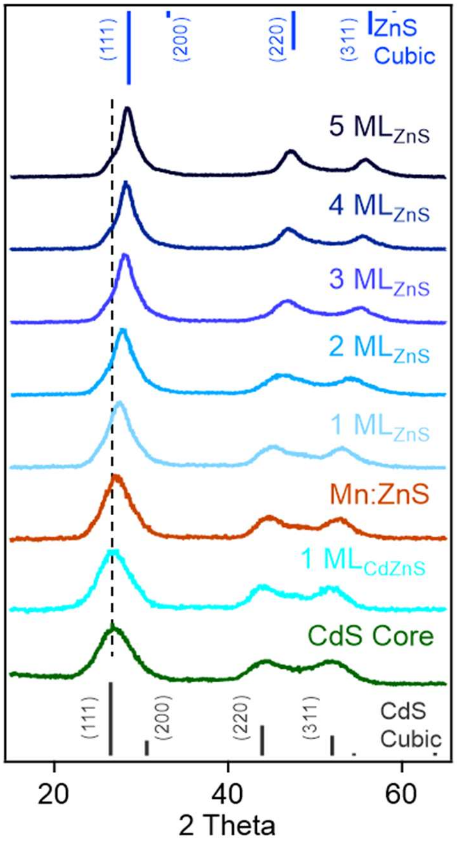

Figure 3.2 XRD patterns of CdS core and CdS/CdZnS/Mn:ZnS/ZnS$_{(1\text{-}5\ \mathrm{MLs})}$ core/multi-shell QDs.

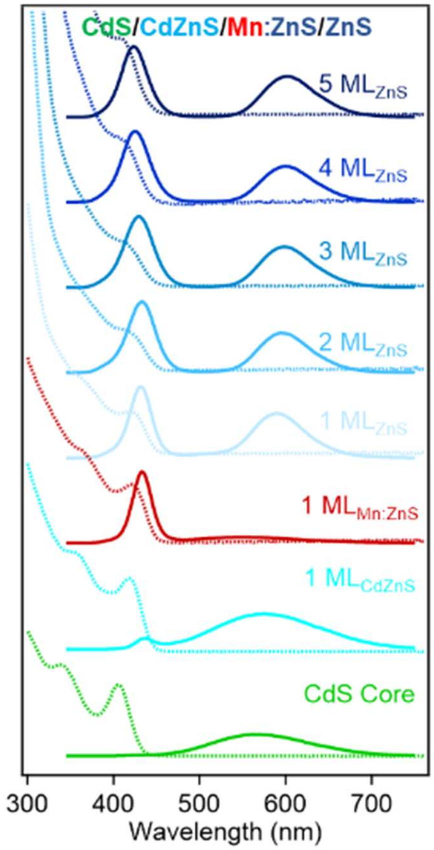

Figure 3.3 Normalized absorption (dotted lines) and PL (solid lines) spectra of CdS core and CdS/CdZnS/Mn:ZnS/ZnS$_{(1\text{-}5\ \text{MLs})}$ core/multi-shell QDs.

3.3.2 Mn doping into larger substitutional Cd sites (92 pm) in CdS shell

To study the initial substitutional site-dependent dopant behavior under the influence of the alloyed "trap" layer, Mn(II) ions were doped in CdS shell with larger substitutional Cd(II) cationic sites (92 nm) in CdS/CdZnS/Mn:CdS/ZnS core/multi-shell QDs. TEM images indicate the size of the core/multi-shell QDs increases ~0.5 nm upon the addition of each shell layer (Figure 3.4a–c), which is similar to that of CdS/CdZnS$_{(1\ \text{ML})}$/Mn:ZnS/ZnS core/multi-shell QDs (Figure 3.5). XRD diffraction peaks gradually shifted from cubic CdS to cubic ZnS phase as the function of the ZnS shell thickness (Figure 3.4d and Figure 3.6). ICP-OES measurements indicate that the Mn doping concentration is 0.4% for CdS/CdZnS/Mn:CdS QDs, which represents ~5 Mn(II) ions per QD with an average diameter of a 3.8 nm. After the 1st ML of ZnS coating onto the QDs, the Mn doping concentration dropped to 0.3% which represents ~4 Mn(II) ions per QD with an average diameter of 4.3 nm.

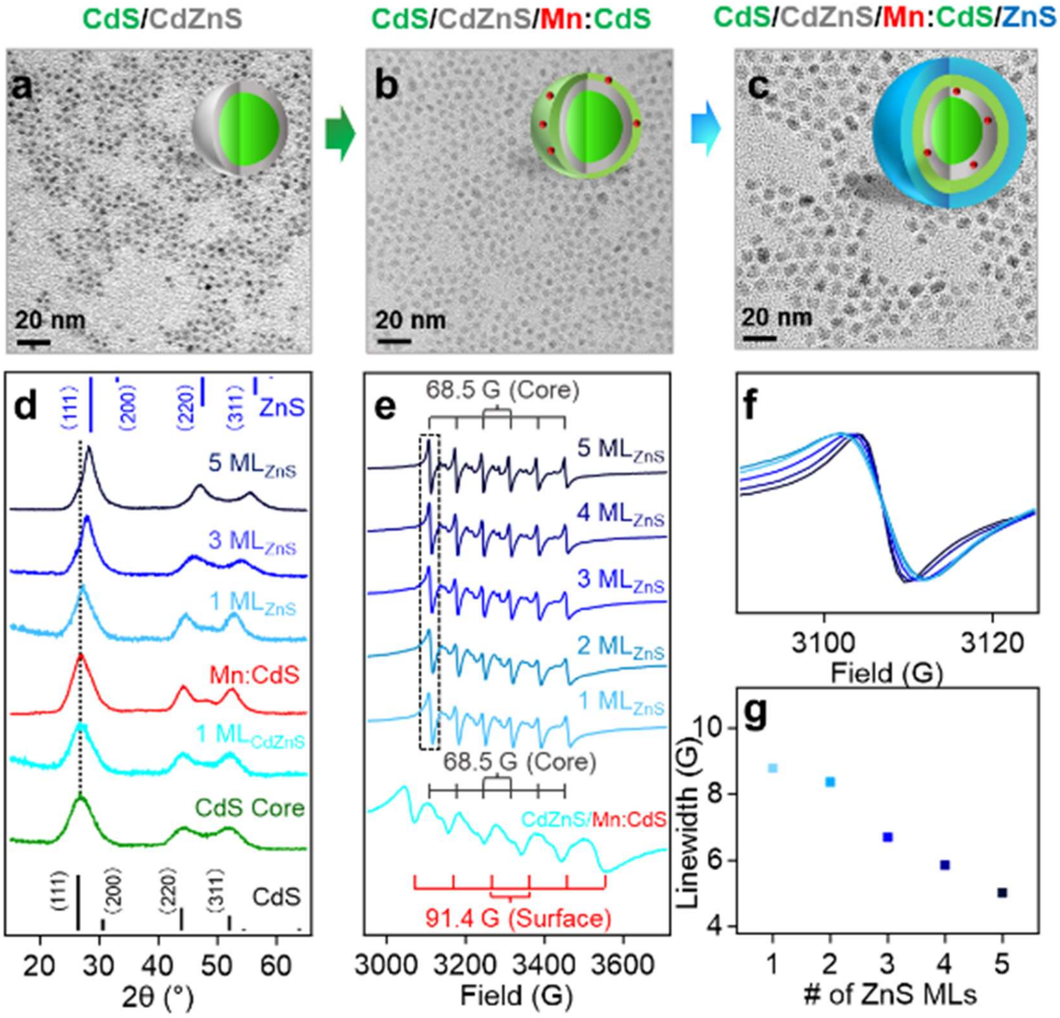

Figure 3.4 (a–c) TEM images of CdS/CdZnS, CdS/CdZnS/Mn:CdS, and CdS/CdZnS/Mn:CdS/ZnS core/multi-shell QDs. (d) XRD patterns of CdS and CdS/CdZnS/Mn:CdS/ZnS core/multi-shell QDs. (e) X-band EPR spectra of CdS/CdZnS/Mn:CdS and CdS/CdZnS/Mn:CdS/ZnS$_{(1–5\ \mathrm{MLs})}$ core/multi-shell QDs. (f) The representative first sextet hyperfine peak of EPR spectra to display general decreasing spectral linewidth and (g) the EPR hyperfine peak linewidth as a function of shell monolayers.

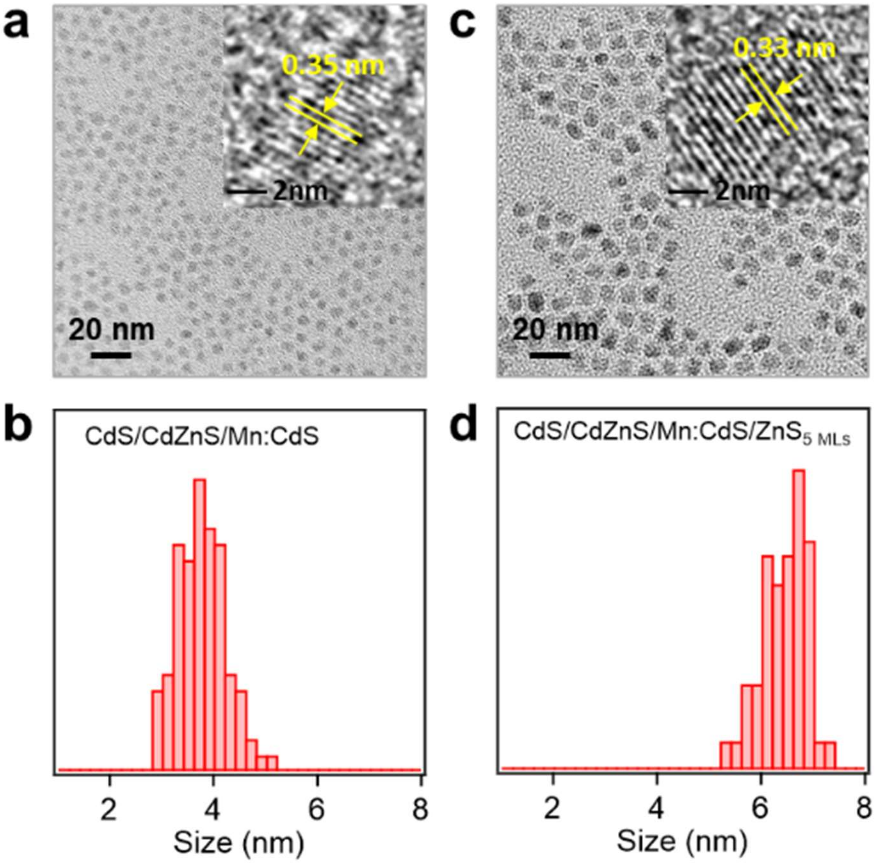

Figure 3.5 TEM Images and histogram of CdS/CdZnS/Mn:CdS and CdS/CdZnS/Mn:CdS/$ZnS_{5\ MLs}$ core/multi-shell QDs. The insets are the high-resolution TEM images showing d-spacing of the (111) lattice plane of the QDs. The slight decrease in the average interplanar spacing from 0.35 nm of CdS/CdZnS/Mn:CdS to 0.33 nm of CdS/CdZnS/Mn:CdS/$ZnS_{5\ MLs}$ core/multi-shell QDs is consistent with the smaller lattice parameters of ZnS compared with that of CdS. The size of the QDs increased from 3.8 ± 0.3 nm (a and b) to 6.4 ± 0.3 nm (c and d) for 5 MLs of ZnS shell coated on the QDs.

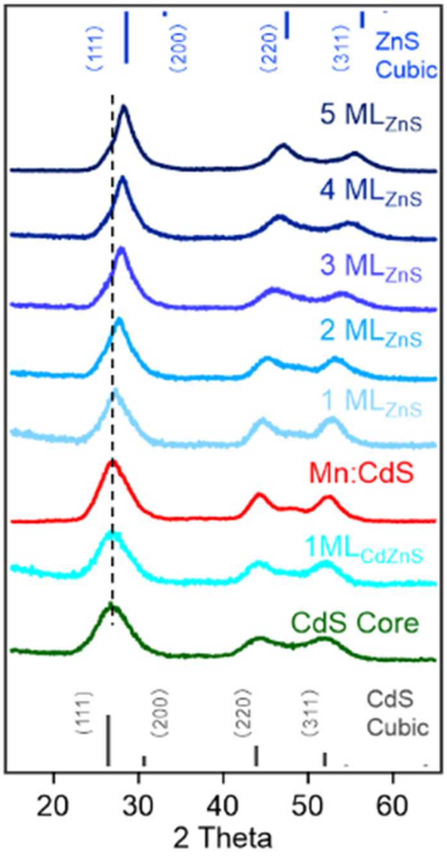

Figure 3.6 XRD patterns of CdS/CdZnS/Mn:CdS/ZnS core/multi-shell QDs as a function of shell thickness.

EPR data illustrates the hyperfine peaks with hyperfine splitting constants of 91.4 G and 68.5 G from surface and core Mn dopants for the CdS/CdZnS/Mn:CdS QDs, respectively (Figure 3.4e). For the CdS/CdZnS/Mn:CdS/ZnS QDs core/multi-shell QDs, all surface hyperfine terms were removed through ZnS shell coating. Interestingly, the linewidth of the core Mn hyperfine splitting peaks of the CdS/CdZnS/Mn:CdS/ZnS$_{(1–5\ MLs)}$ QDs decreased from 8.6 G (1st ZnS ML) to 5.0 G (5th ZnS MLs) (Figure 3.4f and g). Considering a slightly larger average Mn–Mn distance after the inward dopant migration in the core/multi-shell QDs (from ~1.7 nm to ~2.1 nm. See Table 3.1 and calculation, and Scheme 3.2), the decreasing hyperfine peak linewidth could indicate more diluted Mn doping inside the inserted alloy trap layer, as well as narrower and more homogeneous Mn bonding environments, as the result of dopant migration towards the alloy trap layer with the smaller cationic size mismatch with Mn dopants.

Table 3.1 The average distance between Mn ions inside CdS/CdZnS/Mn:CdS QDs and CdS/CdZnS/Mn:CdS/ZnS QDs with inward dopant migration behavior.

Sample	[Mn]	Number of Mn ions per QD (n)	Assuming dopant radial position from the center of a QD/nm	Average surface area occupied per Mn ion (A_{Mn}) /nm^2	Average distance between Mn ions (d_{Mn}) /nm
CdS/CdZnS/Mn:CdS	0.4%	5	At the CdZnS and Mn:CdS shell interface (1.75 nm)	7.70	1.57
			At the midpoint of Mn:CdS shell (1.88 nm)	8.84	1.68
			At the outer surface of Mn:CdS shell layer (2 nm)	10.04	1.79
CdS/CdZnS/Mn:CdS/ZnS_{1ML}	0.3%	4	At the CdZnS and Mn:CdS shell interface (2 nm)	12.57	2.00
			At the midpoint of Mn:CdS shell (2.13 nm)	14.19	2.13
			At the to outer surface of Mn:CdS shell layer (2.25 nm)	15.90	2.25

Note: ***Calculation of the average distance between Mn ions within QDs before and after dopant migration.***

For the Mn shell-doped core/multi-shell QDs, Mn ions would occupy in a thin shell layer above the CdS core. The surface area of a shell QD can be calculated using equation 3.2,

$$A_{shell} = 4\pi r_{QD}^2 \quad \text{(Eq. 3.2)}$$

The average area occupied by each Mn ion can be calculated using equation 3.3. It should be noted that decreased doping concentration after shell coating and the number of Mn ions per core/shell QD is represented as n'.

$$A_{\mathrm{Mn}} = A_{\mathrm{shell}}/n' \quad \text{(Eq. 3.3)}$$

The radius of the circle occupied by a Mn ion (R_{Mn}) is,

$$R_{\mathrm{Mn}} = \sqrt{\frac{A_{\mathrm{Mn}}}{4\pi}} \quad \text{(Eq. 3.4)}$$

Then the average Mn-Mn distance in the shell can be estimated as 2 * R_{Mn}.

ZnS shell coated CdS/CdZnS/Mn:CdS QDs, *i.e.,* CdS/CdZnS/Mn:CdS/ZnS$_{(1\text{-}5\ \mathrm{MLs})}$, have the same dopant concentration, and therefore the same average distance between Mn ions, regardless of the ZnS shell MLs.

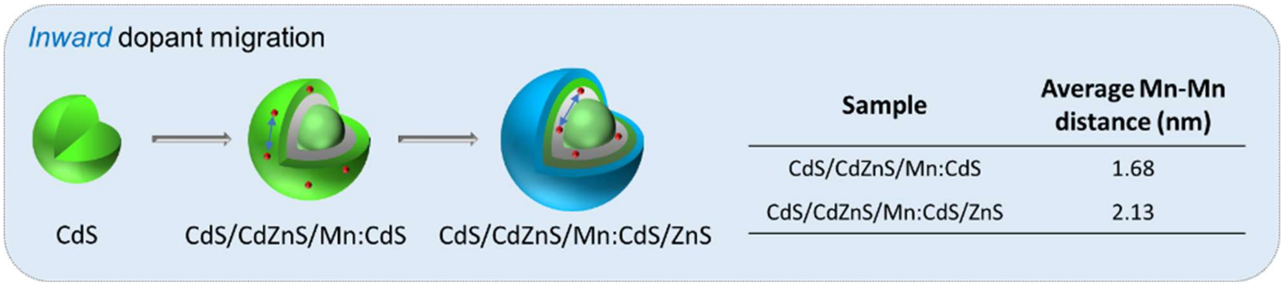

Sample	Average Mn-Mn distance (nm)
CdS/CdZnS/Mn:CdS	1.68
CdS/CdZnS/Mn:CdS/ZnS	2.13

Scheme 3.2 Average Mn-Mn distance before and after inward dopant migration inside shell-doped QDs.

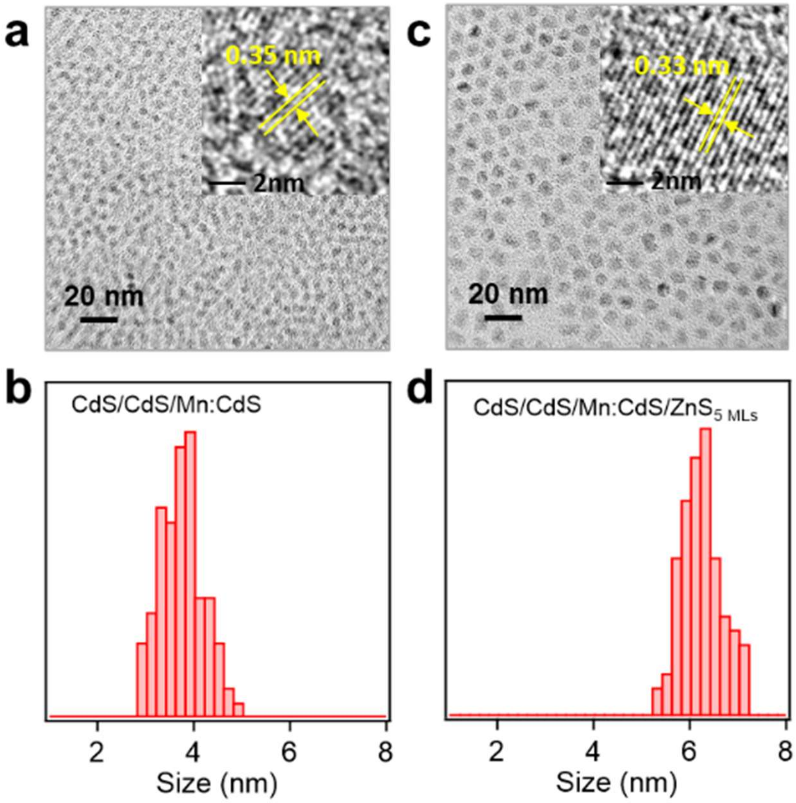

Figure 3.7 TEM Images and histogram of CdS/CdS/Mn:CdS and CdS/CdS/Mn:CdS/$ZnS_{5\ \mathrm{MLs}}$ core/multi-shell QDs. The insets are the high-resolution TEM images showing d-spacing of the (111) lattice plane of the QDs. The slight decrease in the average interplanar spacing from 0.35 nm of CdS/CdS/Mn:CdS to 0.33 nm of CdS/CdS/Mn:CdS/$ZnS_{5\ \mathrm{MLs}}$ core/multi-shell QDs is consistent with the smaller lattice parameters of ZnS compared with that of CdS. The size of QDs increased from 3.8 ± 0.3 nm (a and b) to 6.4 ± 0.3 nm (c and d) for 5 MLs of ZnS shell coated on the QDs.

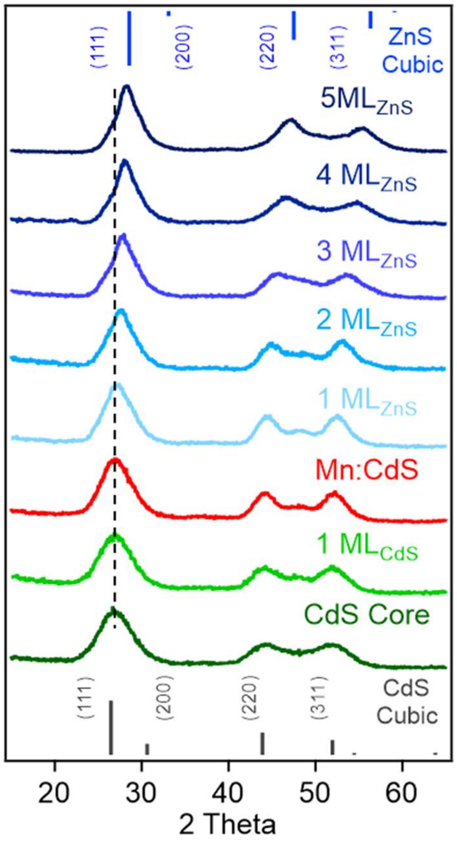

Figure 3.8 XRD patterns of CdS/CdS/Mn:CdS/ZnS core/multi-shell QDs as a function of shell thickness.

To further prove the role of the alloyed trap layer for dopant migration, we used a CdS layer to replace CdZnS in the core/multi-shell QDs (*i.e.*, CdS/CdS/Mn:CdS/ZnS) without an "atomic trap" in the core/shell interface (Figure 3.7 and 3.8). Two similar sets of EPR hyperfine splitting from surface and core Mn dopants (A: 96.0 and 69.1 G) from CdS/CdS/Mn:CdS QDs and only core hyperfine peaks were observed after the following ZnS shell coating in CdS/CdS/Mn:CdS/ZnS QDs (Figure 3.9). However, no change in the linewidth of the Mn core hyperfine peaks (7.5 G for QDs from the 1st to 5th ZnS shell) was observed (Figure 3.9b and c), which indicates no significant changes in the dopant bonding environment and location inside the QD lattice without the CdZnS alloyed trap layer.

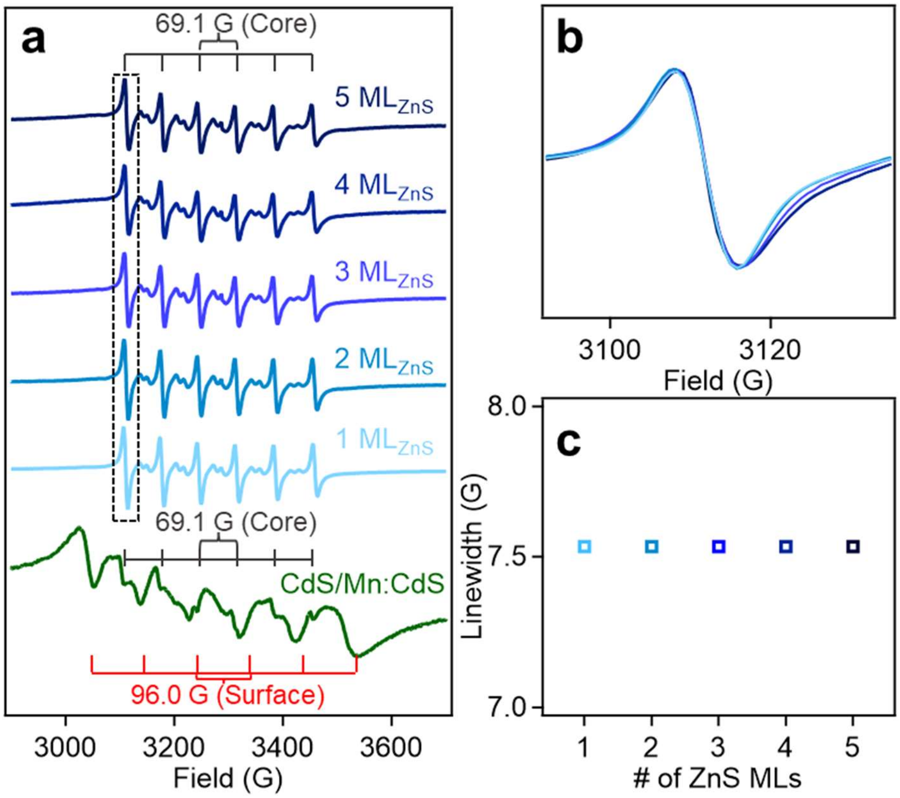

Figure 3.9 (a) Room Temperature X-Band EPR spectra of CdS/CdS/Mn:CdS/ZnS$_{(1\text{-}5\ \mathrm{MLs})}$ core/multi-shell QDs. Two discrete substitutional Mn(II) sites including the core Mn(II) sites (hyperfine splitting constant (A: 69.1 G) and surface Mn(II) sites (A: 96.0 G). During the shell passivation, only the core site (A = 69.1 G) was observed. (b) The representative first sextet hyperfine peak of EPR spectra to display spectra linewidth and (c) the EPR hyperfine peak linewidth as a function of shell monolayers.

The absorption and PL spectra of the selected CdS/CdZnS/Mn:CdS/ZnS and CdS/CdS/Mn:CdS/ZnS core/multi-shell QDs are shown in Figure 3.10a and b, respectively (full set optical data in Figure 3.11). The PL QYs of the QDs gradually increased during the ZnS shell passivation, which is similar to undoped core/multi-shell QDs with the same core and shell lattice (Figure 3.12). Significantly, the PL intensity ratio of Mn(II) and CdS host lattice ($I_{\mathrm{Mn}}/I_{\mathrm{CdS}}$) increases from 1.22 to 2.50 during the ZnS shell growth (1–5 MLs) in the

CdS/CdZnS/Mn:CdS/ZnS core/multi-shell QDs (Figure 3.10c), which is in contrast to the lack of a change in $I_{\mathrm{Mn}}/I_{\mathrm{CdS}}$ when doping Mn in the ZnS lattice of CdS/CdZnS/Mn:ZnS/ZnS core/multi-shell QDs. (Discussed in Mn doping into ZnS shell with smaller initial substitutional Zn sites above.)

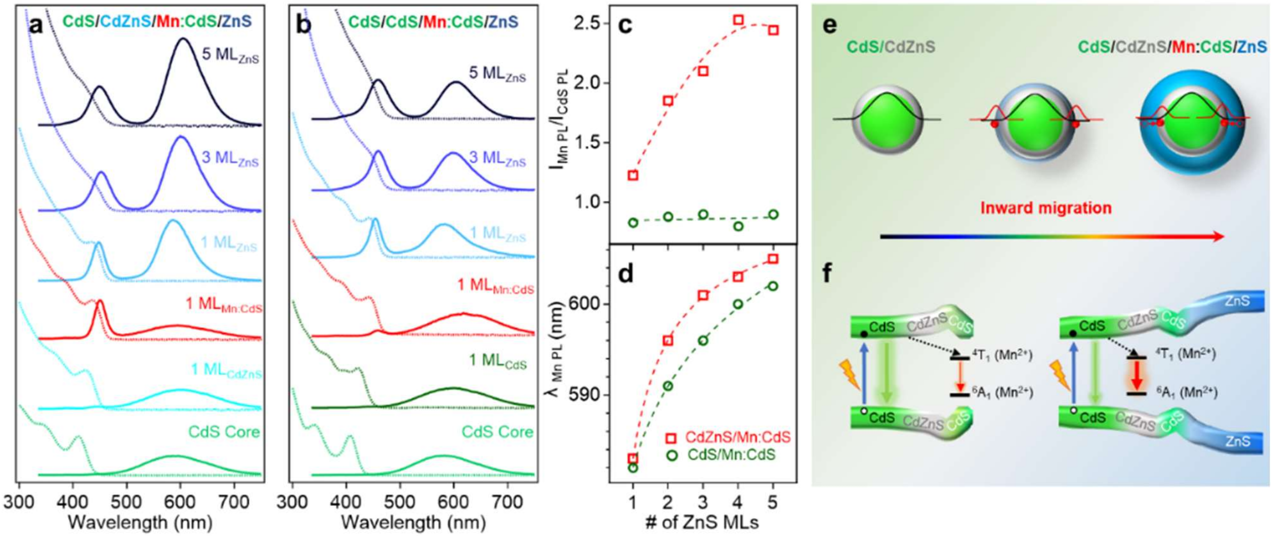

Figure 3.10 (a and b) Normalized absorption and PL spectra of (a) CdS/CdZnS/Mn:CdS/$\mathrm{ZnS}_{(1\text{–}5\ \mathrm{MLs})}$ and (b) CdS/CdS/Mn:CdS/$\mathrm{ZnS}_{(1\text{–}5\ \mathrm{MLs})}$ core/multi-shell QDs. (c) The PL Intensity ratio of Mn(II) and CdS host lattice and (d) the changes of Mn(II) PL peak position as a function of ZnS shell thickness. (e) Schematic of the dopant inward migration by inserted CdZnS alloyed trap layer and (f) the band alignment of the CdS/CdZnS/Mn:CdS/ZnS core/multi-shell QDs.

Based on eq. 2.1, the increased PL ratio between Mn(II) and CdS host lattice represents increased rate of energy transfer (k_{ET}), which indicates the enhanced host-to-dopant energy transfer due to the inward Mn migration to the alloyed interface (Figure 3.10e and f). Furthermore, there was no significant change in the PL ratio of Mn(II) and CdS host QDs when a CdS layer is used to replace the “atomic trap” CdZnS layer in the CdS/CdS/Mn:CdS/ZnS core/multi-shell QDs (Figure 3.10b and c), which indicates there was no significant dopant migration in the absence of the alloyed interface even though Mn dopants substitute in larger Cd sites. In addition, a rapid redshift of the Mn PL position (23 nm) was observed in the CdS/CdZnS/Mn:CdS/ZnS QDs with the inserted alloy trap (Figure 3.10a and d). In contrast, the Mn dopant PL peak position of CdS/CdS/Mn:CdS/ZnS QDs experienced a lesser redshift (20 nm, Figure 3.10b and d). The larger Mn PL peak shift indicates larger pressure applied from the thick outer shell in CdS/CdZnS/Mn:CdS/ZnS QDs, which can support that the alloy trap layer could facilitate the inward dopant migration (Figure 3.10e).

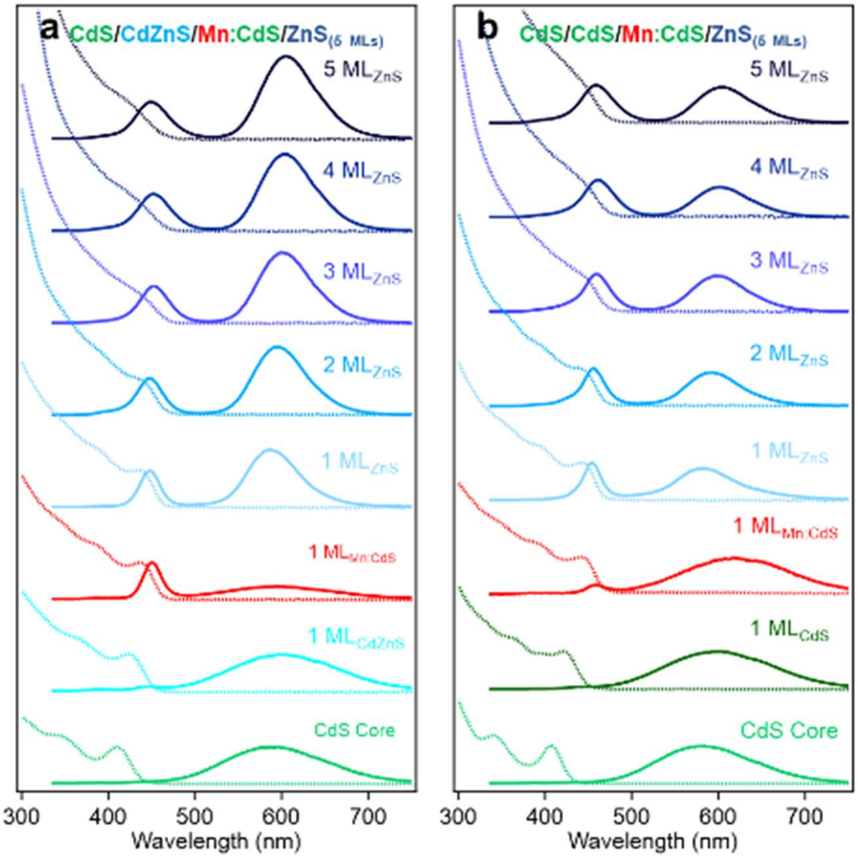

Figure 3.11 Normalized absorption (dotted lines) and PL (solid lines) spectra of (a) CdS/CdZnS/Mn:CdS/ZnS$_{(1\text{-}5\ MLs)}$ and (b) CdS/CdS/Mn:CdS/ZnS$_{(1\text{-}5\ MLs)}$ core/multi-shell QDs.

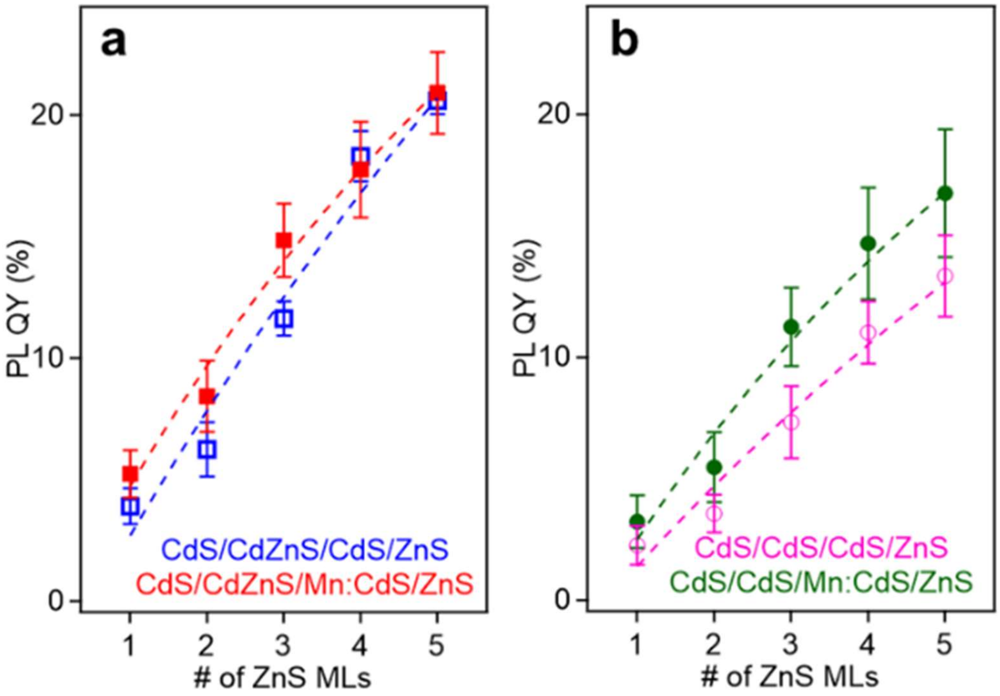

Figure 3.12 PL QYs (a) shell doped CdS/CdZnS/Mn:CdS/ZnS$_{(1\text{-}5\ \text{MLs})}$ and undoped CdS/CdZnS/CdS/ZnS$_{(1\text{-}5\ \text{MLs})}$ core/multi-shell QDs, and (b) shell doped CdS/CdS/Mn:CdS/ZnS$_{(1\text{-}5\ \text{MLs})}$ and undoped CdS/CdS/CdS/ZnS$_{(1\text{-}5\ \text{MLs})}$ core/multi-shell QDs.

3.3.3 Mechanism of initial dopant site-dependent dopant migration behavior and DFT calculations

Our experimental results indicate significant dopant migration when Mn(II) ions were doped at larger Cd(II) substitutional cationic sites (92 pm) in Mn:CdS/CdZnS/ZnS (outward migration) and CdS/CdZnS/Mn:CdS/ZnS core/multi-shell QDs (inward migration) under the influence of inserted CdZnS "atomic trap". The large size mismatch (13%) between a Mn(II) dopant and a larger Cd(II) substitutional site (Mn_{Cd}^{X}) entails significant local distortion of the structure, therefore, thermodynamically, the dopant migration to the alloyed shell with smaller size mismatch ($Mn_{Cd/Zn}^{X}$) to reduce the cationic size strain between Mn(II) ions and host sites is favored. However, no significant dopant migration towards inserted alloyed shell occurred when

Mn(II) dopants were directly doped into ZnS shell with smaller Zn(II) cationic sites (74 pm) as in CdS/CdZnS/Mn:ZnS/ZnS core/multi-shell QDs. Therefore, the initial doping environment can affect the dopant behavior, which can be understood as the different energy barriers for the Mn dopants hopping between the T_d sites formed in the cubic close packing of S ions. In general, the dopant ions will follow the lowest energy path available in the host lattice during migration, in which the dopant ion first passes through one of the triangular faces of the T_d site, then through one of the triangular faces of an adjacent tetrahedron, before arriving at the vacant tetrahedral site ($V''_{Cd/Zn}$, Figure 3.13a and b).

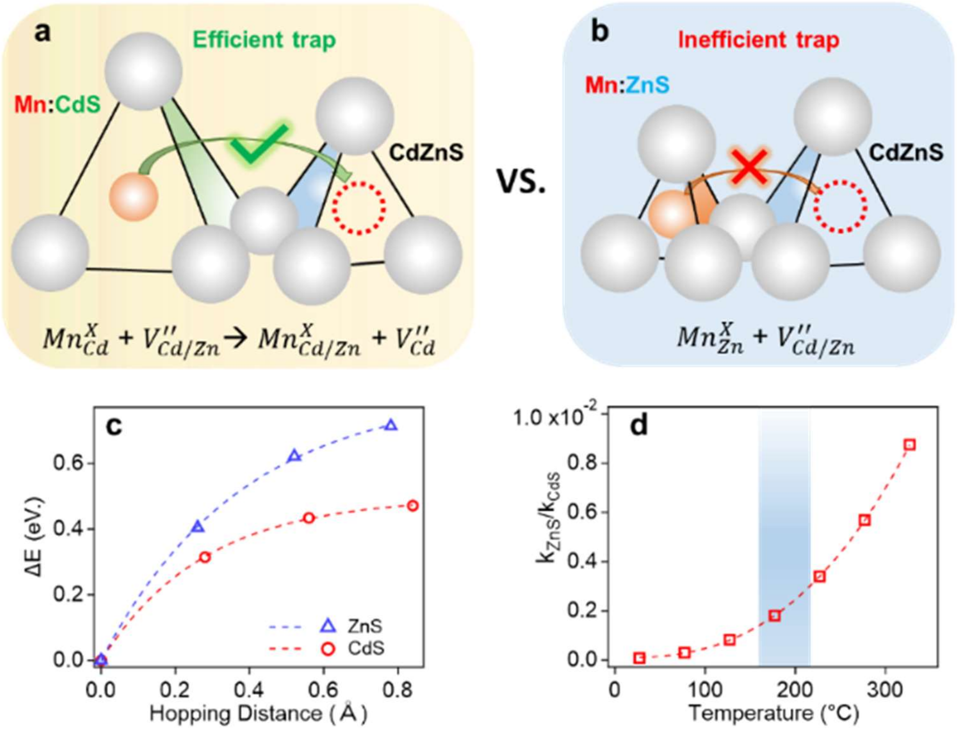

Figure 3.13 Schematic of dopant migration behaviors when a Mn dopant occupies a larger substitutional Cd site in QD lattice (a) and a smaller substitutional Zn site in QD lattice (b). (c) DFT calculation of the minimum energy path as a function of the reaction coordinate (*Z*) at 0 K. (d) Ratio of rate constant for dopant migration in ZnS and CdS lattices as a function of temperature.

In the case of Mn doped at a smaller Zn(II) substitutional site (74 pm, Mn_{Zn}^{X}), a high activation energy for dopant hopping is expected since the dopant needs to move through a small triangular face from the host ZnS_4 tetrahedron (Figure 3.13b). The high activation energy for dopants escaping from the small tetrahedrons leads to inactive dopant trapping of the alloyed T_d site. Therefore, no notable dopant migration occurs in our experiments even though with the inserted “alloyed trap” layer. In contrast, a larger initial substitutional Cd(II) site (92 pm) in CdS lattice with larger triangular faces of the host CdS_4 tetrahedron could lead to a lower energy barrier for dopant hopping (Figure 3.13a), which allows for active/efficient atomic trapping and directional dopant migration towards alloyed lattice under moderate temperatures ($Mn_{Cd}^{X} + V_{Cd/Zn}'' \rightarrow Mn_{Cd/Zn}^{X} + V_{Cd}''$).

To further confirm the initial doping site-dependent dopant behaviors, the minimum energy path (MEP) of the Mn dopant hopping to escape from the T_d site in ZnS and CdS lattice was calculated using DFT. The transition-state structure for the Mn migration was obtained by constraining the Mn to be co-planar with one of the triangular faces of the T_d site (Figure 3.13a and b). The direction normal to the plane, defined by the three S and the Mn atoms, was identified to the unbound reaction coordinate which was used to construct the MEP for Mn migration (Figure 3.13c). The zero of the hopping distance (x-axis in Figure 3.13c) corresponds to the minimum-energy structure of the Mn in the T_d site. The barrier height (E^a) is defined as the energy difference between the transition-state and the minimum-energy structure for both CdS and ZnS T_d sites. The results from the MEP analysis show that the E^a is 0.71 and 0.47 eV at 0 K for ZnS_4 and CdS_4 T_d sites, respectively, which represents a 52% higher energy barrier for the Mn hopping in the ZnS lattice as compared to the CdS lattice.

The barrier height (E^a) was further used to calculate the temperature-dependence relative rate constant of dopant migration using transition-state theory[231] (Figure 3.13d). The relative temperature dependence of the mobility of the ions can be expressed by an Arrhenius-like equation.

$$\frac{k_{ZnS}}{k_{CdS}} = \frac{\exp\left[-E^a_{ZnS}/k_B T\right]}{\exp\left[-E^a_{CdS}/k_B T\right]} \qquad \text{(eq. 3.5)}$$

Analysis of the relative rate constants show that the rate of Mn dopant migration is about three-orders of magnitude smaller (0.0018–0.004) in the ZnS lattice as compared to CdS for the temperature range investigated in this study (180–230 °C, blue region in Figure 3.13d). It should be noted that higher thermal energy of dopant ions at elevated temperatures (>230 °C) could lead to fast dopant migration due to the increased hopping frequencies of the dopants inside the host lattice.[15] However, the rate of Mn dopant migration in the ZnS lattice as compared to CdS is still more than two-orders of magnitude smaller (0.005–0.01) at 230–320 °C shown in Figure 3.13d, which can support the different dopant behaviors when dopants initially substitute in Cd and Zn sites in the core/multi-shell QDs.

3.4 Conclusion

In this work, directional inward dopant migration behaviors was achieved using an alloyed layer with a small cationic size mismatch with the dopant ions in Mn shell-doped core/multi-shell QDs. The inserted alloyed shell (CdZnS) with smaller cationic size mismatch with the dopants can serve as an "atomic trap" to the dopant ions to reduce the strain from the larger cationic mismatch between Mn(II) ions and host sites. In addition, the initial dopant substantial site is critical for the dopant migration behavior. Specifically, larger Cd(II) substitutional sites for Mn dopants in the core (shell)-doped core/multi-shell QDs with inserted

CdZnS “active atomic trap” facilitate either the *outward* or *inward* dopant migration, while smaller initial substitutional sites inhibit dopant movement due to higher energy barrier for dopant hopping even through more stable alloyed substitutional sites are available (*i.e.*, “inefficient atomic trap”). This work represents the first directional dopant migration behavior in NC lattice by inserting an “atomic trap” for dopant ions. Controlled dopant migration inside NC lattice provides a new way to fine tune the properties of doped QDs.

Chapter 4

Dopant Behaviors in Perovskite/CdS Ionic Core/Covalent Shell or CdS/Perovskite Covalent Core/Ionic Shell Heterojunctions

Perovskites, a class of materials with a general formula of ABX_3, have attracted considerable attention for their versatile applications in photovoltaics and LEDs. Recent advancements have particularly highlighted the importance of metal halide perovskite QDs (PQDs) and transition metal doped PQDs due to their outstanding optoelectronic properties and potential to enhance solar cell efficiency. Researchers have designed and synthesized epitaxial core/shell structures and heterostructures to improve their stability and functionality. However, dopant behaviors, such as dopant diffusion, distribution, and migration, within core/shell PQDs remain unclear. This chapter explores the synthesis of perovskite-based core/shell heterostructures combined with II-VI chalcogenide semiconductors using various colloidal methods and investigates dopant behavior through the examination of optical properties. In addition, it was found that the significant differences in crystal structure, coordination, and growth mechanism between perovskites and chalcogenides make the synthesis of epitaxial core/shell PQDs very challenging.

4.1 Introduction

The term 'perovskite' originally referred to the mineral calcium titanium oxide ($CaTiO_3$), named after Russian mineralogist Lev Perovski who discovered it in 1839.[232] In the 1950s, the $CaTiO_3$ crystal structure was elucidated as a 3D network of BX_6 octahedra surrounded by a cubic A cage.[233] Since then, as a promising nanomaterial class, perovskites refer to a large category of materials that share an ABX_3 crystal structure, where A and B are cations and X is the anion (Figure 4.1). The A-site is traditionally occupied by large monovalent cations like methylammonium and cesium. The B-site often contains divalent metal cations like lead and tin. The X-site typically contains halide anions including chlorine, bromine, or iodine.

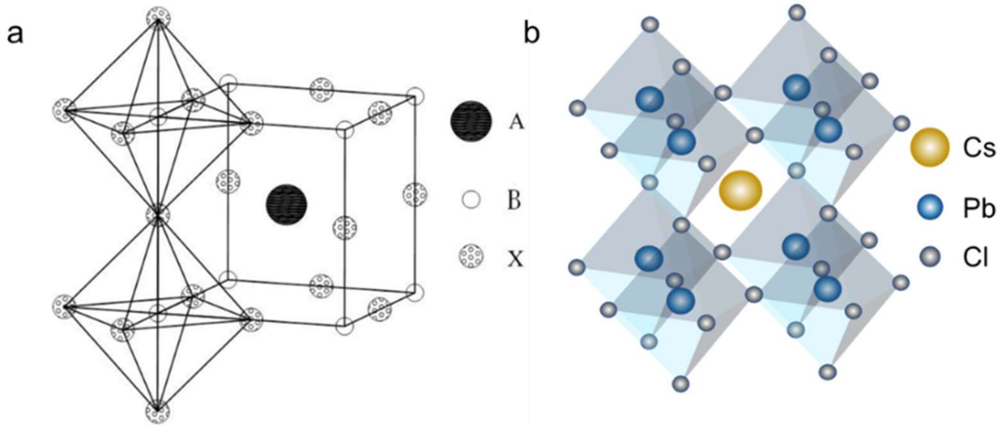

Figure 4.1 schematic of (a) ABX_3 structure[18] and (b) 3-D illustration of corner-sharing $PbCl_6$ in cubic $CsPbCl_3$ lattice.[19]

[18] [Reproduced with permission of the International Union of Crystallography © 2008]

[19] [Reproduced with open access from {Li, S.; Lin, H.; Chu, C.; Martin, C.; MacSwain, W.; Meulenberg, R. W.; Franck, J. M.; Chakraborty, A.; Zheng, W., Interfacial B-Site Ion Diffusion in All-Inorganic Core/Shell Perovskite Nanocrystals. ACS Nano 2023, 17 (22), 22467-22477.} Copyright © 2023 The Authors.]

The A, B, and X sites in the perovskite ABX_3 structure allow for diverse compositional engineering, leading to perovskites with different crystal structures and properties. The stability and structure of a perovskite can be predicted using the Goldschmidt tolerance factor t which could be calculated based on the ratio of the ionic radii of ions where r_A, r_B, and r_X are the ionic radii of the A-site, B-site and X ions (Eq. 4.1).[234, 235]

$$t = \frac{r_A + r_X}{\sqrt{2}\,(r_B + r_X)} \qquad \text{(eq. 4.1)}$$

While theoretically any combination of monovalent, divalent, and halide ions could occupy the A, B, and X sites, only certain combinations satisfy the tolerance factor requirements for a stable perovskite structure at room temperature. The tolerance factor must be between 0.8-1.0 to form a stable orthorhombic, tetragonal, or cubic perovskite crystal structure, which determines the size compatibility between the A, B, and X ions. Values closer to 1 give ideal cubic structures, while lower values give increasingly distorted tetragonal and orthorhombic phases. Thus, the Goldschmidt tolerance factor severely limits the possible ion combinations that can be used to synthesize viable perovskites (Figure 4.2).

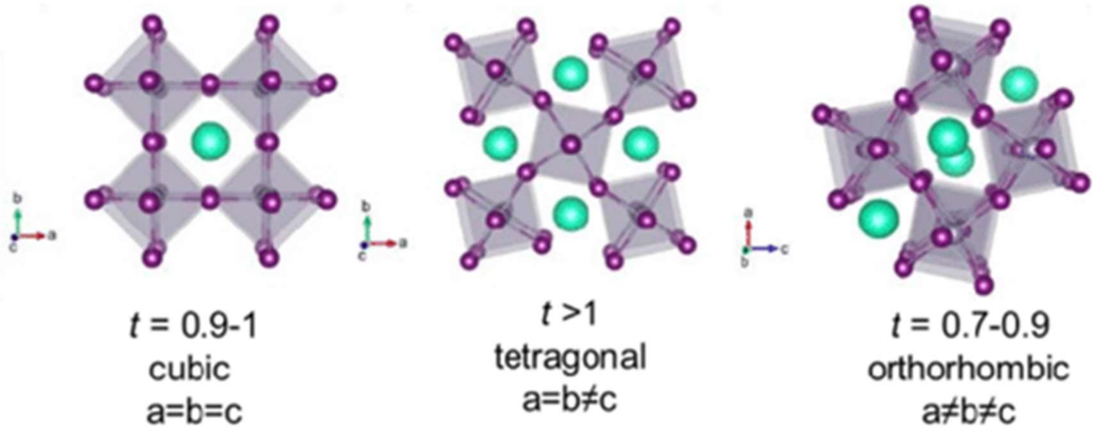

t = 0.9-1
cubic
a=b=c

t >1
tetragonal
a=b≠c

t = 0.7-0.9
orthorhombic
a≠b≠c

Figure 4.2 The illustration of different possible crystal structures based on different Goldschmidt tolerance factors (The illustration is based on the $CsSnI_3$ composition presented by E. Lora Da Silvia and coworkers.)[20, 21]

[20] [Reproduced with permission of the American Physical Society © 2015]

Metal halide perovskite QDs (PQDs) have rapidly attracted attention with a wide range of applications as a new emerged class of semiconductor.[236, 237] It was found that the PQDs usually have high defect tolerance, free of mid-gap trap states. PQDs have exhibited high photoluminescence quantum yield (PL QY),[84, 238-240] bright exciton triplet states,[241] superfluorescence,[242] and enhanced phase stability compared to the bulk,[243-245] as well as promising performance in photovoltaics,[246-248] light-emitting diodes (LEDs),[249-251] lasers[252-254] and photodetectors.[255-257] For example, during the year 2012, a research work designed a meso-superstructure perovskite-based solar cell in which perovskites act as both the light-harvesting material and the electron-transporting material, improving the power conversion efficiency to 10.9%.[258] The Ghosh group reported a high power conversion efficiency of 31% with an optimized perovskite solar cell structure, where a lead-free perovskite acts as a hole transport material.[259] The significant improvement in the power conversion efficiency of perovskite-based solar cells has ignited more in-depth studies of perovskite-based nanomaterials, such as doped perovskites or perovskites core/shell heterostructures.

Transition metal doping, particularly the incorporation of Mn ions in metal chalcogenide NC hosts, has been well-developed.[173, 260-263] The distinctive feature of Mn doping lies in its long-lifetime spin-forbidden d–d transition within a yellow–orange emission. In perovskite hosts, $CsPbCl_3$ stands out due to its wide band alignment and efficient host exciton energy transfer to Mn states.[264] Achieving successful Mn insertions in perovskite hosts requires a competitive reactivity of the Mn precursor with Pb, especially given the rapid reaction kinetics at the desired temperature (180–200°C).[264] One such method to provide the preferred reaction kinetics is to utilize RNH_3Cl as the activating reagent under high temperatures to overcome the challenges associated with doping in perovskite NCs.[22] Mn^{2+} ions substitutionally replace Pb^{2+} ions in the $CsPbCl_3$ NCs lattice to form doped perovskites as shown in figure 4.3.

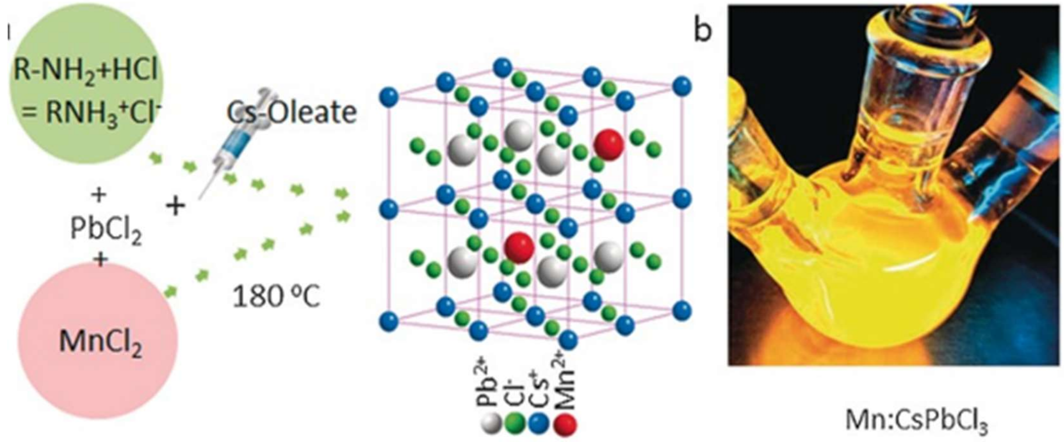

Figure 4.3 Schematic illustration of high-temperature synthesis of Mn doped $CsPbCl_3$ NCs using RNH_3Cl as the activating reagent.[22]

[22][Reprinted (adapted) with permission from {Das Adhikari, S.; Dutta, S. K.; Dutta, A.; Guria, A. K.; Pradhan, N., Chemically Tailoring the Dopant Emission in Manganese-Doped $CsPbCl_3$ Perovskite Nanocrystals. Angew Chem. Int. Ed. Engl. 2017, 56 (30), 8746-8750.}. Copyright (2017) John Wiley and Sons Publishing]

Using a solution phase approach under high temperatures, the synthesis of high quality perovskite NCs with different morphologies have been recently reported.[239, 265-267] For instance, using a high temperature synthesis approach, (150 - 250 °C), the reported $CsPbX_3$ nanocubes have a tunable emission range from 410 nm to 700 nm with a narrow emission line widths (12-42 nm) and high PL QYs (reaching up to 90%) by adjusting the composition of halide ions.[239, 268] Besides the size and composition, geometric morphology such as 0D spherical QDs, 1D nanowires, 2D nanoplatelets is another key factor to affect the overall optical and electronic properties, due to changes in band structure.[269] For example, 0D QDs usually exhibit an isotropic emission, but the 1D nanorods could show a polarized emission. (ref) Sun et al. reported a facile ligand-assisted precipitation approach under room temperature for colloidal synthesis of different morphologies of $CsPbX_3$ NCs by adjusting the ligands.[23] The tailorable morphologies of NCs would be achieved by the combination of different organic acid and amine ligands. The mixture of hexanoic acid and octylamine could shape the NCs into spherical QDs, the combination of oleic acid and dodecylamine could tailor the shape of NCs into nanocubes, acetate acid and dodecylamine will also generate nanocubes, and the oleic acid and octylamine would tailor NCs into 2D nanoplatelets.(Figure 4.4)[23] These different shapes of NCs show a shape-dependent PL within the whole visible spectral region and also a variable decay lifetime from several to tens to hundreds of nanoseconds. Davis et al. developed a straightforward, ligand-mediated synthesis approach for producing 2D Mn-doped $CsPbX_3$ nanoplatelets by controlling the composition and concentration of surface ligands. These include short carbon chain ligands (octanoic acid and octylamine) and long carbon chain ligands (oleic acid and oleylamine). This facile method offers a green chemistry strategy that operate experiments under room temperature and ambient conditions without the use of harsh acids and avoid excessive lead waste.[270]

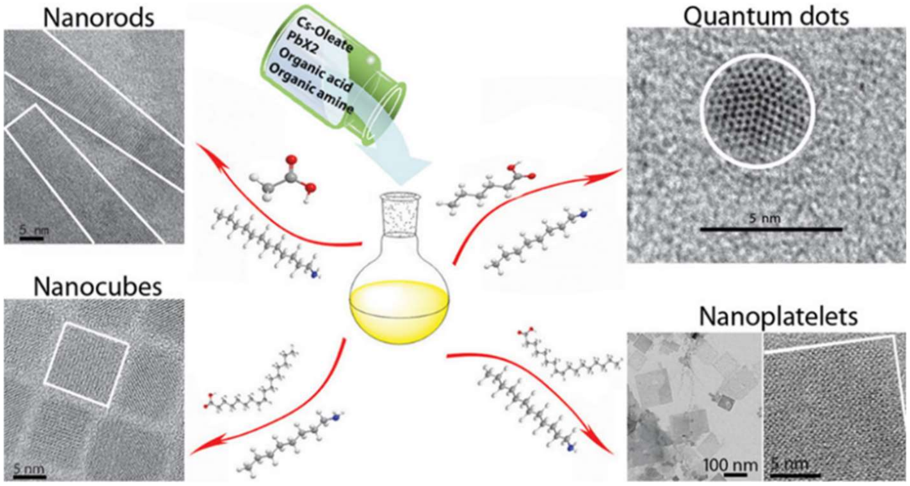

Figure 4.4 Schematic illustration of the Room-temperature synthesis route for different morphology of $CsPbX_3$ (X = Cl, Br, I) NCs, which mediated by organic acid and amine ligands.[23]

[23] [Reprinted (adapted) with permission from {Sun, S.; Yuan, D.; Xu, Y.; Wang, A.; Deng, Z., Ligand-Mediated Synthesis of Shape-Controlled Cesium Lead Halide Perovskite Nanocrystals via Reprecipitation Process at Room Temperature. ACS Nano 2016, 10 (3), 3648-57.}. Copyright {2016} American Chemical Society.]

However, the soft ionic nature and low formation energy of metal halide perovskites can lead to rapid decomposition and ion segregation.[250, 271] The inherent instability of perovskites became a significant barrier for practical applications, as when they are exposed to moisture, polar solvents, air, light, or heat perovskites degrade.[272, 273] For example, prolonged exposure to light can lead to the decomposition of PQDs, due to the formation of halogen vacancy-halogen interstitial pairs under illumination, causing halogens to migrate to the surface.[274]

In traditional metal chalcogenide NCs, shell coating with a different material for the formation of a core/shell heterostructure, has proven to significantly enhance the stability and optical properties of the NCs. Epitaxial core/shell structures are achieved when the lattice parameters and crystal structures between the core and shell materials are compatible, such as in the case of CdSe/CdS core/shell NCs with a small lattice mismatch (4%) between the same zinc blend crystal structure of the CdSe core and CdS shell.[5] Many epitaxial core/shell NC structures using III-V, II-VI, IV-VI and I-III-V group semiconductors have been reported with engineered optical, electrical, and magnetic properties.[77, 275, 276] Similar with the conventional core/shell semiconductor NCs, the passivation of a shell onto the perovskite NCs should also provide enhanced stability.

The inherent instability of PQDs necessitates strategies for enhancing their resistance to moisture and oxygen. Surface encapsulation methods not only prevent aggregation in solutions, thus mitigating anion exchange, but also reduces degradation when PQDs are exposed to polar solvents, air, high temperatures, and high-energy beams, attributed to the ionic nature of their crystalline structure. Effective surface passivation with alternative materials can significantly enhance the chemical, photonic, and thermal stabilities of PQDs. The growth of a shell on the surface of ionic perovskites is facilitated when the shell material also exhibits ionic characteristics. For instance, successful synthesis of heterostructures like $CsPbBr_3/Cs_4PbBr_6$ and $CsPbBr_3/Cs_2PbBr_5$ has been achieved through the addition or removal of $PbBr_2$/CsBr on $CsPbBr_3$ perovskite NCs.[277-280] However, rapid halide ion exchange and spontaneous phase transformations challenge the epitaxial growth of semiconductor NCs on surfaces using traditional wet colloidal chemistry synthesis methods.[281, 282] For ionic perovskites, surface passivation with a covalently bonded material could reduce surface defects, improve carrier transfer, expand the tunable optical range, and boost stability.[283, 284]

Binary II-VI and IV-VI chalcogenides as shell materials for perovskites to enhance the stability and optoelectronic properties have been investigated in recent years. Tang et al. synthesized $CsPbBr_3$/CdS core/shell NCs by using Cd-oleate and S-OAm as shell precursors.[24, 285] The absorption and PL spectra of the core/shell exhibited a blue shift compared with the pure perovskite which indicates an increasing bandgap of the core/shell NCs.(Figure 4.5) The PL QYs were reported to increase to 88% with significant added stability. The Chen group reported $CsPbBr_{3-x}I_x$/ZnS heterodimers with a longer PL lifetime and an increasing charge diffusion length which would benefit photovoltaic devices.[286]

However, the large difference in lattice parameters, crystal structure, and growth kinetics between ionic perovskites and covalent chalcogenides makes the epitaxial growth of a chalcogenide onto a perovskite still very challenging. For example, the bonding environment in perovskites is of a soft ionic nature, while in chalcogenides, it is covalent. Furthermore, for most II-VI group semiconductors, such as CdS or ZnS, the divalent metal ions are in tetrahedral coordination. In contrast, the B-site ions in perovskites, such as Pb^{2+} in $CsPbX_3$, are in octahedral coordination. In addition, there are different growth kinetics and rates for perovskites and chalcogenides, especially to form a perovskite shell on the top of II-VI QDs, the rapid formation of perovskite NCs usually makes it difficult to grow a perovskite shell slowly on the core QDs without additional perovskite nucleation. These differences create a high energetic barrier at the interface, which makes epitaxial growth problematic.[281]

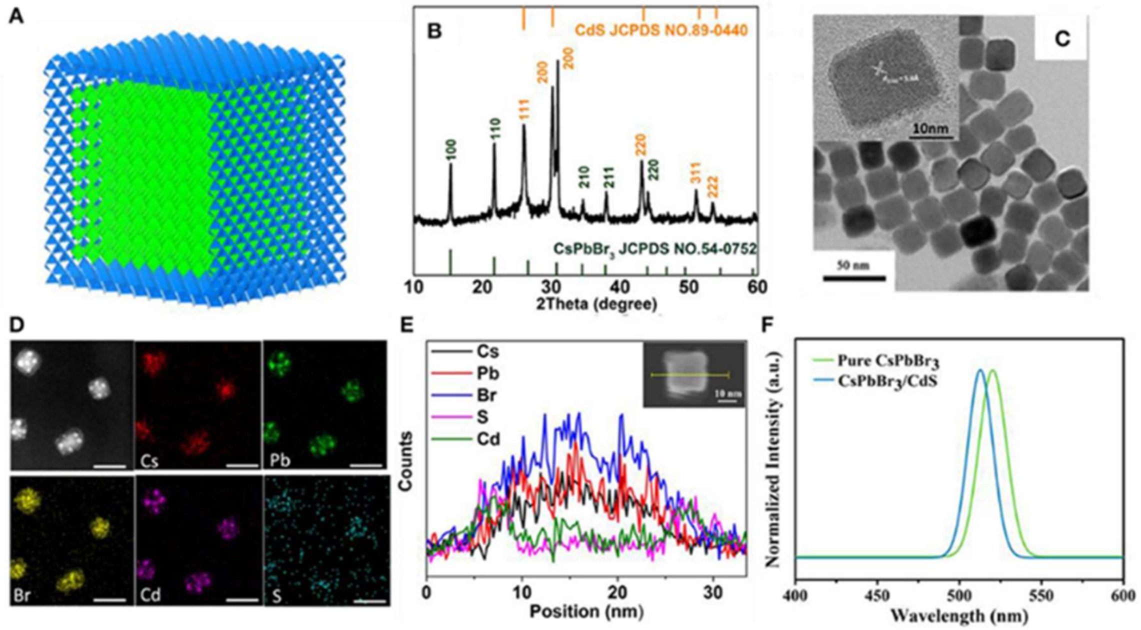

Figure 4.5 (a) Schematic of CsPbBr$_3$/CdS QDs and (b) XRD patterns of the CsPbBr$_3$/CdS QDs compared with standard peak position of CsPbBr$_3$ (Green line in the bottom) and CdS (Orange line in the top). (c) and (d) shows the TEM images and the mapping images of core/shell QDs. (e) EDX line profiles of Cs, Pb, Br, S, and Cd for CsPbBr$_3$/CdS QDs. and (f) PL emissions of the pure perovskite QDs (in green) and CsPbBr$_3$/CdS core/shell QDs (in blue).[24]

[24] [Reproduced with open access from {Tang, X.; Yang, J.; Li, S.; Chen, W.; Hu, Z.; Qiu, J., CsPbBr$_3$/CdS Core/Shell Structure Quantum Dots for Inverted Light-Emitting Diodes Application. Front Chem. 2019, 7, 499.} Copyright © 2019 Tang, Yang, Li, Chen, Hu and Qiu.]

From the discussions in chapters 2 and 3, it is fundamentally important to understand both the spatial distribution and location of dopants in NCs from a synthetic control perspective, and how dopant manipulation affects the resulting properties. In this chapter, we aim to systematically study the dopant behavior in perovskite-based core/shell NCs. The Mn doped perovskite/CdS and perovskite/ZnS core/shell heterostructures were synthesized using a combination of hot-injection and single-source precursor methods, as well as a precipitation approach. The dopant behavior was probed by optical spectroscopy.

4.2 Experimental

4.2.1 Chemicals, stock solutions and precursors

Chemicals: Cesium carbonate (Cs_2CO_3, 99.9%, Sigma-Aldrich), hydrobromic acid (HBr, 48% w/w in H_2O, Alfa Aesar), hydrochloric acid (HCl, 37% aqueous solution, Sigma-Aldrich), lead (II) bromide ($PbBr_2$, 99.999%, Sigma-Aldrich), lead (II) chloride ($PbCl_2$, 99.999%, Alfa Aesar), manganese (II) bromide ($MnBr_2$, >99%, Alfa Aesar), manganese (II) chloride ($MnCl_2$, >99%, Fisher), dimethyl sulfoxide (DMSO, 99.9%, Fisher), N,N-dimethylformamide (DMF, 99.9%, Fisher), cadmium chloride ($CdCl_2$, 99%, Fisher), sodium diethyldithiocarbamate (Na(DDTC), 98%, Fisher), zinc diethyldithiocarbamate ($Zn(DDTC)_2$, 97%, Sigma-Aldrich), 1-octadecene (ODE, technical grade 90%, Fisher), oleylamine (OAm, technical grade 70%, Sigma-Aldrich), oleic acid (OA, 90%, Fisher), trioctylphosphine (TOP, 97%, Fisher), toluene (99.8%, Pharmco), hexanes (98.5%, Pharmco), ethanol (99.5%, Pharmco), methanol (99.8%, Pharmco), methyl acetate (99%, Fisher) were purchased and used without further purification.

Stock solutions and precursors:

a) Preparation of oleylammonium halide salt (OAm-HX): The OAm-HX (OAm-Br, OAm-Cl) salt was synthesized through a modified procedure from the literature.[195, 240] In a typical 10 mL reaction synthesis, 10 mL of OAm, and 1.28 mL of HBr (1.0 mL of HCl) were loaded and mixed well in a 25 mL three neck flask. The following solidified mixture was heated to 80 °C under vacuum and refilled with Ar gas for 1 hour. Then the temperature was increased to 120 °C for 2 hours followed by another further 30 minutes under 150 °C. The liquid solution was then collected into a 20 mL vial with a septum. The stock solution could be stored under room temperature but need to be heated to 80 °C before using in the following experiment.

b) Preparation of cesium oleate (Cs-oleate) precursor: Cs-oleate precursor was synthesized based on reported method in literatures.[265] Briefly, 0.125 g (0.38 mmol) of Cs_2CO_3, 0.45 mL of OA, and 4.4 mL of ODE were mixed in a 25 mL three neck flask. The solution was heated to 120 °C under vacuum for 1 hour and heated to 150 °C under Ar for a further 30 minutes. The stock solution could be stored under room temperature but need to be heated to 120 °C before using in the following experiment.

c) Preparation of cadmium diethyldithiocarbamate ($Cd(DDTC)_2$): $Cd(DDTC)_2$ precursor was synthesized with slight modification based on reported method in literatures.[97] In a typical synthesis, $CdCl_2$ (0.504 g, 2.7 mmol) was dissolved in 18.4 mL of distilled water. $Na(DDTC)\cdot 3H_2O$ (1.242 g, 5.5 mmol) was mixed with 11.0 mL of distilled water and kept stirring until fully dissolved. Then, $Na(DDTC)\cdot 3H_2O$ aqueous solution was added dropwise into the flask containing $CdCl_2$ solution under vigorous stirring followed by slowly formed white precipitates of $Cd(DDTC)_2$ particles. The mixture was stirred for at least 1 hour under room temperature. Centrifuged all solution to obtain white precipitates and washed with methanol twice. The white $Cd(DDTC)_2$ particles were dried under vacuum.

4.2.2 Room temperature shell growth for Mn doped CdS/Perovskite core/shell heterojunctions

a) Synthesis of undoped and Mn doped CdS core QDs: Mn(II) doped CdS QDs were synthesized through a colloidal hot-injection technique as previously described.[17] Briefly, 41.2 mg (0.130 mmol) of Cd $(NO_3)_2\cdot 4H_2O$, 5.82 mg (0.033 mmol) of $Mn(NO_3)_2\cdot H_2O$, 0.167 mL of

DDT, and 10 mL of OAm were mixed in a three-neck flask. The mixture was degassed for 40 min at room temperature and another 10 min at 100 °C. The mixture was refilled with Ar and kept at 110 °C for 30 min. Then, 0.667 mL of a 0.2 M solution of sulfur in OAm was swiftly injected into the flask when the mixture was heated to 160 °C. After the injection, the temperature was set at 120 °C and degassed for 10 min. The temperature was then raised to 240 °C for nanocrystal growth for 5-10 min. The reaction was quenched by quickly removing the heating mantle and submerging the flask in a cold-water bath. After the reaction had been cooled below 100 °C, the product was dissolved in toluene and then crashed out by adding ethanol. The QDs were separated from solutions by centrifugation with a speed set to 5000 rpm at 15 °C for 5 min. The supernatant was discarded and the QDs in the precipitant were redissolved in toluene or hexane, and the cleaning process was repeated 3 more times before shell coating. For undoped CdS core QDs, the reaction starts without $Mn(NO_3)_2·H_2O$ and all other procedures are same as those for Mn^{2+} doped QDs.

The QDs were cleaned once using toluene and ethanol and redissolved in toluene for optical measurements. For XRD measurements, 4-6 additional washes using toluene and ethanol were performed.

b) Room temperature shell growth of perovskite through the ligand-assisted precipitation method, as previously described.[270, 287] A control reaction to synthesize $CsPbBr_3$ QDs was performed first. In a typical reaction, $PbBr_2$ (0.04 mmol) and CsBr (0.04 mmol) were mixed in a glass vial containing 1 mL of DMF, stirring or sonicating the solution until all particles are fully dissolved. In a separate tube, usually a 15 mL centrifuge tube, 0.1 mL of oleic acid (OA) and 0.05 mL of oleylamine (OAm) were thoroughly mixed before being added to the $PbBr_2$ and CsBr precursors. The above solution was then dropwise injected into a vial containing 10 mL of toluene under continuous stirring. Centrifuge the solution at 5000 rpm for 10 minutes and discard the precipitate. Wash the supernatant with acetonitrile. All operations were conducted at room temperature in an atmosphere without any protective measures.

For CdS/$CsPbBr_3$ core/shell heterostructures, add pre-synthesized CdS core into the toluene before injecting precursors and ligands. For $CsPbCl_3$ and CdS/$CsPbCl_3$ core/shell heterostructures, use $PbCl_2$, CsCl, and $MnCl_2$ precursors instead of Br-precursors, and keep all procedures the same as described above. For Mn-doped $CsPbBr_3$ shell growth, a separate $MnBr_2$ precursor was prepared by dissolving $MnBr_2$ into DMF. Adjusting the ratio between precursors could achieve different doping concentrations and compositions during the shell growth.

4.2.3 Single source shell precursors (SSP) method for Mn doped perovskite/CdS core/shell NCs

a) Synthesis of $CsPbX_3$ QDs was performed through the hot-injection method, as previously described.[239] Briefly, PbX_2 (0.188 mmol), such as $PbBr_2$ (0.069 g), or $PbCl_2$ (0.052 g), ODE (5 mL), OAm (0.5 mL) and OA (0.5 mL) were loaded in a three-neck flask. The mixture was degassed more than 1 hour at 120 °C followed by argon refilling. After complete solubilization of the $PbBr_2$ or $PbCl_2$ salt, the flask was heated up to 150 °C for Br-salt and 170 °C for Cl-salt. Swiftly injected the prepared Cs-oleate precursor (0.4 mL, 0.125 M in ODE) into the solution and quenched the reaction into an ice-water bath after 5 s. For $CsPbCl_3$, 1 mL of trioctylphosphine (TOP) was required in the beginning mixture.

Cleaned the $CsPbX_3$ NCs with toluene and methyl acetate and centrifuged 10 minutes with 5000 rpm. Dried NCs under vacuum.

b) Synthesis of $CsPbX_3$/CdS core/shell heterostructures by SSP method. Prepared $CsPbX_3$ powder (0.015 g), ODE (3 mL) and OAm-X (20 μL) were mixed in a three-neck flask and sonicated for 3 minutes. $Cd(DDTC)_2$ powder (5 ~ 10 mg) was added into the flask and sonicated for another 5 minutes. The solution was degassed at room temperature for 30 minutes and at 100 °C for at least 1 hour. Quenched the reaction at different times (10 minutes, 30 minutes, 60 minutes, etc.) into a cold-water bath. The resulting crude solution was then centrifuged for 10 minutes at 5000 rpm. The NCs were redispersed into toluene and cleaned with methyl acetate centrifugation where finally the NCs were dissolved in toluene for optical measurements.

4.2.4 Characterizations

Powder X-ray diffraction (XRD) patterns were taken on a Bruker D2 Phaser with a LYKXEYE 1-dimensional silicon strip detector using Cu Kα radiation (λ =1.5406 Å). Agilent Cary 60 UV-vis spectrophotometer was used to collect absorption spectra of the samples in a 1 cm quartz cell. PL measurements were conducted with a Horiba FluroMax Plus spectrofluorometer. Time-resolved emission measurements were performed using an Edinburgh FLS-980 fluorescence spectrometer equipped with 365 nm picoseconds pulsed lasers (EPLSs) and microsecond flashlamp (μF_2) to measure PL lifetime from a few nano seconds to seconds.

4.3 Results and Discussion

4.3.1 Doped and undoped CdS/Perovskite core/shell heterojunctions

CdS QDs were initially synthesized using a hot injection in colloidal solution. Subsequently, to grow the CdS/Perovskite core/shell NCs, the pre-synthesized CdS core was dissolved in toluene, followed by the room temperature ligand-assisted reprecipitation approach for shelling Mn-doped $CsPbBr_{3-x}Cl_x$ NCs perovskite. (Scheme 4.1)

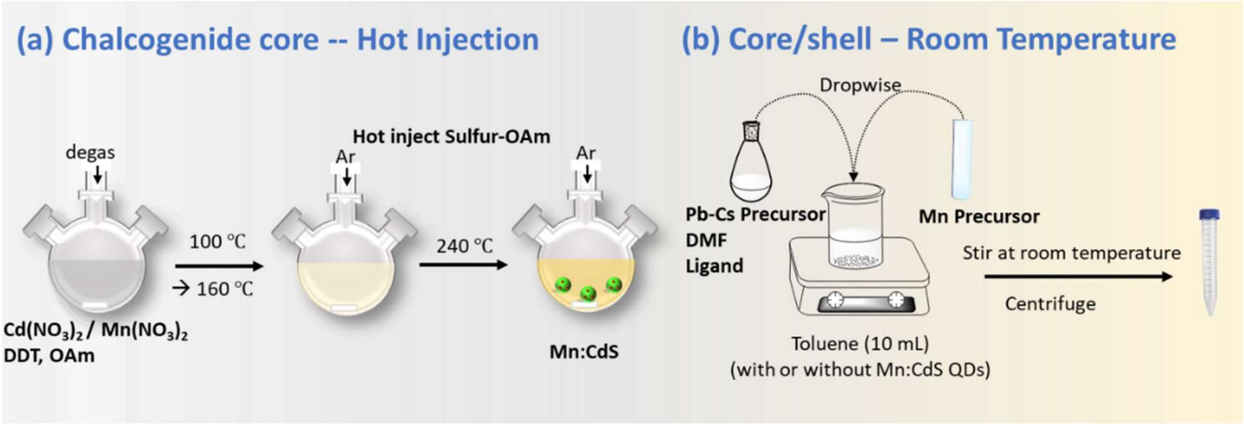

Scheme 4.1 Schematic illustration of the room-temperature synthesis of core/shell NCs.

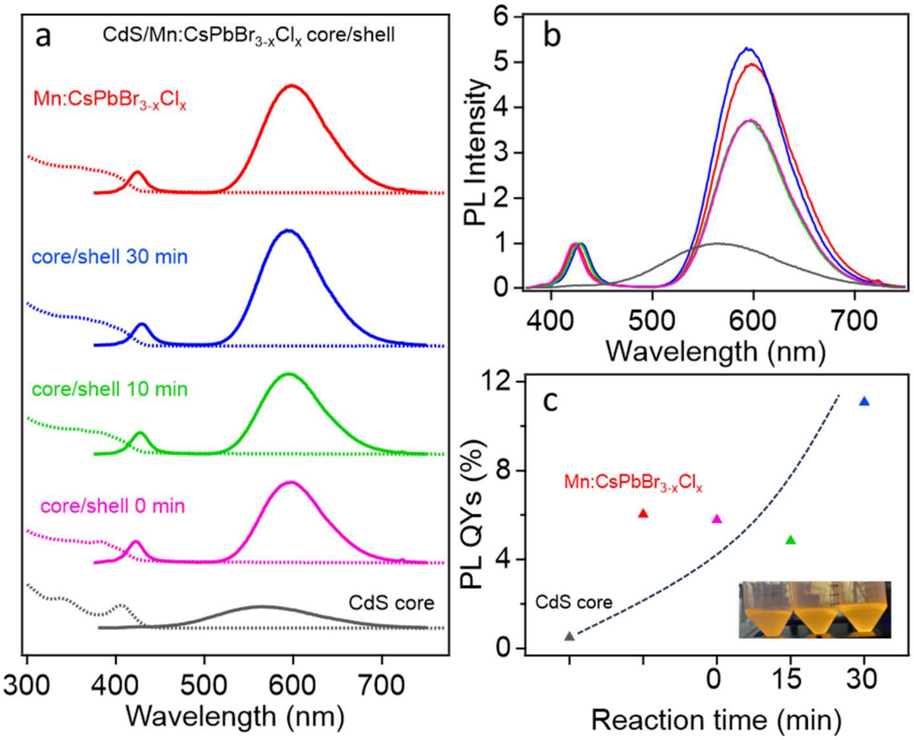

Figure 4.6 (a)The absorption and emission spectra of CdS core (gray curve), $Mn{:}CsPbBr_{3-x}Cl_x$ (red curve) and $CdS/Mn{:}CsPbBr_{3-x}Cl_x$ core/shell NCs (purple, green and blue curves) with different reaction times. (b) The emission comparison and (c) PL QYs of CdS core, $Mn{:}CsPbBr_{3-}$

$_xCl_x$ and CdS/Mn:CsPbBr$_{3-x}$Cl$_x$ core/shell NCs are shown. Inset figure shows optical images of three samples (0, 15, 30 minutes) under UV light.

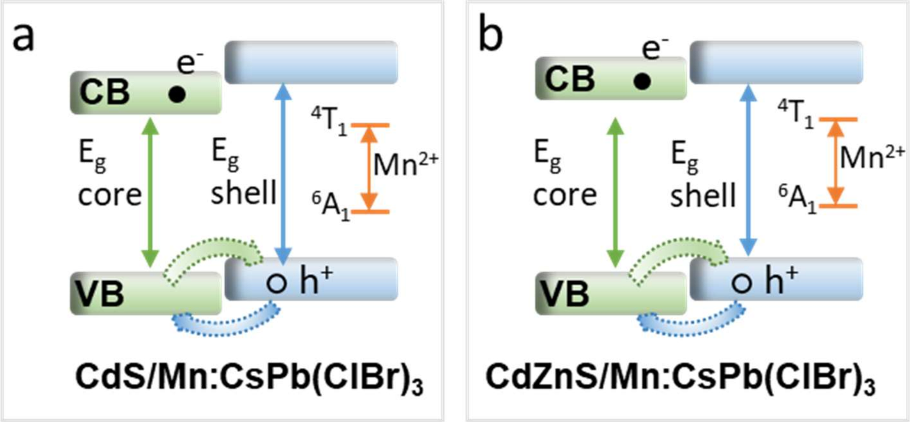

Scheme 4.2 Schematic illustration of type-II band alignment of (a) CdS/Mn:CsPbBr$_{3-x}$Cl$_x$ core/shell QDs and (b) CdZnS/Mn:CsPbBr$_{3-x}$Cl$_x$ core/shell QDs.

The first exciton absorption peak for the CdS core at 406 nm experiences a blue shift to 384 nm after the addition of perovskite precursors and does not shift with increasing reaction time. However, this 384 nm absorption peak could be assigned to the pure perovskite, like the red curve in figure 4.6 a. The emission spectrum of the CdS core displays a single broad emission peak around 570 nm, which indicates a large number of surface defects on the CdS core QDs. During the core/shell growth, dual emission peaks illustrate the band gap emission from the host lattice around 425 nm, and the Mn dopants emission around 595 nm due to excitonic recombination and Mn d-d transitions ($^4T_1$ to $^6A_1$), respectively. However, during core/shell synthesis, the absorption and emission peak positions and shapes remain unaltered with reaction time, which might indicate no core/shell QDs formation. Compared with pure Mn-doped perovskite NCs (shell material), they display a strong Mn emission peak around ~598 nm, with a slight shift (~4 nm) toward shorter wavelengths for the core/shell QDs. Depending on the type-II CdS/Mn:CsPbBr$_{3-x}$Cl$_x$ core/shell band alignment (Scheme 4.2),[288-291] the electron will be confined in the core, but the hole could be relocated in the core or in the shell, which is expected to result in a red shift of the PL spectrum. The PL QYs increased from 6% to 12% following the core/shell reaction, suggesting that the CdS core QDs in the initial solution might influence the emission, but this is not sufficient evidence for core/shell structure formation.

For a better understanding of the CdS/perovskite core/shell NCs, CdZnS/perovskite core/shell NCs with the similar type-II band alignment were synthesized for comparison using the same procedure but replacing the CdS core with a CdZnS core in the initial reaction. The optical results and host/Mn PL decay dynamics were shown in figures 4.7 and 4.8.

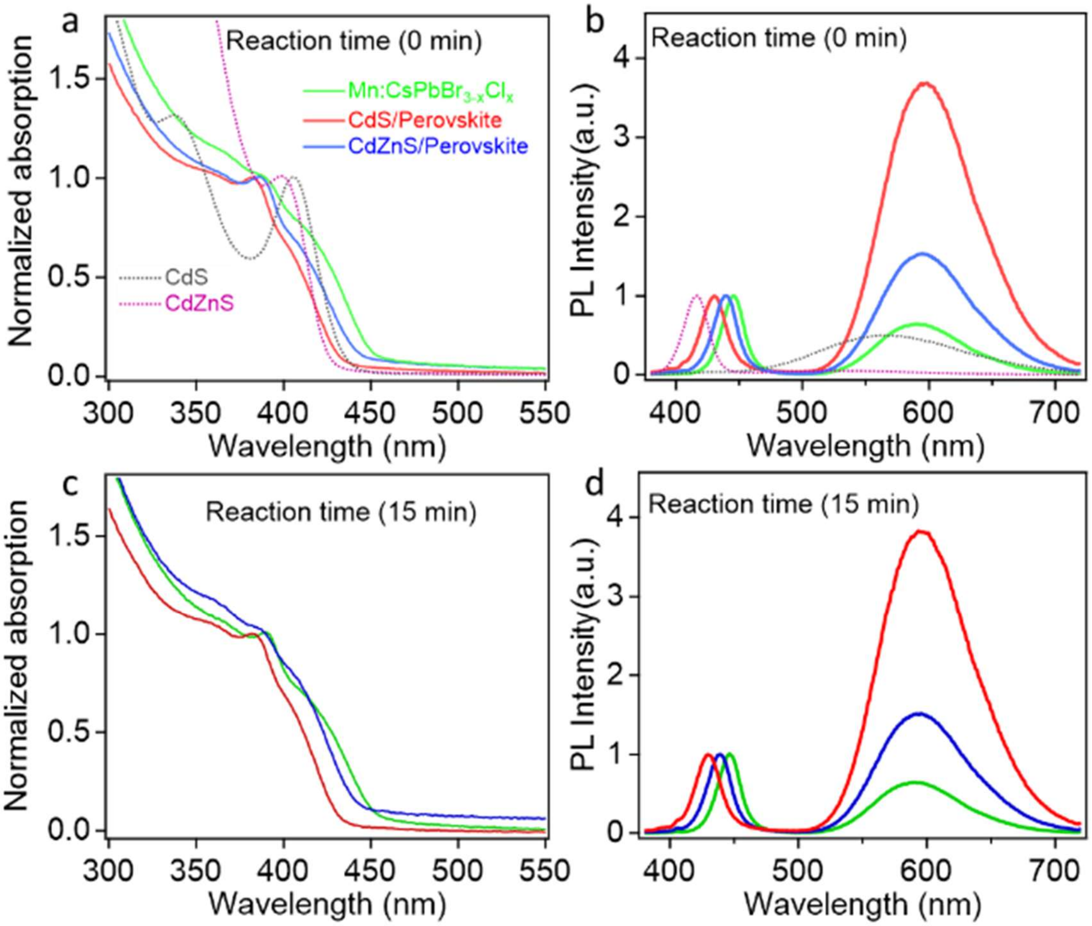

Figure 4.7 Normalized absorption and emission spectra of Mn:CsPbBr$_{3-x}$Cl$_x$ (green curve), CdS/Mn:CsPbBr$_{3-x}$Cl$_x$ (red curve), and CdZnS/Mn:CsPbBr$_{3-x}$Cl$_x$ (blue curve) core/shell NCs are shown under (a and b) 0 min and (c and d) 15 min of reaction time.

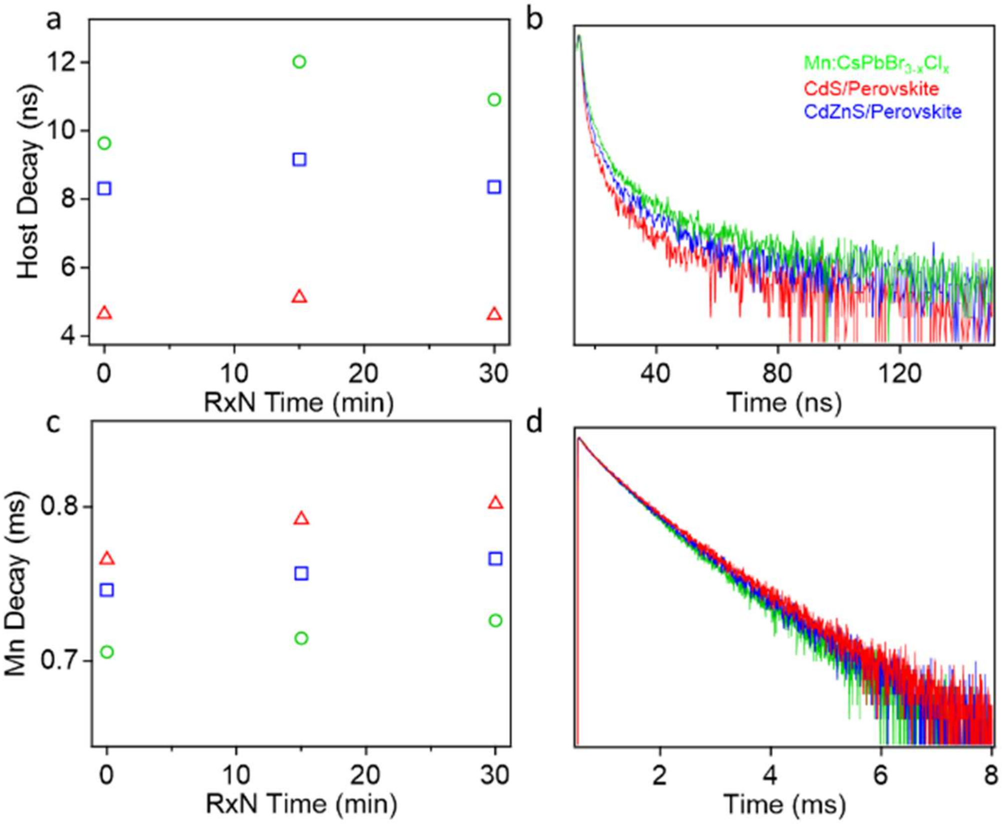

Figure 4.8 PL lifetime for Mn:CsPbBr$_{3-x}$Cl$_x$ (green curve), CdS/Mn:CsPbBr$_{3-x}$Cl$_x$ (red curve), and CdZnS/Mn:CsPbBr$_{3-x}$Cl$_x$ (blue curve) core/shell NCs are presented as follows: (a and b) host decay time, and (c and d) Mn decay time for the three samples, plotted as a function of reaction time. b and d show the lifetimes of the three samples at 0 min.

As shown in figure 4.7, the CdS/Mn:CsPbBr$_{3-x}$Cl$_x$ and CdZnS/Mn:CsPbBr$_{3-x}$Cl$_x$ core/shell heterostructures exhibit very different absorption peaks between the pure CdS core and CdZnS core. But they are similar to the absorption of pure Mn:CsPbBr$_{3-x}$Cl$_x$ NCs. The reaction time appears to have a minimal impact on the absorption and emission spectra, as all samples exhibit similar optical performance at 0 and 15 minutes. These consistent absorption profiles indicate that the optical absorption properties of the core perovskite structure are largely preserved, with little impact from the capping layer or specific modifications such as Mn doping. Nevertheless, while the absorption characteristics remain consistent across the three samples at the same reaction time, they display varying PL intensities. Both the CdS and CdZnS based core/shell samples exhibit distinct dual emission characteristics, similar to those of pure Mn-doped perovskites. However, samples with a CdZnS core generally show a slightly broader emission peak with lower intensity compared to those with a CdS core, suggesting better surface passivation and fewer non-radiative recombination sites, possibly due to the wider bandgap of CdZnS which could affect confinement and energy transfer dynamics.

Regarding the decay times for host and Mn of the three core/shell NC samples, the Mn-doped perovskite NCs exhibits the longest host decay and the shortest Mn decay, potentially due to more non-radiative pathways or less efficient charge carrier confinement, leading to faster recombination. In contrast, CdS/Mn:$CsPbBr_{3-x}Cl_x$ core/shell samples with a CdS core exhibit the shortest host decay and the longest Mn decay, possibly resulting from changes in inter-band dynamics. However, all samples show similar trends as a function of reaction time, which indicate no clear difference in lifetime observed during the shell coating time. As shown in scheme 4.2, both of CdS/Mn:$CsPbBr_{3-x}Cl_x$ and CdZnS/Mn:$CsPbBr_{3-x}Cl_x$ core/shell heterostructure have type-II band alignment, which is expected to have a longer lifetime than pure CdS or CdZnS core QDs (in the range of a few to tens of ns). But from figure 4.8, we could not observe obvious longer lifetime of the core/shell heterostructures, therefore, it may not support the hypothesis of core/shell formation. Previous literature indicates that overcoming the challenges associated with epitaxially passivating perovskites using chalcogenide semiconductor

NCs is difficult. Although both perovskite and chalcogenide NCs are colloidal NCs and can be synthesized using the high-temperature hot injection method, the fundamental differences between the ionic nature of perovskites and the covalent nature of chalcogenide NCs pose significant challenges in core/shell formation.[281]

4.3.2 Doped perovskite with CdS and ZnS shell by SSP shell coating method

As described in the experimental section, doped perovskites with a chalcogenide shell were synthesized by a combination of hot-injection synthesis of $CsPbX_3$ core reaction with a single source precursor shelling methods for II-VI shell growth. (Scheme 4.3)

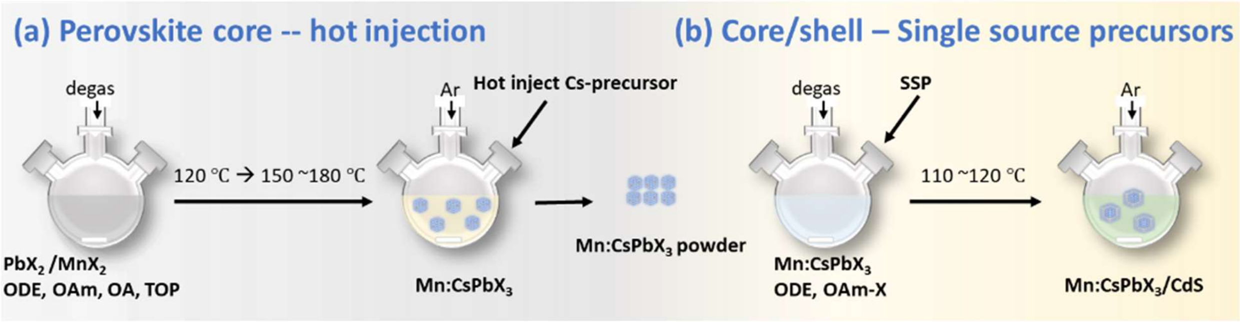

Scheme 4.3 Schematic of the synthetic route of (a) $CsPbCl_3$ and Mn:$CsPbCl_3$ perovskite core NCs via hot injection approach and (b) perovskite/chalcogenide core/shell heterostructures via single source precursor method.

We first synthesized Mn core-doped $CsPbBr_3$/CdS, and $CsPbBr_3$/ZnS core/shell heterostructures, however, no Mn PL was observed in small bandgap $CsPbBr_3$ NCs.[270] Therefore, to observe the Mn PL changes in doped NCs, we synthesized core/shell structures using Mn-doped larger bandgap $CsPbCl_3$ core NCs with a CdS shell. For the undoped $CsPbCl_3$/CdS core/shell heterostructures, Figure 4.9 demonstrates that the absorption and emission spectra exhibit similar spectra, including the shape and position of the peaks. Notably, the PL QYs of the core/shell NCs increased from 2% (undoped $CsPbCl_3$ NCs) to 18% (0 min core/shell NCs), indicating successful passivation. Additionally, slight changes in the full width at half maximum (FWHM) suggest alterations in size distribution due to shell formation.

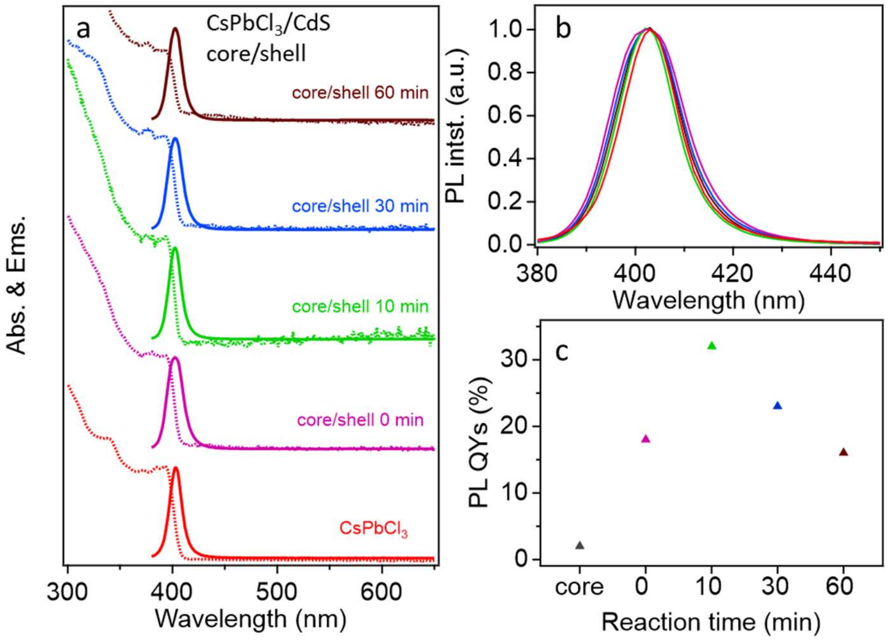

Figure 4.9 (a) Absorption (dashed line) and photoluminescence (solid line) spectra of $CsPbCl_3$ core (red), and $CsPbCl_3$/CdS core/shell heterostructures (colorful lines) with different reaction time (from 0 to 60 minutes). (b) Photoluminescence spectra of $CsPbCl_3$/CdS core/shell heterostructures. (c) The PL QYs changes of the $CsPbCl_3$ core and $CsPbCl_3$/CdS core/shell heterostructures as a function of reaction time.

Figure 4.10 and figure 4.11 illustrate that a low (Mn-to-Pb ratio: 2.0) and high (Mn-to-Pb ratio: 5.0) concentration of Mn ions was doped into $CsPbCl_3$ NCs, followed by CdS shell growth. The Mn PL peak in low concentration core/shell QDs samples, initially at 589 nm in the core, red-shifted to 595 nm after core/shell formation, indicating a change in pressure applied on the dopant ions by the shell thickness. However, the intensity of the Mn PL peak remained unchanged, suggesting that most of the Mn ions are confined to the $CsPbCl_3$ core. However, as shown in figure 4.11, the high concentration of Mn doped core/shell QDs show a clear decreasing trend in Mn PL intensity with reaction time, along with a blue shift in Mn PL emission peak position. The high concentration of Mn dopant ions introduced more complicated Mn-Mn interactions within the core. Therefore, the Mn PL intensity demonstrated a clear decrease as the shell passivation time increased, and the Mn PL peak position exhibited a blue shift towards shorter wavelengths, which might have resulted from the slight migration of Mn ions out of the core. The PL QYs for low Mn-doped core/shell NCs increased from 4.7% (low Mn:$CsPbCl_3$ NCs) to 18% (40 min core/shell NCs) and for samples with a high Mn concentration, they increased from 18% (high Mn:$CsPbCl_3$ NCs) to 80% (30 min core/shell NCs) as shown in Figure 4.12, consistent with observations in the PL spectra of samples with low and high Mn concentration.

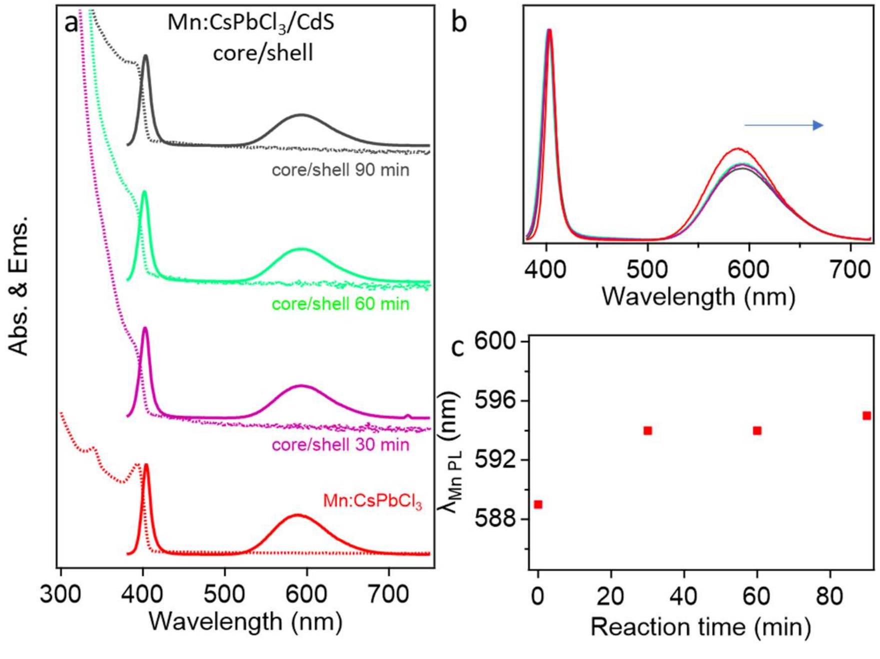

Figure 4.10 (a) Absorption (dashed line) and photoluminescence (solid line) spectra of low Mn concentration (Mn-to-Pb ratio: 2.0) of Mn: $CsPbCl_3$ core (red), and Mn:$CsPbCl_3$/CdS core/shell heterostructures (colorful lines) with different reaction time (from 30 to 90 minutes). (b) Photoluminescence spectra of Mn:$CsPbCl_3$/CdS core/shell heterostructures. The blue arrow

shows the wavelength shift with reaction time. (c) The changes of Mn PL peak position of the core/shell heterostructures as a function of reaction time.

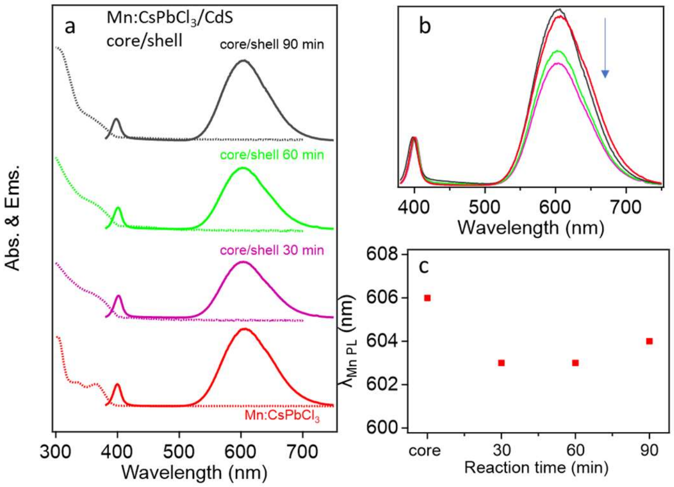

Figure 4.11 (a) Absorption (dashed line) and photoluminescence (solid line) spectra of high Mn concentration (Mn-to-Pb ratio: 5.0) of Mn: CsPbCl$_3$ core (red), and Mn:CsPbCl$_3$/CdS core/shell heterostructures (colorful lines) with different reaction time (from 30 to 90 minutes). (b) Photoluminescence spectra of Mn:CsPbCl$_3$/CdS core/shell heterostructures. The blue arrow shows the changes of the PL intensity. (c) The changes of Mn PL peak position of the core/shell heterostructures as a function of reaction time.

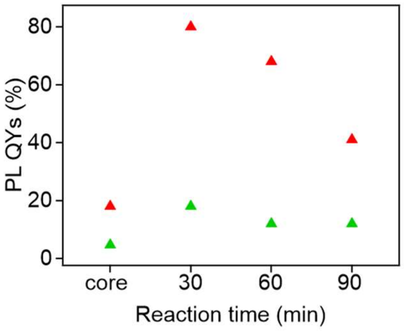

Figure 4.12 The PL QYs for low Mn concentration (Mn-to-Pb ratio: 2.0) of Mn:CsPbCl$_3$/CdS core/shell NCs (green markers) and for high Mn concentration (Mn-to-Pb ratio: 5.0) of Mn:CsPbCl$_3$/CdS core/shell NCs (red markers).

4.4 Conclusion and Future Research

Core/shell NCs are an intriguing strategy that offers significant potential to enhance stability and broaden the applications of perovskites. Nevertheless, the direct formation of shells on perovskite NCs poses considerable challenges, largely due to the soft ionic nature of the perovskite structures and the difficulty in finding shell materials that align well with the lattice structures of the cores. Ideally, the shell material should serve as a protective barrier against severe environmental conditions and should be engineered with a precisely controlled thickness to facilitate charge transfer at the interface.

In the case of perovskite/chalcogenide core/shell NCs, the large differences between ionic nature and covalent nature become a notable challenge. Another challenge is how to overcome the decomposition issue when shelling with chalcogenides under high temperatures, which is essential for the synthesis of colloidal chalcogenide QDs. It has been established that shell growth must occur at lower temperatures to prevent impurity formation and phase changes. Selecting shell precursors with lower reactivity and fine-tuning the growth duration might provide a gradual release of the precursors and prevent independent nucleation of the shell material, such as when using single source precursors.

In this chapter, we synthesized both CdS/perovskite and perovskite/CdS core/shell heterostructures. Utilizing the room-temperature precipitation method posed significant challenges in shell growth due to limited thermal energy, the rapid growth kinetics of perovskites, and the slower kinetics of shell passivation. Optical measurements indicated the possible formation of the core/shell heterojunctions, but more analysis using both XRD and TEM are needed to definitively prove the core/shell structures. Employing a single-source shelling precursor method for II-VI shell growth yielded promising results for core/shell formation.

Experiments with both low and high Mn concentrations in Mn:$CsPbCl_3$/CdS core/shell NCs show a decreased Mn PL over shell coating reaction time, potentially due to slight outward migration from the core during shell growth at high temperatures. However, further studies are needed to provide more evidence for the dopant behaviors in the perovskite-based core/shell NCs.

Chapter 5

Conclusions and Future Perspectives

5.1 Research Summary

The thesis explores the controllable and directional dopant migration behavior within core/multi-shell NCs. The first chapter provides an overview of several prior studies on the development of both doped and undoped core/shell nanomaterials, as well as the various dopant behaviors that could significantly affect the optical and electrical properties of doped NCs. In chapter 2, we delve into the Mn(II) outward migration towards the inserted alloyed layer with a smaller lattice mismatch in cationic size with the dopant before the outer ZnS shell coating onto the Mn:CdS QDs surface. This intentionally inserted alloyed layer (CdZnS) aims to reduce the lattice strain caused by the large cationic mismatch between the larger Cd(II) in the core and the smaller Zn(II) in the shell and promote the migration of Mn dopants from the core toward this alloyed layer. An optical probe using the PL ratio between host and Mn dopant was established based on the distance-dependent host-dopant coupling and host to dopant energy transfer. A successful inward migration was achieved in Mn shell doped core/multi-shell QDs, which is covered in chapter 3. The intentionally inserted alloyed CdZnS layer could be served as an atomic trap to facilitate dopant migration. Significantly, it was found that the initial doping site and environment is critical for efficient dopant trapping and migration. Specifically, a larger Cd(II) substitutional site (92 pm) for the Mn(II) dopant (80 pm), with larger local lattice distortion, allows for efficient atomic trapping and dopant migration, while Mn(II) dopant ions can be very stable with no significant migration when occupying a smaller Zn(II) substitutional site (74 pm).

Chapter 4 represents my initial effort toward the investigation of dopant behavior in ionic/covalent core/shell heterostructures, *i.e.*, ionic perovskite core with covalent shell, or covalent chalcogenide core with ionic perovskite shell. There are still unresolved challenges in this topic, but this chapter covers the discussion about the difficulties to achieve epitaxial core/shell NCs with large lattice and bonding differences between chalcogenide semiconductor and perovskite NCs; these initial results hopefully pave a way to the future for continued study of dopant behavior in perovskite-based core/shell NCs.

5.2 Future Research Directions

5.2.1 Further exploration of dopant migration behavior in different host lattice

Dopant migration behavior and dopant location within NCs are crucial for optical, electronic, and magnetic properties. The understanding of dopant behavior within different host lattices still needs to be further explored. The influence of the host lattice on dopant migration and/or dopant localization is a complex interplay of several factors, including lattice structure, atomic size mismatch, and the chemical nature of both the host and dopant ions. The crystal structure of the semiconductor, whether it's cubic, hexagonal, or another structure, could impact dopant diffusion. The size and shape of the substitutional doping sites and vacancies/holes in the host lattice determine the potential sites where dopants can fit. For example, a tightly packed cubic structure may offer less space for larger dopant atoms, leading to limited diffusion or the formation of defect sites.[15]

Up to date, most studies on Mn dopants migration or diffusion were related to the CdS QDs or CdS/ZnS core/shell QDs.[12, 123, 147, 292] Only a few cases focus on dopant migration or diffusion behavior of Mn doping into other host lattices have been reported to date. For instance, Jamil and Shaw reported that Mn ions diffusion in CdTe NCs depends on the Cd vacancies, which are further affected by the temperature.[187] Li et al. in our group previously studied Mn-Mn interactions and host-Mn energy transfer in doped 1-D nanowires (NWs) and found that Mn dopant ions tend to migrate from the core to the alloyed interface in quasi type-II ZnSe/CdS NWs and ZnSe/CdS/ZnS core/shell NWs. This migration significantly affects the host-dopant coupling and the optical properties.[65]

However, besides II-VI chalcogenide semiconductors, the migration behavior and distribution of dopants inside NCs, such as those doped in $CuInS_2$/ZnS core/shell and perovskite-based core/shell NCs are not fully understood for other commonly explored Mn-doped NCs.

5.2.2 Monovalent ion ($Cu^{+/2+}$ and Ag^{+}) doping in CdS/ZnS core/shell system

Many transition metal ions have been introduced in NC lattices, resulting in varied doping concentrations, optical, and magnetic properties. It would be very interesting to study the migration behavior of highly mobile monovalent dopant ions in the host NC lattice. Besides Mn^{2+}, $Cu^{+/2+}$ and Ag^{+} are the other two most common dopants in semiconductor NCs. The Peng group developed a method for doping ZnSe NCs with copper using a growth-doping approach. They observed a noticeable red shift in the emission peak as the position of the dopant shifted from the surface to the interior of the NCs.[11] In comparison to Mn-doped semiconductor NCs, the synthesis of Cu-doped NCs has received less focus due to the challenges in determining the oxidation state and location of Cu ions within the structure. Many unresolved questions surround the Cu dopant emission, such as the origin of its emission, reasons for its higher intensity, tunability, potential involvement of Cu d-states, emission spectral width, and other related properties.[293]

Monovalent Cu^{+} and Ag^{+} ions have significantly larger diffusion coefficients than divalent ions, such as Mn^{2+}, in various semiconductors.[294, 295] For example, the activation energies (E_a) for ion diffusion of Cu(I) and Mn(II) ions in ZnS are 0.64 and 2.46 eV, respectively.[294] In addition, charge compensation, by surface or thermally generated charge carriers, is expected in the heterovalent doped II-VI lattice for sustaining electroneutrality.[296] Consequently, diffusion and migration of such monovalent dopant ions in II-VI NCs might be more complicated and difficult to control.

An additional challenge involves the oxidation state of Cu ions in the doped semiconductor system. There has been continuous debate regarding the presence of both Cu^+ and Cu^{2+} oxidation states, with evidence supporting each. Typically, Cu^{2+} salts are used as the doping source, leading many researchers to believe that Cu^{2+} ions maintain their +2 oxidation state when incorporated into group II-VI semiconductors. However, there are instances in ZnS and CdS hosts where it has been observed that sulfide ions reduce Cu(II) to Cu(I), as confirmed by EPR measurements, thereby establishing Cu(I) as a stable oxidation state in these contexts. These conflicting views on the Cu oxidation state pose significant challenges in defining the mechanisms behind Cu dopant emission. Thus, comprehensive scientific investigations are necessary to fully understand the photophysical processes in these doped NCs.

5.2.3 Mn^{2+} and $Cu^{+/2+}$ dual ion doping into NCs

Co-doping with dual transition metal ions into NCs is a useful technique in the development of materials with specific optical and electrical properties. For example, Er-based amplifiers often introduce a co-dopant, such as Yb, to broaden the absorption cross-sections, thereby enhancing the optical gain. Studies of the amplifiers using both Er, and Yb usually focused on the interaction between these co-dopants, involving the alternation of their concentration and ratios due to the optical gain, heavily relies on the efficiency of energy transfer between dopants.[297-299] In II-VI chalcogenide semiconductor NCs, by incorporating both Mn^{2+}

and $Cu^{+/2+}$ into NCs with a bandgap around 3.10 eV, such as CdS or ZnSe, could achieve white light emission.[300] ZnSe QDs doped with Mn typically exhibit an orange emission at approximately 590 nm due to the $^4T_1$–$^6A_1$ transition of Mn^{2+}.[133] Likewise, ZnSe QDs doped with Cu are known to emit blue-green light around 500 nm.[301, 302] Consequently, co-doping ZnSe QDs with both Cu and Mn could potentially enable the production of a white light emission. In addition to white light, the migration of these dual dopants could allow for adjustable tri-emission (from the host lattice, $Cu^{+/2+,}$ and Mn^{2+}) depending on the dopants' location within the NCs. However, incorporating two different dopant ions presents multiple challenges, including the coordination of two dopants' reactivity, their oxidation states, and their even distribution within the nanocrystal. In the case of Mn, the electron and hole created by the excitation of the host lattice migrate to its d-states ($^4T_1$–$^6A_1$), where they recombine. In contrast, for Cu-doped systems, either the electron or the hole moves to the Cu state, leading to recombination within the Cu state while the other carrier remains in the host band. These complex interactions in the recombination mechanism alters their emission characteristics, and became a large challenge in the understanding of Mn and Cu co-doping in NCs.[303]

Given these challenges, it's clear that optimized synthetic parameters, including cation reactivity, reaction ligands, and temperatures, are necessary to achieve stable, uniformly dual-doped QDs; dual doped systems offer unique properties to better understanding and control of dopant migration behavior.

5.2.4 New characterization techniques for dopant location and distribution in NCs with high spatial resolution

It is critical to develop characterization techniques to visualize dopant location inside NCs with high spatial and temporal resolution. Much of the challenge pertains to the fact that limited experimental tools have sub-nanometer resolution capable of studying the dopant location, interface depth, and composition gradients in NCs. In future studies, high-resolution transmission electron microscopy (HR-TEM), scanning transmission electron microscope (STEM), energy-dispersive X-ray spectroscopy (EDS), and X-ray absorption fine structure (XAFS) analysis could be applied to map and track the dopant sites/movement as well as to detail the local-composition inside host NCs. For example, XAFS is a powerful tool that could interrogate the location of the dopant ions, providing valuable information regarding the distance between elements of interest and surrounding atoms, as well as grant aspects pertaining to local lattice perturbations caused by lattice mismatch.[304-307] In addition, XAFS measurements could probe the electronic and atomic structure of each element within the NCs, and use changes in signal to validate the dopant migration to the surface or interface region.[304, 305] For example, Mn, Cd, and Zn K-edge XAFS will be used to probe the local bonding and site symmetry of Mn:CdS/ZnS core/shell NCs. In addition, theoretical DFT calculations could be performed to establish realistic models of dopants inside NCs and provide more evidence for dopant migration.

References

1. McNeil, S. E., Nanotechnology for the biologist. *Journal of Leukocyte Biology* **2005,** *78* (3), 585-594.

2. Chen, G.; Roy, I.; Yang, C.; Prasad, P. N., Nanochemistry and Nanomedicine for Nanoparticle-based Diagnostics and Therapy. *Chem. Rev.* **2016,** *116* (5), 2826-85.

3. Smith, A. M.; Nie, S., Chemical analysis and cellular imaging with quantum dots. *Analyst* **2004,** *129* (8), 672-7.

4. Reiss, P.; Protiere, M.; Li, L., Core/Shell semiconductor nanocrystals. *Small* **2009,** *5* (2), 154-68.

5. Nan, W.; Niu, Y.; Qin, H.; Cui, F.; Yang, Y.; Lai, R.; Lin, W.; Peng, X., Crystal structure control of zinc-blende CdSe/CdS core/shell nanocrystals: synthesis and structure-dependent optical properties. *J. Am. Chem. Soc.* **2012,** *134* (48), 19685-93.

6. Zheng, W.; Wang, Z.; van Tol, J.; Dalal, N. S.; Strouse, G. F., Alloy formation at the tetrapod core/arm interface. *Nano Lett.* **2012,** *12* (6), 3132-7.

7. Makkar, M.; Viswanatha, R., Frontier challenges in doping quantum dots: synthesis and characterization. *RSC Adv.* **2018,** *8* (39), 22103-22112.

8. Zhao, Y.; Rabouw, F. T.; Puffelen, T. v.; Walree, C. A. v.; Gamelin, D. R.; de Mello Donegá, C.; Meijerink, A., Lanthanide-Doped CaS and SrS Luminescent Nanocrystals: A Single-Source Precursor Approach for Doping. *J. Am. Chem. Soc.* **2014,** *136* (47), 16533-16543.

9. Pradhan, N.; Sarma, D. D., Advances in Light-Emitting Doped Semiconductor Nanocrystals. *J. Phys. Chem. Lett.* **2011,** *2* (21), 2818-2826.

10. Norris, D. J.; Yao, N.; Charnock, F. T.; Kennedy, T. A., High-Quality Manganese-Doped ZnSe Nanocrystals. *Nano Lett.* **2000,** *1* (1), 3-7.

11. Pradhan, N.; Goorskey, D.; Thessing, J.; Peng, X., An alternative of CdSe nanocrystal emitters: pure and tunable impurity emissions in ZnSe nanocrystals. *J. Am. Chem. Soc.* **2005,** *127* (50), 17586-7.

12. Yang, Y.; Chen, O.; Angerhofer, A.; Cao, Y. C., Radial-position-controlled doping in CdS/ZnS core/shell nanocrystals. *J. Am. Chem. Soc.* **2006,** *128* (38), 12428-9.

13. Zheng, W.; Wang, Z.; Wright, J.; Goundie, B.; Dalal, N. S.; Meulenberg, R. W.; Strouse, G. F., Probing the Local Site Environments in Mn:CdSe Quantum Dots. *J. Phys. Chem. C* **2011,** *115* (47), 23305-23314.

14. Hofman, E.; Khammang, A.; Wright, J. T.; Li, Z. J.; McLaughlin, P. F.; Davis, A. H.; Franck, J. M.; Chakraborty, A.; Meulenberg, R. W.; Zheng, W., Decoupling and Coupling of

the Host-Dopant Interaction by Manipulating Dopant Movement in Core/Shell Quantum Dots. *J. Phys. Chem. Lett.* **2020,** *11* (15), 5992-5999.

15. Smart, L.; Moore, E. E. A., Solid state chemistry : an introduction. *CRC Press* **2012**.

16. Vlaskin, V. A.; Barrows, C. J.; Erickson, C. S.; Gamelin, D. R., Nanocrystal diffusion doping. *J. Am. Chem. Soc.* **2013,** *135* (38), 14380-9.

17. Hofman, E.; Robinson, R. J.; Li, Z. J.; Dzikovski, B.; Zheng, W., Controlled Dopant Migration in CdS/ZnS Core/Shell Quantum Dots. *J. Am. Chem. Soc.* **2017,** *139* (26), 8878-8885.

18. Li, C.; Lu, X.; Ding, W.; Feng, L.; Gao, Y.; Guo, Z., Formability of ABX_3 (X = F, Cl, Br, I) halide perovskites. *Acta Crystallographica Section B* **2008,** *64* (6), 702-707.

19. Li, S.; Lin, H.; Chu, C.; Martin, C.; MacSwain, W.; Meulenberg, R. W.; Franck, J. M.; Chakraborty, A.; Zheng, W., Interfacial B-Site Ion Diffusion in All-Inorganic Core/Shell Perovskite Nanocrystals. *ACS Nano* **2023,** *17* (22), 22467-22477.

20. da Silva, E. L.; Skelton, J. M.; Parker, S. C.; Walsh, A., Phase stability and transformations in the halide perovskite $CsSnI_3$. *Phys. Rev. B* **2015,** *91* (14), 144107.

21. Flatken, M. The early stages of halide perovskites thin film formation. **2022**.

22. Das Adhikari, S.; Dutta, S. K.; Dutta, A.; Guria, A. K.; Pradhan, N., Chemically Tailoring the Dopant Emission in Manganese-Doped $CsPbCl_3$ Perovskite Nanocrystals. *Angew Chem. Int. Ed. Engl.* **2017,** *56* (30), 8746-8750.

23. Sun, S.; Yuan, D.; Xu, Y.; Wang, A.; Deng, Z., Ligand-Mediated Synthesis of Shape-Controlled Cesium Lead Halide Perovskite Nanocrystals via Reprecipitation Process at Room Temperature. *ACS Nano* **2016,** *10* (3), 3648-57.

24. Tang, X.; Yang, J.; Li, S.; Chen, W.; Hu, Z.; Qiu, J., CsPbBr(3)/CdS Core/Shell Structure Quantum Dots for Inverted Light-Emitting Diodes Application. *Front Chem.* **2019,** *7*, 499.

25. Bailey, R. E.; Smith, A. M.; Nie, S., Quantum dots in biology and medicine. *Physica E: Low-dimensional Systems and Nanostructures* **2004,** *25* (1), 1-12.

26. Smith, A. M.; Gao, X.; Nie, S., Quantum Dot Nanocrystals for In Vivo Molecular and Cellular Imaging¶. *Photochemistry and Photobiology* **2004,** *80* (3).

27. Jang, Y.; Shapiro, A.; Isarov, M.; Rubin-Brusilovski, A.; Safran, A.; Budniak, A. K.; Horani, F.; Dehnel, J.; Sashchiuk, A.; Lifshitz, E., Interface control of electronic and optical properties in IV-VI and II-VI core/shell colloidal quantum dots: a review. *Chem. Commun. (Camb)* **2017,** *53* (6), 1002-1024.

28. Knowles, K. E.; Hartstein, K. H.; Kilburn, T. B.; Marchioro, A.; Nelson, H. D.; Whitham, P. J.; Gamelin, D. R., Luminescent Colloidal Semiconductor Nanocrystals Containing Copper: Synthesis, Photophysics, and Applications. *Chem. Rev.* **2016,** *116* (18), 10820-51.

29. Lohse, S. E.; Murphy, C. J., Applications of colloidal inorganic nanoparticles: from medicine to energy. *J. Am. Chem. Soc.* **2012,** *134* (38), 15607-20.

30. Yang, Y.; Hu, K.; Zhang, P.; Zhou, P.; Duan, X.; Sun, H.; Wang, S., Manganese-Based Micro/Nanomotors: Synthesis, Motion, and Applications. *Small* **2021,** *17* (50), e2100927.

31. Chen, X.; Li, C.; Gratzel, M.; Kostecki, R.; Mao, S. S., Nanomaterials for renewable energy production and storage. *Chem. Soc. Rev.* **2012,** *41* (23), 7909-37.

32. Kovalenko, M. V.; Protesescu, L.; Bodnarchuk, M. I., Properties and potential optoelectronic applications of lead halide perovskite nanocrystals. *Science* **2017,** *358* (6364), 745-750.

33. Jang, E.; Jang, H., Review: Quantum Dot Light-Emitting Diodes. *Chem. Rev.* **2023**.

34. Wu, P.; Miao, L. N.; Wang, H. F.; Shao, X. G.; Yan, X. P., A multidimensional sensing device for the discrimination of proteins based on manganese-doped ZnS quantum dots. *Angew Chem. Int. Ed. Engl.* **2011,** *50* (35), 8118-21.

35. Muska, M.; Yang, J.; Sun, Y.; Wang, J.; Wang, Y.; Yang, Q., $CoSe_2$ Nanoparticles Dispersed in WSe_2 Nanosheets for Efficient Electrocatalysis and Supercapacitance Applications. *ACS Applied Nano Materials* **2021,** *4* (6), 5796-5807.

36. Li, H.; Jiao, J.; Ye, Q.; Wu, Z.; Luo, D.; Xiong, D., Controllable synthesis of CdSe/ZnS core–shell quantum dots by one-step thermal injection and application in light-emitting diodes. *Journal of Materials Science: Materials in Electronics* **2021,** *32* (17), 22024-22034.

37. Rhee, S.; An, K.; Kang, K.-T., Recent Advances and Challenges in Halide Perovskite Crystals in Optoelectronic Devices from Solar Cells to Other Applications. *Crystals* **2020,** *11* (1).

38. Gbashi, K. R.; Muhi, M. A. H.; Jabbar, A. A.; Mahmood, N. B.; Hasan, R. F., Copper dopants impact enhanced behavior of Mn:Cu co-doped CdS nanocrystals (quantum dots) and their characteristics for optoelectronic applications. *Applied Physics A* **2020,** *126* (8).

39. Bera, R.; Dutta, A.; Kundu, S.; Polshettiwar, V.; Patra, A., Design of a CdS/CdSe Heterostructure for Efficient H_2 Generation and Photovoltaic Applications. *J. Phys. Chem. C* **2018,** *122* (23), 12158-12167.

40. Wang, T.; Chai, Y.; Ma, D.; Chen, W.; Zheng, W.; Huang, S., Multidimensional CdS nanowire/$CdIn_2S_4$ nanosheet heterostructure for photocatalytic and photoelectrochemical applications. *Nano Research* **2017,** *10* (8), 2699-2711.

41. Ghosh Chaudhuri, R.; Paria, S., Core/shell nanoparticles: classes, properties, synthesis mechanisms, characterization, and applications. *Chem. Rev.* **2012,** *112* (4), 2373-433.

42. Han, L.; Qin, D.; Jiang, X.; Liu, Y.; Wang, L.; Chen, J.; Cao, Y., Synthesis of high quality zinc-blende CdSe nanocrystals and their application in hybrid solar cells. *Nanotechnology* **2006,** *17* (18), 4736-42.

43. Bryan, J. D.; Gamelin, D. R., Doped Semiconductor Nanocrystals: Synthesis, Characterization, Physical Properties, and Applications. *Prog. Inorg. Chem.* **2005,** *54*, 47-126.

44. Wang, C. W.; Orrison, C.; Son, D. H., Hot electrons generated from Mn-doped quantum dots via upconversion for photocatalysis applications. *Bulletin of the Korean Chemical Society* **2022,** *43* (4), 492-500.

45. Talapin, D. V.; Lee, J. S.; Kovalenko, M. V.; Shevchenko, E. V., Prospects of colloidal nanocrystals for electronic and optoelectronic applications. *Chem. Rev.* **2010,** *110* (1), 389-458.

46. Shafiee, A.; Rabiee, N.; Ahmadi, S.; Baneshi, M.; Khatami, M.; Iravani, S.; Varma, R. S., Core–Shell Nanophotocatalysts: Review of Materials and Applications. *ACS Applied Nano Materials* **2022,** *5* (1), 55-86.

47. Fu, J.; Liu, J.; Yuan, L.; Pan, Q.; Chen, S.; Hu, Y.; Chen, J.; Ma, W.; Zhang, Q.; Liu, Z.; Cao, M., 3D/2D Core/Shell Perovskite Nanocrystals for High-Performance Solar Cells. *Small* **2023,** *19* (17), e2207312.

48. King, R. R.; Law, D. C.; Edmondson, K. M.; Fetzer, C. M.; Kinsey, G. S.; Yoon, H.; Sherif, R. A.; Karam, N. H., 40% efficient metamorphic GaInP⁄GaInAs⁄Ge multijunction solar cells. *Applied Physics Letters* **2007,** *90* (18).

49. Lin, S.; Peng, X., Current Status and Challenges of Solar Cells Based on Semiconductor Nanocrystals. *Energy & Fuels* **2021,** *35* (23), 18928-18941.

50. Pan, Z.; Zhang, H.; Cheng, K.; Hou, Y.; Hua, J.; Zhong, X., Highly efficient inverted type-I CdS/CdSe core/shell structure QD-sensitized solar cells. *ACS Nano* **2012,** *6* (5), 3982-91.

51. Lee, Y.-L.; Lo, Y.-S., Highly Efficient Quantum-Dot-Sensitized Solar Cell Based on Co-Sensitization of CdS/CdSe. *Adv. Funct. Mater* **2009,** *19* (4), 604-609.

52. Ahn, N.; Livache, C.; Pinchetti, V.; Klimov, V. I., Colloidal Semiconductor Nanocrystal Lasers and Laser Diodes. *Chem. Rev.* **2023,** *123* (13), 8251-8296.

53. Zhu, H.; Fu, Y.; Meng, F.; Wu, X.; Gong, Z.; Ding, Q.; Gustafsson, M. V.; Trinh, M. T.; Jin, S.; Zhu, X. Y., Lead halide perovskite nanowire lasers with low lasing thresholds and high quality factors. *Nat. Mater* **2015,** *14* (6), 636-42.

54. Wang, Y.; Li, X.; Nalla, V.; Zeng, H.; Sun, H., Solution-Processed Low Threshold Vertical Cavity Surface Emitting Lasers from All-Inorganic Perovskite Nanocrystals. *Adv. Funct. Mater* **2017,** *27* (13).

55. Najafi, A.; Tarasek, S.; Delikanli, S.; Zhang, P.; Norden, T.; Shendre, S.; Sharma, M.; Bhattacharya, A.; Taghipour, N.; Pientka, J.; Demir, H. V.; Petrou, A.; Thomay, T., CdSe/CdMnS Nanoplatelets with Bilayer Core and Magnetically Doped Shell Exhibit Switchable Excitonic Circular Polarization: Implications for Lasers and Light-Emitting Diodes. *ACS Appl. Nano Mater* **2020,** *3* (4), 3151-3156.

56. Li, S. N.; Pan, J. L.; Yu, Y. J.; Zhao, F.; Wang, Y. K.; Liao, L. S., Advances in Solution-Processed Blue Quantum Dot Light-Emitting Diodes. *Nanomaterials (Basel)* **2023,** *13* (10).

57. Li, Z.; Wei, J.; Wang, F.; Tang, Y.; Li, A.; Guo, Y.; Huang, P.; Brovelli, S.; Shen, H.; Li, H., Carrier Dynamics in Alloyed Chalcogenide Quantum Dots and Their Light-Emitting Devices. *Adv. Energy Mater* **2021,** *11* (40).

58. Li, X.; Wu, Y.; Zhang, S.; Cai, B.; Gu, Y.; Song, J.; Zeng, H., $CsPbX_3$Quantum Dots for Lighting and Displays: Room-Temperature Synthesis, Photoluminescence Superiorities, Underlying Origins and White Light-Emitting Diodes. *Adv. Funct. Mater* **2016,** *26* (15), 2435-2445.

59. Yuan, X.; Hua, J.; Zeng, R.; Zhu, D.; Ji, W.; Jing, P.; Meng, X.; Zhao, J.; Li, H., Efficient white light emitting diodes based on Cu-doped ZnInS/ZnS core/shell quantum dots. *Nanotechnology* **2014,** *25* (43), 435202.

60. Algar, W. R.; Massey, M.; Rees, K.; Higgins, R.; Krause, K. D.; Darwish, G. H.; Peveler, W. J.; Xiao, Z.; Tsai, H. Y.; Gupta, R.; Lix, K.; Tran, M. V.; Kim, H., Photoluminescent Nanoparticles for Chemical and Biological Analysis and Imaging. *Chem. Rev.* **2021,** *121* (15), 9243-9358.

61. Medintz, I. L.; Uyeda, H. T.; Goldman, E. R.; Mattoussi, H., Quantum dot bioconjugates for imaging, labelling and sensing. *Nat. Mater* **2005,** *4* (6), 435-46.

62. Alivisatos, A. P., Semiconductor Clusters, Nanocrystals, and Quantum Dots. *Science* **1996,** *271* (5251), 933-937.

63. Manna, L.; Scher, E. C.; Li, L. S.; Alivisatos, A. P., Epitaxial growth and photochemical annealing of graded CdS/ZnS shells on colloidal CdSe nanorods. *J. Am. Chem. Soc.* **2002,** *124* (24), 7136-45.

64. Zhang, J.; Qiao, S. Z.; Qi, L.; Yu, J., Fabrication of NiS modified CdS nanorod p-n junction photocatalysts with enhanced visible-light photocatalytic H_2-production activity. *Phys. Chem. Chem. Phys.* **2013,** *15* (29), 12088-94.

65. Li, Z. J.; Hofman, E.; Blaker, A.; Davis, A. H.; Dzikovski, B.; Ma, D. K.; Zheng, W., Interface Engineering of Mn-Doped ZnSe-Based Core/Shell Nanowires for Tunable Host-Dopant Coupling. *ACS Nano* **2017,** *11* (12), 12591-12600.

66. Barnard, A. S.; Xu, H.; Li, X.; Pradhan, N.; Peng, X., Modelling the formation of high aspect CdSe quantum wires: axial-growth versus oriented-attachment mechanisms. *Nanotechnology* **2006,** *17* (22), 5707-14.

67. Muckel, F.; Delikanli, S.; Hernandez-Martinez, P. L.; Priesner, T.; Lorenz, S.; Ackermann, J.; Sharma, M.; Demir, H. V.; Bacher, G., sp-d Exchange Interactions in Wave Function Engineered Colloidal CdSe/Mn:CdS Hetero-Nanoplatelets. *Nano Lett* **2018,** *18* (3), 2047-2053.

68. Gerard, C.; Das, R.; Mahadevan, P.; Sarma, D. D., Effective Mass-Driven Structural Transition in a Mn-Doped ZnS Nanoplatelet. *J. Phys. Chem. Lett.* **2013,** *4* (6), 1023-7.

69. Ekimov, A. I., Quantum size effect in three-dimensional microscopic semiconductor crystals. In *JETP Lett.*, **1981**; Vol. 34, p 345.

70. Rossetti, R.; Ellison, J. L.; Gibson, J. M.; Brus, L. E., Size effects in the excited electronic states of small colloidal CdS crystallites. *J.Chem.Phys.* **1984,** *80* (9), 4464-4469.

71. Efros, A. L. E. A. L., Interband absorption of light in a semiconductor sphere. *Sov. Phys. Semicond.* **1981,** *16*, 772-775.

72. Sapra, S.; Shanthi, N.; Sarma, D. D., Realistic Tight Binding Model for the Electronic Structure of II-VI Semiconductors. Cornell University Library, arXiv.org: Ithaca, **2003**.

73. Viswanatha, R.; Sapra, S.; Satpati, B.; Satyam, P. V.; Dev, B. N.; Sarma, D. D., Understanding the quantum size effects in ZnO nanocrystals. *J. Mater Chem.* **2004,** *14* (4).

74. Viswanatha, R.; Sapra, S.; Saha-Dasgupta, T.; Sarma, D. D., Electronic structure of and quantum size effect in III-V and II-VI semiconducting nanocrystals using a realistic tight binding approach. *Phys. Rev. B* **2005,** *72* (4), 045333.

75. Bawendi, M. G.; Carroll, P. J.; Wilson, W. L.; Brus, L. E., Luminescence properties of CdSe quantum crystallites: Resonance between interior and surface localized states. *J. Chem. Phys.* **1992,** *96* (2), 946-954.

76. Brus, L. E., Electron–electron and electron-hole interactions in small semiconductor crystallites: The size dependence of the lowest excited electronic state. *J. Chem. Phys.* **1984,** *80* (9), 4403-4409.

77. Garcia de Arquer, F. P.; Talapin, D. V.; Klimov, V. I.; Arakawa, Y.; Bayer, M.; Sargent, E. H., Semiconductor quantum dots: Technological progress and future challenges. *Science* **2021,** *373* (6555).

78. Smith, A. M.; Nie, S., Semiconductor nanocrystals: structure, properties, and band gap engineering. *Acc. Chem. Res.* **2010,** *43* (2), 190-200.

79. Pu, C.; Qin, H.; Gao, Y.; Zhou, J.; Wang, P.; Peng, X., Synthetic Control of Exciton Behavior in Colloidal Quantum Dots. *J. Am. Chem. Soc.* **2017,** *139* (9), 3302-3311.

80. Rodriguez, H. B.; San Roman, E., Effect of concentration on the photophysics of dyes in light-scattering materials. *Photochem Photobiol* **2013,** *89* (6), 1273-82.

81. de Mello, J. C.; Wittmann, H. F.; Friend, R. H., An improved experimental determination of external photoluminescence quantum efficiency. *Adv. Mater* **1997,** *9* (3), 230-232.

82. Swarnkar, A.; Chulliyil, R.; Ravi, V. K.; Irfanullah, M.; Chowdhury, A.; Nag, A., Colloidal $CsPbBr_3$ Perovskite Nanocrystals: Luminescence beyond Traditional Quantum Dots. *Angew Chem. Int. Ed. Engl.* **2015,** *54* (51), 15424-8.

83. Qu, L.; Peng, X., Control of photoluminescence properties of CdSe nanocrystals in growth. *J. Am. Chem. Soc.* **2002,** *124* (9), 2049-55.

84. Huang, H.; Zhao, F.; Liu, L.; Zhang, F.; Wu, X. G.; Shi, L.; Zou, B.; Pei, Q.; Zhong, H., Emulsion Synthesis of Size-Tunable $CH_3NH_3PbBr_3$ Quantum Dots: An Alternative Route toward Efficient Light-Emitting Diodes. *ACS Appl. Mater Interfaces* **2015,** *7* (51), 28128-33.

85. Peng, Z. A.; Peng, X., Mechanisms of the Shape Evolution of CdSe Nanocrystals. *J. Am. Chem. Soc.* **2001,** *123* (7), 1389-1395.

86. Ninomiya, S.; Adachi, S., Optical properties of wurtzite CdS. *Journal of Applied Physics* **1995,** *78* (2), 1183-1190.

87. Washington, A. L., 2nd; Foley, M. E.; Cheong, S.; Quffa, L.; Breshike, C. J.; Watt, J.; Tilley, R. D.; Strouse, G. F., Ostwald's Rule of Stages and its role in CdSe quantum dot crystallization. *J. Am. Chem. Soc.* **2012,** *134* (41), 17046-52.

88. Harris, C.; Kamat, P. V., Photocatalysis with CdSe nanoparticles in confined media: mapping charge transfer events in the subpicosecond to second timescales. *ACS Nano* **2009,** *3* (3), 682-90.

89. Li, L. S.; Pradhan, N.; Wang, Y.; Peng, X., High Quality ZnSe and ZnS Nanocrystals Formed by Activating Zinc Carboxylate Precursors. *Nano Lett.* **2004,** *4* (11), 2261-2264.

90. Jagtap, S.; Chopade, P.; Tadepalli, S.; Bhalerao, A.; Gosavi, S., A review on the progress of ZnSe as inorganic scintillator. *Opto-Electronics Review* **2019,** *27* (1), 90-103.

91. Peng, X.; Schlamp, M. C.; Kadavanich, A. V.; Alivisatos, A. P., Epitaxial Growth of Highly Luminescent CdSe/CdS Core/Shell Nanocrystals with Photostability and Electronic Accessibility. *J. Am. Chem. Soc.* **1997,** *119* (30), 7019-7029.

92. Liu, X.; Jiang, Y.; Fu, F.; Guo, W.; Huang, W.; Li, L., Facile synthesis of high-quality ZnS, CdS, CdZnS, and CdZnS/ZnS core/shell quantum dots: characterization and diffusion mechanism. *Materials Science in Semiconductor Processing* **2013,** *16* (6), 1723-1729.

93. Brumer, M.; Kigel, A.; Amirav, L.; Sashchiuk, A.; Solomesch, O.; Tessler, N.; Lifshitz, E., PbSe/PbS and PbSe/$PbSe_xS_{1-x}$ Core/Shell Nanocrystals. *Adv. Funct. Mater.* **2005,** *15* (7), 1111-1116.

94. Lv, Y.; Yuan, Y.; Hu, N.; Jin, N.; Xu, D.; Wu, R.; Shen, H.; Chen, O.; Li, L. S., Thick-Shell CdSe/ZnS/CdZnS/ZnS Core/Shell Quantum Dots for Quantitative Immunoassays. *ACS Applied Nano Materials* **2021,** *4* (3), 2855-2865.

95. Chen, X.; Lou, Y.; Samia, A. C.; Burda, C., Coherency Strain Effects on the Optical Response of Core/Shell Heteronanostructures. *Nano Lett* **2003,** *3* (6), 799-803.

96. Wang, Y.; Tang, Z.; Correa-Duarte, M. A.; Pastoriza-Santos, I.; Giersig, M.; Kotov, N. A.; Liz-Marzán, L. M., Mechanism of Strong Luminescence Photoactivation of Citrate-Stabilized Water-Soluble Nanoparticles with CdSe Cores. *J. Phys. Chem. B* **2004,** *108* (40), 15461-15469.

97. Chen, D.; Zhao, F.; Qi, H.; Rutherford, M.; Peng, X., Bright and Stable Purple/Blue Emitting CdS/ZnS Core/Shell Nanocrystals Grown by Thermal Cycling Using a Single-Source Precursor. *Chemistry of Materials* **2010,** *22* (4), 1437-1444.

98. Wang, H.; Xu, L.; Liu, N.; Zhang, R.; Xu, J.; Su, W.; Yu, Y.; Ma, Z.; Li, W.; Chen, K., Enhanced stability and emission intensity of aqueous CdTe/CdS core–shell quantum dots with widely tunable wavelength. *Canadian Journal of Physics* **2014,** *92* (7/8), 802-805.

99. Cristea, M.; Niculescu, E. C., Hydrogenic impurity states in CdSe/ZnS and ZnS/CdSe core-shell nanodots with dielectric mismatch. *The European Physical Journal B* **2012,** *85* (6).

100. Pietryga, J. M.; Werder, D. J.; Williams, D. J.; Casson, J. L.; Schaller, R. D.; Klimov, V. I.; Hollingsworth, J. A., Utilizing the lability of lead selenide to produce heterostructured nanocrystals with bright, stable infrared emission. *J. Am. Chem. Soc.* **2008,** *130* (14), 4879-85.

101. Ivanov, S. A.; Piryatinski, A.; Nanda, J.; Tretiak, S.; Zavadil, K. R.; Wallace, W. O.; Werder, D.; Klimov, V. I., Type-II core/shell CdS/ZnSe nanocrystals: synthesis, electronic structures, and spectroscopic properties. *J. Am. Chem. Soc.* **2007,** *129* (38), 11708-19.

102. Aven, M.; Garwacki, W., Epitaxial Growth and Properties of ZnTe-CdS Heterojunctions. *Journal of The Electrochemical Society* **1963,** *110* (5).

103. McBride, J.; Treadway, J.; Feldman, L. C.; Pennycook, S. J.; Rosenthal, S. J., Structural basis for near unity quantum yield core/shell nanostructures. *Nano Lett* **2006,** *6* (7), 1496-501.

104. Dabbousi, B. O.; RodriguezViejo, J.; Mikulec, F. V.; Heine, J. R.; Mattoussi, H.; Ober, R.; Jensen, K. F.; Bawendi, M. G., (CdSe)ZnS core-shell quantum dots: Synthesis and characterization of a size series of highly luminescent nanocrystallites. *Journal of Physical Chemistry B* **1997,** *101* (46), 9463-9475.

105. Guyot-Sionnest, M. A. H. a. P., Synthesis and Characterization of strongly luminescing ZnS-Capped CdSe nanocrystals. *J. Phys. Chem* **1995,** *100*, 468-471.

106. Li, J. J.; Wang, Y. A.; Guo, W.; Keay, J. C.; Mishima, T. D.; Johnson, M. B.; Peng, X., Large-scale synthesis of nearly monodisperse CdSe/CdS core/shell nanocrystals using air-stable reagents via successive ion layer adsorption and reaction. *J. Am. Chem. Soc.* **2003,** *125* (41), 12567-75.

107. Chen, G.; Zhang, W.; Zhong, X., Single-source precursor route for overcoating CdS and ZnS shells around CdSe core nanocrystals. *Frontiers of Chemistry in China* **2010,** *5* (2), 214-220.

108. Smith, A. M.; Mohs, A. M.; Nie, S., Tuning the optical and electronic properties of colloidal nanocrystals by lattice strain. *Nat Nanotechnol* **2009,** *4* (1), 56-63.

109. Talapin, D. V.; Mekis, I.; Götzinger, S.; Kornowski, A.; Benson, O.; Weller, H., CdSe/CdS/ZnS and CdSe/ZnSe/ZnS Core−Shell−Shell Nanocrystals. *J. Phys. Chem. B* **2004,** *108* (49), 18826-18831.

110. Erwin, S. C.; Zu, L.; Haftel, M. I.; Efros, A. L.; Kennedy, T. A.; Norris, D. J., Doping semiconductor nanocrystals. *Nature* **2005,** *436* (7047), 91-4.

111. Yu, J. H.; Liu, X.; Kweon, K. E.; Joo, J.; Park, J.; Ko, K. T.; Lee, D. W.; Shen, S.; Tivakornsasithorn, K.; Son, J. S.; Park, J. H.; Kim, Y. W.; Hwang, G. S.; Dobrowolska, M.; Furdyna, J. K.; Hyeon, T., Giant Zeeman splitting in nucleation-controlled doped CdSe:Mn^{2+} quantum nanoribbons. *Nat Mater* **2010,** *9* (1), 47-53.

112. Torma, A. J.; Li, W.; Zhang, H.; Tu, Q.; Klepov, V. V.; Brennan, M. C.; McCleese, C. L.; Krzyaniak, M. D.; Wasielewski, M. R.; Katan, C.; Even, J.; Holt, M. V.; Grusenmeyer, T. A.; Jiang, J.; Pachter, R.; Kanatzidis, M. G.; Blancon, J. C.; Mohite, A. D., Interstitial Nature of Mn(2+) Doping in 2D Perovskites. *ACS Nano* **2021,** *15* (12), 20550-20561.

113. Makkar, M.; Dheer, L.; Singh, A.; Moretti, L.; Maiuri, M.; Ghosh, S.; Cerullo, G.; Waghmare, U. V.; Viswanatha, R., Magneto-Optical Stark Effect in Fe-Doped CdS Nanocrystals. *Nano Lett* **2021,** *21* (9), 3798-3804.

114. Shornikova, E. V.; Yakovlev, D. R.; Tolmachev, D. O.; Ivanov, V. Y.; Kalitukha, I. V.; Sapega, V. F.; Kudlacik, D.; Kusrayev, Y. G.; Golovatenko, A. A.; Shendre, S.; Delikanli, S.; Demir, H. V.; Bayer, M., Magneto-Optics of Excitons Interacting with Magnetic Ions in CdSe/CdMnS Colloidal Nanoplatelets. *ACS Nano* **2020,** *14* (7), 9032-9041.

115. Bussian, D. A.; Crooker, S. A.; Yin, M.; Brynda, M.; Efros, A. L.; Klimov, V. I., Tunable magnetic exchange interactions in manganese-doped inverted core-shell ZnSe-CdSe nanocrystals. *Nat. Mater* **2009,** *8* (1), 35-40.

116. Hwang, I. I.; Kim, H.; Kim, J. E.; Park, H. Y.; Lim, H., Solid solubilities of magnetic ions in diluted magnetic semiconductors grown under equilibrium conditions. *Phys. Rev. B Condens Matter* **1994,** *50* (12), 8849-8852.

117. Amit, Y.; Li, Y.; Frenkel, A. I.; Banin, U., From Impurity Doping to Metallic Growth in Diffusion Doping: Properties and Structure of Silver-Doped InAs Nanocrystals. *ACS Nano* **2015,** *9* (11), 10790-800.

118. Schimpf, A. M.; Knowles, K. E.; Carroll, G. M.; Gamelin, D. R., Electronic doping and redox-potential tuning in colloidal semiconductor nanocrystals. *Acc. Chem. Res.* **2015,** *48* (7), 1929-37.

119. Vlaskin, V. A.; Janssen, N.; van Rijssel, J.; Beaulac, R.; Gamelin, D. R., Tunable dual emission in doped semiconductor nanocrystals. *Nano Lett.* **2010,** *10* (9), 3670-4.

120. Liu, N.; Tang, M. L.; Hentschel, M.; Giessen, H.; Alivisatos, A. P., Nanoantenna-enhanced gas sensing in a single tailored nanofocus. *Nat. Mater* **2011,** *10* (8), 631-6.

121. Shanker, G. S.; Tandon, B.; Shibata, T.; Chattopadhyay, S.; Nag, A., Doping Controls Plasmonics, Electrical Conductivity, and Carrier-Mediated Magnetic Coupling in Fe and Sn

Codoped In_2O_3 Nanocrystals: Local Structure Is the Key. *Chemistry of Materials* **2015,** *27* (3), 892-900.

122. Yang, Y.; Chen, O.; Angerhofer, A.; Cao, Y. C., On doping CdS/ZnS core/shell nanocrystals with Mn. *J. Am. Chem. Soc.* **2008,** *130* (46), 15649-61.

123. Chen, H. Y.; Maiti, S.; Son, D. H., Doping location-dependent energy transfer dynamics in Mn-doped CdS/ZnS nanocrystals. *ACS Nano* **2012,** *6* (1), 583-91.

124. Nag, A.; Sarma, D. D., White Light from Mn^{2+}-Doped CdS Nanocrystals: A New Approach. *J. Phys. Chem. C* **2007,** *111* (37), 13641-13644.

125. Bhargava, R. N.; Gallagher, D.; Hong, X.; Nurmikko, A., Optical properties of manganese-doped nanocrystals of ZnS. *Phys. Rev. Lett.* **1994,** *72* (3), 416-419.

126. Bol, A. A.; Meijerink, A., Long-lived Mn^{2+} emission in nanocrystalline ZnS:Mn^{2+}. *Phys. Rev. B* **1998,** *58* (24), 15997-16000.

127. Pandey, A.; Sarma, D. D., Recent Advances in Manganese Doped II-VI Semiconductor Quantum Dots. *Zeitschrift für anorganische und allgemeine Chemie* **2016,** *642* (23), 1331-1339.

128. Dietl, T.; Ohno, H.; Matsukura, F.; Cibert, J.; Ferrand, D., Zener model description of ferromagnetism in zinc-blende magnetic semiconductors. *Science* **2000,** *287* (5455), 1019-22.

129. Fainblat, R.; Frohleiks, J.; Muckel, F.; Yu, J. H.; Yang, J.; Hyeon, T.; Bacher, G., Quantum confinement-controlled exchange coupling in manganese(II)-doped CdSe two-dimensional quantum well nanoribbons. *Nano Lett.* **2012,** *12* (10), 5311-7.

130. Gan, C.; Xiao, M.; Battaglia, D.; Pradhan, N.; Peng, X., Size dependence of nonlinear optical absorption and refraction of Mn-doped ZnSe nanocrystals. *Applied Physics Letters* **2007,** *91* (20).

131. Norberg, N. S.; Kittilstved, K. R.; Amonette, J. E.; Kukkadapu, R. K.; Schwartz, D. A.; Gamelin, D. R., Synthesis of colloidal Mn^{2+}:ZnO quantum dots and high-TC ferromagnetic nanocrystalline thin films. *J. Am. Chem. Soc.* **2004,** *126* (30), 9387-98.

132. Proshchenko, V.; Dahnovsky, Y., Magnetic effects in Mn-doped CdSe nanocrystals. *physica status solidi (b)* **2015,** *252* (10), 2275-2279.

133. Pradhan, N.; Peng, X., Efficient and color-tunable Mn-doped ZnSe nanocrystal emitters: control of optical performance via greener synthetic chemistry. *J. Am. Chem. Soc.* **2007,** *129* (11), 3339-47.

134. Nag, A.; Cherian, R.; Mahadevan, P.; Gopal, A. V.; Hazarika, A.; Mohan, A.; Vengurlekar, A. S.; Sarma, D. D., Size-Dependent Tuning of Mn^{2+} d Emission in Mn^{2+}-Doped CdS Nanocrystals: Bulk vs Surface. *J. Phys. Chem. C* **2010,** *114* (43), 18323-18329.

135. House, G. L.; Drickamer, H. G., High pressure luminescence studies of localized excitations in ZnS doped with Pb^{2+} and Mn^{2+}. *J. Chem. Phys.* **1977,** *67* (7), 3230-3237.

136. Ithurria, S.; Guyot-Sionnest, P.; Mahler, B.; Dubertret, B., Mn^{2+} as a radial pressure gauge in colloidal core/shell nanocrystals. *Phys. Rev. Lett.* **2007,** *99* (26), 265501.

137. Bhattacharjee, A. K.; Pérez-Conde, J., Optical properties of paramagnetic ion-doped semiconductor nanocrystals. *Phys. Rev. B* **2003,** *68* (4).

138. Efros, A. L.; Rashba, E. I.; Rosen, M., Paramagnetic ion-doped nanocrystal as a voltage-controlled spin filter. *Phys. Rev. Lett.* **2001,** *87* (20), 206601.

139. Ochsenbein, S. T.; Feng, Y.; Whitaker, K. M.; Badaeva, E.; Liu, W. K.; Li, X.; Gamelin, D. R., Charge-controlled magnetism in colloidal doped semiconductor nanocrystals. *Nat. Nanotechnol* **2009,** *4* (10), 681-7.

140. Liu, W. K.; Whitaker, K. M.; Kittilstved, K. R.; Gamelin, D. R., Stable photogenerated carriers in magnetic semiconductor nanocrystals. *J. Am. Chem. Soc.* **2006,** *128* (12), 3910-1.

141. Buonsanti, R.; Milliron, D. J., Chemistry of Doped Colloidal Nanocrystals. *Chemistry of Materials* **2013,** *25* (8), 1305-1317.

142. Zheng, W.; Singh, K.; Wang, Z.; Wright, J. T.; van Tol, J.; Dalal, N. S.; Meulenberg, R. W.; Strouse, G. F., Evidence of a $ZnCr_2Se_4$ spinel inclusion at the core of a Cr-doped ZnSe quantum dot. *J. Am. Chem. Soc.* **2012,** *134* (12), 5577-85.

143. Hanif, K. M.; Meulenberg, R. W.; Strouse, G. F., Magnetic ordering in doped Cd(1-x)Co(x)Se diluted magnetic quantum dots. *J. Am. Chem. Soc.* **2002,** *124* (38), 11495-502.

144. Zheng, W.; Strouse, G. F., Involvement of carriers in the size-dependent magnetic exchange for Mn:CdSe quantum dots. *J. Am. Chem. Soc.* **2011,** *133* (19), 7482-9.

145. Saha, A.; Makkar, M.; Shetty, A.; Gahlot, K.; A, R. P.; Viswanatha, R., Diffusion doping in quantum dots: bond strength and diffusivity. *Nanoscale* **2017,** *9* (8), 2806-2813.

146. Archer, P. I.; Santangelo, S. A.; Gamelin, D. R., Inorganic cluster syntheses of TM^{2+}-doped quantum dots (CdSe, CdS, CdSe/CdS): physical property dependence on dopant locale. *J. Am. Chem. Soc.* **2007,** *129* (31), 9808-18.

147. Yang, Y.; Chen, O.; Angerhofer, A.; Cao, Y. C., Radial-position-controlled doping of CdS/ZnS core/shell nanocrystals: surface effects and position-dependent properties. *Chemistry* **2009,** *15* (13), 3186-97.

148. Acharya, S.; Sarkar, S.; Pradhan, N., Material Diffusion and Doping of Mn in Wurtzite ZnSe Nanorods. *J. Phys. Chem. C* **2013,** *117* (11), 6006-6012.

149. Rivest, J. B.; Jain, P. K., Cation exchange on the nanoscale: an emerging technique for new material synthesis, device fabrication, and chemical sensing. *Chem. Soc. Rev.* **2013,** *42* (1), 89-96.

150. Beberwyck, B. J.; Surendranath, Y.; Alivisatos, A. P., Cation Exchange: A Versatile Tool for Nanomaterials Synthesis. *J. Phys. Chem. C* **2013,** *117* (39), 19759-19770.

151. Zu, L.; Norris, D. J.; Kennedy, T. A.; Erwin, S. C.; Efros, A. L., Impact of ripening on manganese-doped ZnSe nanocrystals. *Nano Lett.* **2006,** *6* (2), 334-40.

152. Buonsanti, R.; Llordes, A.; Aloni, S.; Helms, B. A.; Milliron, D. J., Tunable infrared absorption and visible transparency of colloidal aluminum-doped zinc oxide nanocrystals. *Nano Lett.* **2011,** *11* (11), 4706-10.

153. Dasgupta, N. P.; Neubert, S.; Lee, W.; Trejo, O.; Lee, J.-R.; Prinz, F. B., Atomic Layer Deposition of Al-doped ZnO Films: Effect of Grain Orientation on Conductivity. *Chemistry of Materials* **2010,** *22* (16), 4769-4775.

154. Sapra, S.; Sarma, D. D., Simultaneous control of nanocrystal size and nanocrystal-nanocrystal separation in CdS nanocrystal assembly. *Pramana-J Phys* **2005,** *65* (4), 565-570.

155. Acebron, M.; Galisteo-Lopez, J. F.; Lopez, C.; Herrera, F. C.; Mizrahi, M.; Requejo, F. G.; Palomares, F. J.; Juarez, B. H., Unexpected Optical Blue Shift in Large Colloidal Quantum Dots by Anionic Migration and Exchange. *J. Phys. Chem. Lett.* **2018,** *9* (11), 3124-3130.

156. Li, Y.; Frenkel, A. I., Deciphering the Local Environment of Single-Atom Catalysts with X-ray Absorption Spectroscopy. *Acc. Chem. Res.* **2021,** *54* (11), 2660-2669.

157. Moreau, L. M.; Ha, D. H.; Bealing, C. R.; Zhang, H.; Hennig, R. G.; Robinson, R. D., Unintended phosphorus doping of nickel nanoparticles during synthesis with TOP: a discovery through structural analysis. *Nano Lett.* **2012,** *12* (9), 4530-9.

158. Cooper, J. K.; Gul, S.; Lindley, S. A.; Yano, J.; Zhang, J. Z., Tunable Photoluminescent Core/Shell Cu(+)-Doped ZnSe/ZnS Quantum Dots Codoped with Al(3+), Ga(3+), or In(3+). *ACS Appl Mater Interfaces* **2015,** *7* (18), 10055-66.

159. Chakraborty, S.; Grandhi, G. K.; Viswanatha, R., Study of the Interface and Radial Dopant Position in Semiconductor Heterostructures Using X-ray Absorption Spectroscopy. *J. Phys. Chem. Lett.* **2022,** *13* (47), 11036-11043.

160. Groeneveld, E.; Witteman, L.; Lefferts, M.; Ke, X.; Bals, S.; Van Tendeloo, G.; Donega Cde, M., Tailoring ZnSe-CdSe colloidal quantum dots via cation exchange: from core/shell to alloy nanocrystals. *ACS Nano* **2013,** *7* (9), 7913-30.

161. Bailey, R. E.; Nie, S., Alloyed semiconductor quantum dots: tuning the optical properties without changing the particle size. *J. Am. Chem. Soc.* **2003,** *125* (23), 7100-6.

162. Gadiyar, C.; Loiudice, A.; D'Ambra, F.; Oveisi, E.; Stoian, D.; Iyengar, P.; Castilla-Amoros, L.; Mantella, V.; Buonsanti, R., Nanocrystals as Precursors in Solid-State Reactions for Size- and Shape-Controlled Polyelemental Nanomaterials. *J. Am. Chem. Soc.* **2020,** *142* (37), 15931-15940.

163. Smith, D., McCartney, M., Microscopy | Semiconductors. *Encyclopedia of Analytical Science* **2013**, 89-97.

164. Verbeeck, J.; Hens, S.; Potapov, P.; Schryvers, D., ELECTRON ENERGY LOSS SPECTROMETRY. In *Encyclopedia of Analytical Science (Second Edition)*, Worsfold, P.; Townshend, A.; Poole, C., Eds. Elsevier: Oxford, **2005**; pp 324-331.

165. Counio, G.; Gacoin, T.; Boilot, J. P., Synthesis and photoluminescence of $Cd_{1-x}Mn_xS$ (x <= 5%) nanocrystals. *Journal of Physical Chemistry B* **1998,** *102* (27), 5257-5260.

166. Wang, Z.; Zheng, W.; van Tol, J.; Dalal, N. S.; Strouse, G. F., High-field electron paramagnetic resonance as a microscopic probe of anisotropic strain at Mn^{2+} sites in CdSe:Mn^{2+} quantum dots. *Chemical Physics Letters* **2012,** *524*, 73-77.

167. Dorain, P. B., Electron Paramagnetic Resonance of Manganese (II) in Hexagonal Zinc Oxide and Cadmium Sulfide Single Crystals. *Phys. Rev.* **1958,** *112* (4), 1058-1060.

168. Title, R. S., Covalency and the Paramagnetic Resonance of Mn^{++}in CdSe. *Phys. Rev.* **1963,** *130* (1), 17-19.

169. Keller, S. P.; Gelles, I. L.; Smith, W. V., Paramagnetic Resonance Absorption in Mn-Activated Hexagonal ZnS. *Phys. Rev.* **1958,** *110* (4), 850-855.

170. Kennedy, T. A.; Glaser, E. R.; Klein, P. B.; Bhargava, R. N., Symmetry and electronic structure of the Mn impurity in ZnS nanocrystals. *Phys. Rev. B Condens Matter* **1995,** *52* (20), 14356-14359.

171. Lad, A. D.; Rajesh, C.; Khan, M.; Ali, N.; Gopalakrishnan, I. K.; Kulshreshtha, S. K.; Mahamuni, S., Magnetic behavior of manganese-doped ZnSe quantum dots. *Journal of Applied Physics* **2007,** *101* (10).

172. Matumura, O., Electron Spin Resonance of Mn-activated Phosphors. *Journal of the Physical Society of Japan* **1959,** *14* (1), 108-108.

173. Mikulec, F. V.; Kuno, M.; Bennati, M.; Hall, D. A.; Griffin, R. G.; Bawendi, M. G., Organometallic Synthesis and Spectroscopic Characterization of Manganese-Doped CdSe Nanocrystals. *J. Am. Chem. Soc.* **2000,** *122* (11), 2532-2540.

174. Nag, A.; Sapra, S.; Nagamani, C.; Sharma, A.; Pradhan, N.; Bhat, S. V.; Sarma, D. D., A Study of Mn^{2+} Doping in CdS Nanocrystals. *Chemistry of Materials* **2007,** *19* (13), 3252-3259.

175. Sabir, N.; Qayyum, W.; Ali, F.; Ameen, F.; Parak, W. J.; Osiński, M., Optical study of the transition metals (M=Cr, Mn, Co, Ni, Cu) doped M-CdS/ZnS core/shell nanoparticles. In *Colloidal Nanoparticles for Biomedical Applications XIV*, 2019.

176. Chamarro, M. A.; Voliotis, V.; Grousson, R.; Lavallard, P.; Gacoin, T.; Counio, G.; Boilot, J. P.; Cases, R., Optical properties of Mn-doped CdS nanocrystals. *Journal of Crystal Growth* **1996,** *159* (1-4), 853-856.

177. Stroyuk, O.; Raevskaya, A.; Gaponik, N.; Selyshchev, O.; Dzhagan, V.; Schulze, S.; Zahn, D. R. T., Origin of the Broadband Photoluminescence of Pristine and Cu^+/Ag^+-Doped Ultrasmall CdS and CdSe/CdS Quantum Dots. *J. Phys. Chem. C* **2018,** *122* (18), 10267-10277.

178. Nag, A.; Chakraborty, S.; Sarma, D. D., To dope Mn^{2+} in a semiconducting nanocrystal. *J. Am. Chem. Soc.* **2008,** *130* (32), 10605-11.

179. Chen, D.; Viswanatha, R.; Ong, G. L.; Xie, R.; Balasubramaninan, M.; Peng, X., Temperature dependence of "elementary processes" in doping semiconductor nanocrystals. *J. Am. Chem. Soc.* **2009,** *131* (26), 9333-9.

180. Suyver, J. F.; Wuister, S. F.; Kelly, J. J.; Meijerink, A., Luminescence of nanocrystalline ZnSe:Mn^{2+}. *Physical Chemistry Chemical Physics* **2000,** *2* (23), 5445-5448.

181. Barrows, C. J.; Chakraborty, P.; Kornowske, L. M.; Gamelin, D. R., Tuning Equilibrium Compositions in Colloidal $Cd_{1-x}Mn_xSe$ Nanocrystals Using Diffusion Doping and Cation Exchange. *ACS Nano* **2016,** *10* (1), 910-8.

182. Son, D. H.; Hughes, S. M.; Yin, Y.; Paul Alivisatos, A., Cation exchange reactions in ionic nanocrystals. *Science* **2004,** *306* (5698), 1009-12.

183. De Trizio, L.; Manna, L., Forging Colloidal Nanostructures via Cation Exchange Reactions. *Chem. Rev.* **2016,** *116* (18), 10852-87.

184. Petralanda, U.; De Trizio, L.; Gariano, G.; Cingolani, R.; Manna, L.; Artyukhin, S., Triggering Cation Exchange Reactions by Doping. *J. Phys. Chem. Lett.* **2018,** *9* (17), 4895-4900.

185. Makkar, M.; Saha, A.; Khalid, S.; Viswanatha, R., Thermodynamics of Dual Doping in Quantum Dots. *J. Phys. Chem. Lett.* **2019,** *10* (8), 1992-1998.

186. Bothe, C.; Kornowski, A.; Tornatzky, H.; Schmidtke, C.; Lange, H.; Maultzsch, J.; Weller, H., Solid-State Chemistry on the Nanoscale: Ion Transport through Interstitial Sites or Vacancies? *Angew Chem. Int. Ed. Engl.* **2015,** *54* (47), 14183-6.

187. Jamil, N. Y.; Shaw, D., The Diffusion of Mn in Cdte. *Semiconductor Science and Technology* **1995,** *10* (7), 952-958.

188. Zunger, A.; Malyi, O. I., Understanding Doping of Quantum Materials. *Chem. Rev.* **2021,** *121* (5), 3031-3060.

189. Mokari, T.; Aharoni, A.; Popov, I.; Banin, U., Diffusion of gold into InAs nanocrystals. *Angew Chem. Int. Ed. Engl.* **2006,** *45* (47), 8001-5.

190. Rehman, S.; Hafeez, M.; Manzoor, U.; Khan, M. A.; Bhatti, A. S., Competitive role of Mn diffusion with growth in Mn catalyzed nanostructures. *Journal of Applied Physics* **2012,** *111* (8).

191. Prusty, G.; Guria, A. K.; Patra, B. K.; Pradhan, N., Diffusion-Induced Shape Evolution in Multinary Semiconductor Nanostructures. *J. Phys. Chem. Lett.* **2015,** *6* (13), 2421-6.

192. Chen, J.; Jiang, F.; Yin, Y., Manipulation of Interfacial Diffusion for Controlling Nanoscale Transformation. *Acc. Chem. Res.* **2021,** *54* (5), 1168-1177.

193. Pietra, F.; De Trizio, L.; Hoekstra, A. W.; Renaud, N.; Prato, M.; Grozema, F. C.; Baesjou, P. J.; Koole, R.; Manna, L.; Houtepen, A. J., Tuning the Lattice Parameter of In_xZn_yP for Highly Luminescent Lattice-Matched Core/Shell Quantum Dots. *ACS Nano* **2016,** *10* (4), 4754-62.

194. Lesnyak, V.; Brescia, R.; Messina, G. C.; Manna, L., Cu Vacancies Boost Cation Exchange Reactions in Copper Selenide Nanocrystals. *J. Am. Chem. Soc.* **2015,** *137* (29), 9315-23.

195. Ravi, V. K.; Saikia, S.; Yadav, S.; Nawale, V. V.; Nag, A., $CsPbBr_3$/ZnS Core/Shell Type Nanocrystals for Enhancing Luminescence Lifetime and Water Stability. *Acs Energy Letters* **2020,** *5* (6), 1794-1796.

196. Zhang, X.; Zhang, J.; Phuyal, D.; Du, J.; Tian, L.; Öberg, V. A.; Johansson, M. B.; Cappel, U. B.; Karis, O.; Liu, J.; Rensmo, H.; Boschloo, G.; Johansson, E. M. J., Inorganic $CsPbI_3$ Perovskite Coating on PbS Quantum Dot for Highly Efficient and Stable Infrared Light Converting Solar Cells. *Advanced Energy Materials* **2017,** *8* (6).

197. Wan, X.; Pan, Y.; Xu, Y.; Liu, J.; Chen, H.; Pan, R.; Zhao, Y.; Su, P.; Li, Y.; Zhang, X.; Zhang, S.; Li, H.; Su, D.; Weng, Y.; Zhang, J., Ultralong Lifetime of Plasmon-Excited Electrons Realized in Nonepitaxial/Epitaxial Au@CdS/CsPbBr(3) Triple-Heteronanocrystals. *Adv. Mater* **2023,** *35* (3), e2207555.

198. Xu, X.; Wang, X., Perovskite Nano-Heterojunctions: Synthesis, Structures, Properties, Challenges, and Prospects. *Small Structures* **2020,** *1* (1).

199. Yost, A. J.; Pimachev, A.; Rimal, G.; Tang, J.; Dahnovsky, Y.; Chien, T., Effects of Mn dopant locations on the electronic bandgap of PbS quantum dots. *Applied Physics Letters* **2017,** *111* (23).

200. Norris, D. J.; Efros, A. L.; Erwin, S. C., Doped nanocrystals. *Science* **2008,** *319* (5871), 1776-9.

201. Hewavitharana, I. K.; Brock, S. L., When Ligand Exchange Leads to Ion Exchange: Nanocrystal Facets Dictate the Outcome. *ACS Nano* **2017,** *11* (11), 11217-11224.

202. Grandhi, G. K.; M, A.; Viswanatha, R., Understanding the Role of Surface Capping Ligands in Passivating the Quantum Dots Using Copper Dopants as Internal Sensor. *J. Phys. Chem. C* **2016,** *120* (35), 19785-19795.

203. Cao, Y. C., Materials science. Impurities enhance semiconductor nanocrystal performance. *Science* **2011,** *332* (6025), 48-9.

204. Mocatta, D.; Cohen, G.; Schattner, J.; Millo, O.; Rabani, E.; Banin, U., Heavily doped semiconductor nanocrystal quantum dots. *Science* **2011,** *332* (6025), 77-81.

205. Zuo, T.; Sun, Z.; Zhao, Y.; Jiang, X.; Gao, X., The big red shift of photoluminescence of Mn dopants in strained CdS: a case study of Mn-doped MnS-CdS heteronanostructures. *J. Am. Chem. Soc.* **2010,** *132* (19), 6618-9.

206. Bear, J. C.; Hollingsworth, N.; McNaughter, P. D.; Mayes, A. G.; Ward, M. B.; Nann, T.; Hogarth, G.; Parkin, I. P., Copper-doped CdSe/ZnS quantum dots: controllable photoactivated copper(I) cation storage and release vectors for catalysis. *Angew Chem. Int. Ed. Engl.* **2014,** *53* (6), 1598-601.

207. Beaulac, R.; Schneider, L.; Archer, P. I.; Bacher, G.; Gamelin, D. R., Light-induced spontaneous magnetization in doped colloidal quantum dots. *Science* **2009,** *325* (5943), 973-6.

208. Pradhan, N.; Das Adhikari, S.; Nag, A.; Sarma, D. D., Luminescence, Plasmonic, and Magnetic Properties of Doped Semiconductor Nanocrystals. *Angew Chem. Int. Ed. Engl.* **2017,** *56* (25), 7038-7054.

209. Zheng, W.; Kumar, P.; Washington, A.; Wang, Z.; Dalal, N. S.; Strouse, G. F.; Singh, K., Quantum phase transition from superparamagnetic to quantum superparamagnetic state in ultrasmall Cd(1-x)Cr(II)(x)Se quantum dots? *J. Am. Chem. Soc.* **2012,** *134* (4), 2172-9.

210. Kittilstved, K. R.; Gamelin, D. R., Activation of high-T(C) ferromagnetism in Mn^{2+}-doped ZnO using amines. *J. Am. Chem. Soc.* **2005,** *127* (15), 5292-3.

211. Pu, C.; Ma, J.; Qin, H.; Yan, M.; Fu, T.; Niu, Y.; Yang, X.; Huang, Y.; Zhao, F.; Peng, X., Doped Semiconductor-Nanocrystal Emitters with Optimal Photoluminescence Decay Dynamics in Microsecond to Millisecond Range: Synthesis and Applications. *ACS Cent Sci* **2016,** *2* (1), 32-9.

212. Beaulac, R.; Ochsenbein, S.; Gamelin, D., Colloidal Transition-Metal-Doped Quantum Dots. In *Nanocrystal Quantum Dots, Second Edition*, CRC Press: **2010**; pp 397-453.

213. Beaulac, R.; Archer, P. I.; Gamelin, D. R., Luminescence in colloidal Mn^{2+}-doped semiconductor nanocrystals. *Journal of Solid State Chemistry* **2008,** *181* (7), 1582-1589.

214. Beaulac, R.; Archer, P. I.; Ochsenbein, S. T.; Gamelin, D. R., Mn^{2+}-Doped CdSe Quantum Dots: New Inorganic Materials for Spin-Electronics and Spin-Photonics. *Advanced Functional Materials* **2008,** *18* (24), 3873-3891.

215. Dalpian, G. M.; Chelikowsky, J. R., Self-purification in semiconductor nanocrystals. *Phys. Rev. Lett.* **2006,** *96* (22), 226802.

216. Zhao, H.; Zhu, Y.; Ye, H.; He, Y.; Li, H.; Sun, Y.; Yang, F.; Wang, R., Atomic-Scale Structure Dynamics of Nanocrystals Revealed By In Situ and Environmental Transmission Electron Microscopy. *Adv. Mater* **2022**, e2206911.

217. Wu, S.; Luo, T.; Kou, Z.; Tang, S.; Yan, M.; Wang, J.; Fu, S.; Ying, H.; Liu, S.; Wilde, G.; Lai, Q.; Lan, S.; Feng, T., Origin of strain softening in a nanograined Al alloy. *Scripta Materialia* **2023,** *226*.

218. Cheng, Y.; Xie, Y.; Liu, Z.; Yan, S.; Ma, Y.; Yue, Y.; Wang, J.; Gao, Y.; Li, L., Maximizing Electron Channels Enabled by MXene Aerogel for High-Performance Self-Healable Flexible Electronic Skin. *ACS Nano* **2023**.

219. Denton, A. R.; Ashcroft, N. W., Vegard's law. *Phys. Rev. A* **1991,** *43* (6), 3161-3164.

220. Rémi Beaulac, S. T. O., and Daniel R. Gamelin, Colloidal TransitionMetal-Doped quantum dots. *CRC Press* **2010**, 58.

221. Shannon, R. D., Revised effective ionic radii and systematic studies of interatomic distances in halides and chalcogenides. *Acta Crystallographica Section A* **1976,** *32* (5), 751-767.

222. Dabbousi, B. O.; Rodriguez-Viejo, J.; Mikulec, F. V.; Heine, J. R.; Mattoussi, H.; Ober, R.; Jensen, K. F.; Bawendi, M. G., (CdSe)ZnS Core−Shell Quantum Dots: Synthesis and Characterization of a Size Series of Highly Luminescent Nanocrystallites. *J. Phys. Chem. B* **1997,** *101* (46), 9463-9475.

223. Chung, J. H.; Ah, C. S.; Jang, D.-J., Formation and Distinctive Decay Times of Surface- and Lattice-Bound Mn^{2+} Impurity Luminescence in ZnS Nanoparticles. *J. Phys. Chem. B* **2001,** *105* (19), 4128-4132.

224. Sobhanan, J.; Rival, J. V.; Anas, A.; Sidharth Shibu, E.; Takano, Y.; Biju, V., Luminescent quantum dots: Synthesis, optical properties, bioimaging and toxicity. *Adv. Drug Deliv. Rev.* **2023,** *197*, 114830.

225. Hsueh-Shih, C.; Cheng-Kuo, H.; Hsin-Yen, H., InGaN-CdSe-ZnSe quantum dots white LEDs. *IEEE Photonics Technology Letters* **2006,** *18* (1), 193-195.

226. Grandhi, G. K.; Tomar, R.; Viswanatha, R., Study of surface and bulk electronic structure of II-VI semiconductor nanocrystals using Cu as a nanosensor. *ACS Nano* **2012,** *6* (11), 9751-63.

227. Bonanni, A.; Dietl, T., A story of high-temperature ferromagnetism in semiconductors. *Chem. Soc. Rev.* **2010,** *39* (2), 528-39.

228. Viswanatha, R.; Naveh, D.; Chelikowsky, J. R.; Kronik, L.; Sarma, D. D., Magnetic Properties of Fe/Cu Codoped ZnO Nanocrystals. *J. Phys. Chem. Lett.* **2012,** *3* (15), 2009-2014.

229. Sahu, A.; Kang, M. S.; Kompch, A.; Notthoff, C.; Wills, A. W.; Deng, D.; Winterer, M.; Frisbie, C. D.; Norris, D. J., Electronic impurity doping in CdSe nanocrystals. *Nano Lett.* **2012,** *12* (5), 2587-94.

230. Grandhi, G. K.; Swathi, K.; Narayan, K. S.; Viswanatha, R., Cu Doping in Ligand Free CdS Nanocrystals: Conductivity and Electronic Structure Study. *J. Phys. Chem. Lett.* **2014,** *5* (13), 2382-9.

231. Fueno, T., *Transition State: A Theoretical Approach*. CRC Press: Netherlands, **2019**.

232. Wenk, H. R.; Bulakh, A., *Minerals: Their Constitution and Origin*. Cambridge University Press: **2004**.

233. Møller, C. K., Crystal structure and photoconductivity of caesium plumbohalides. *Nature* **1958,** *182* (4647), 1436-1436.

234. Goldschmidt, V., Crystal structure and chemical constitution. *Transactions of the Faraday Society* **1929,** *25*, 253-283.

235. Stoumpos, C. C.; Kanatzidis, M. G., The Renaissance of Halide Perovskites and Their Evolution as Emerging Semiconductors. *Acc. Chem. Res.* **2015,** *48* (10), 2791-2802.

236. Gratzel, M., The light and shade of perovskite solar cells. *Nat. Mater.* **2014,** *13* (9), 838-42.

237. Green, M. A.; Ho-Baillie, A.; Snaith, H. J., The emergence of perovskite solar cells. *Nature Photonics* **2014,** *8* (7), 506-514.

238. Nedelcu, G.; Protesescu, L.; Yakunin, S.; Bodnarchuk, M. I.; Grotevent, M. J.; Kovalenko, M. V., Fast Anion-Exchange in Highly Luminescent Nanocrystals of Cesium Lead Halide Perovskites ($CsPbX_3$, X = Cl, Br, I). *Nano Lett.* **2015,** *15* (8), 5635-40.

239. Protesescu, L.; Yakunin, S.; Bodnarchuk, M. I.; Krieg, F.; Caputo, R.; Hendon, C. H.; Yang, R. X.; Walsh, A.; Kovalenko, M. V., Nanocrystals of Cesium Lead Halide Perovskites (CsPbX(3), X = Cl, Br, and I): Novel Optoelectronic Materials Showing Bright Emission with Wide Color Gamut. *Nano Lett.* **2015,** *15* (6), 3692-6.

240. Dutta, A.; Behera, R. K.; Pal, P.; Baitalik, S.; Pradhan, N., Near-Unity Photoluminescence Quantum Efficiency for All CsPbX(3) (X=Cl, Br, and I) Perovskite Nanocrystals: A Generic Synthesis Approach. *Angew Chem. Int. Ed. Engl.* **2019,** *58* (17), 5552-5556.

241. Becker, M. A.; Vaxenburg, R.; Nedelcu, G.; Sercel, P. C.; Shabaev, A.; Mehl, M. J.; Michopoulos, J. G.; Lambrakos, S. G.; Bernstein, N.; Lyons, J. L.; Stoferle, T.; Mahrt, R. F.; Kovalenko, M. V.; Norris, D. J.; Raino, G.; Efros, A. L., Bright triplet excitons in caesium lead halide perovskites. *Nature* **2018,** *553* (7687), 189-193.

242. Raino, G.; Becker, M. A.; Bodnarchuk, M. I.; Mahrt, R. F.; Kovalenko, M. V.; Stoferle, T., Superfluorescence from lead halide perovskite quantum dot superlattices. *Nature* **2018,** *563* (7733), 671-675.

243. Swarnkar, A.; Marshall, A. R.; Sanehira, E. M.; Chernomordik, B. D.; Moore, D. T.; Christians, J. A.; Chakrabarti, T.; Luther, J. M., Quantum dot-induced phase stabilization of alpha-$CsPbI_3$ perovskite for high-efficiency photovoltaics. *Science* **2016,** *354* (6308), 92-95.

244. Thomas, C. J.; Zhang, Y.; Guillaussier, A.; Bdeir, K.; Aly, O. F.; Kim, H. G.; Noh, J.; Reimnitz, L. C.; Li, J.; Deepak, F. L.; Smilgies, D.-M.; Milliron, D. J.; Korgel, B. A., Thermal Stability of the Black Perovskite Phase in Cesium Lead Iodide Nanocrystals Under Humid Conditions. *Chemistry of Materials* **2019,** *31* (23), 9750-9758.

245. Zhang, Y.; Siegler, T. D.; Thomas, C. J.; Abney, M. K.; Shah, T.; De Gorostiza, A.; Greene, R. M.; Korgel, B. A., A “Tips and Tricks” Practical Guide to the Synthesis of Metal Halide Perovskite Nanocrystals. *Chemistry of Materials* **2020,** *32* (13), 5410-5423.

246. Chen, Y.; Liu, X.; Wang, T.; Zhao, Y., Highly Stable Inorganic Lead Halide Perovskite toward Efficient Photovoltaics. *Acc. Chem. Res.* **2021,** *54* (17), 3452-3461.

247. Chen, Y.; Zhao, Y., Incorporating quantum dots for high efficiency and stable perovskite photovoltaics. *Journal of Materials Chemistry A* **2020,** *8* (47), 25017-25027.

248. Stroyuk, O., Lead-free hybrid perovskites for photovoltaics. *Beilstein J Nanotechnol* **2018,** *9*, 2209-2235.

249. Tan, Z.-K.; Moghaddam, R. S.; Lai, M. L.; Docampo, P.; Higler, R.; Deschler, F.; Price, M.; Sadhanala, A.; Pazos, L. M.; Credgington, D.; Hanusch, F.; Bein, T.; Snaith, H. J.; Friend, R. H., Bright light-emitting diodes based on organometal halide perovskite. *Nature Nanotechnology* **2014,** *9* (9), 687-692.

250. Shen, Y.; Zhou, J.; Li, Y.; Tang, J.-X., Strategies to Improve the Stability of Perovskite Light-Emitting Diodes: Progress and Perspective. *J. Phys. Chem. Lett.* **2022,** *13* (29), 6806-6819.

251. Wu, H.; Xu, S.; Shao, H.; Li, L.; Cui, Y.; Wang, C., Single component Mn-doped perovskite-related $CsPb_2Cl_xBr_{5-x}$ nanoplatelets with a record white light quantum yield of 49%: a new single layer color conversion material for light-emitting diodes. *Nanoscale* **2017,** *9* (43), 16858-16863.

252. Zhu, H.; Fu, Y.; Meng, F.; Wu, X.; Gong, Z.; Ding, Q.; Gustafsson, M. V.; Trinh, M. T.; Jin, S.; Zhu, X. Y., Lead halide perovskite nanowire lasers with low lasing thresholds and high quality factors. *Nature Materials* **2015,** *14* (6), 636-642.

253. Xing, G.; Mathews, N.; Lim, S. S.; Yantara, N.; Liu, X.; Sabba, D.; Grätzel, M.; Mhaisalkar, S.; Sum, T. C., Low-temperature solution-processed wavelength-tunable perovskites for lasing. *Nature Materials* **2014,** *13* (5), 476-480.

254. Sutherland, B. R.; Hoogland, S.; Adachi, M. M.; Wong, C. T. O.; Sargent, E. H., Conformal Organohalide Perovskites Enable Lasing on Spherical Resonators. *ACS Nano* **2014,** *8* (10), 10947-10952.

255. Wang, F.; Cao, Y.; Chen, C.; Chen, Q.; Wu, X.; Li, X.; Qin, T.; Huang, W., Materials toward the Upscaling of Perovskite Solar Cells: Progress, Challenges, and Strategies. *Advanced Functional Materials* **2018,** *28* (52).

256. Han, Q.; Hsieh, Y. T.; Meng, L.; Wu, J. L.; Sun, P.; Yao, E. P.; Chang, S. Y.; Bae, S. H.; Kato, T.; Bermudez, V.; Yang, Y., High-performance perovskite/Cu(In,Ga)Se(2) monolithic tandem solar cells. *Science* **2018,** *361* (6405), 904-908.

257. Dou, L.; Yang, Y. M.; You, J.; Hong, Z.; Chang, W. H.; Li, G.; Yang, Y., Solution-processed hybrid perovskite photodetectors with high detectivity. *Nat. Commun.* **2014,** *5*, 5404.

258. Lee, M. M.; Teuscher, J.; Miyasaka, T.; Murakami, T. N.; Snaith, H. J., Efficient hybrid solar cells based on meso-superstructured organometal halide perovskites. *Science* **2012,** *338* (6107), 643-7.

259. Karna, L. R.; Upadhyay, R.; Ghosh, A., All-inorganic perovskite photovoltaics for power conversion efficiency of 31. *Sci. Rep.* **2023,** *13* (1), 15212.

260. Norris, D. J.; Yao, N.; Charnock, F. T.; Kennedy, T. A., High-Quality Manganese-Doped ZnSe Nanocrystals. *Nano Lett.* **2001,** *1* (1), 3-7.

261. Nelson, H. D.; Bradshaw, L. R.; Barrows, C. J.; Vlaskin, V. A.; Gamelin, D. R., Picosecond Dynamics of Excitonic Magnetic Polarons in Colloidal Diffusion-Doped $Cd_{1-x}Mn_xSe$ Quantum Dots. *ACS Nano* **2015,** *9* (11), 11177-11191.

262. Pradhan, N.; Goorskey, D.; Thessing, J.; Peng, X., An Alternative of CdSe Nanocrystal Emitters: Pure and Tunable Impurity Emissions in ZnSe Nanocrystals. *J. Am. Chem. Soc.* **2005,** *127* (50), 17586-17587.

263. Erickson, C. S.; Bradshaw, L. R.; McDowall, S.; Gilbertson, J. D.; Gamelin, D. R.; Patrick, D. L., Zero-Reabsorption Doped-Nanocrystal Luminescent Solar Concentrators. *ACS Nano* **2014,** *8* (4), 3461-3467.

264. Guria, A. K.; Dutta, S. K.; Adhikari, S. D.; Pradhan, N., Doping Mn^{2+} in Lead Halide Perovskite Nanocrystals: Successes and Challenges. *ACS Energy Letters* **2017,** *2* (5), 1014-1021.

265. Parobek, D.; Dong, Y.; Qiao, T.; Son, D. H., Direct Hot-Injection Synthesis of Mn-Doped $CsPbBr_3$ Nanocrystals. *Chemistry of Materials* **2018,** *30* (9), 2939-2944.

266. Udayabhaskararao, T.; Kazes, M.; Houben, L.; Lin, H.; Oron, D., Nucleation, Growth, and Structural Transformations of Perovskite Nanocrystals. *Chemistry of Materials* **2017,** *29* (3), 1302-1308.

267. Dutta, A.; Dutta, S. K.; Das Adhikari, S.; Pradhan, N., Phase-Stable CsPbI3 Nanocrystals: The Reaction Temperature Matters. *Angew Chem. Int. Ed. Engl.* **2018,** *57* (29), 9083-9087.

268. Stoumpos, C. C.; Malliakas, C. D.; Peters, J. A.; Liu, Z.; Sebastian, M.; Im, J.; Chasapis, T. C.; Wibowo, A. C.; Chung, D. Y.; Freeman, A. J.; Wessels, B. W.; Kanatzidis, M. G., Crystal Growth of the Perovskite Semiconductor $CsPbBr_3$: A New Material for High-Energy Radiation Detection. *Crystal Growth & Design* **2013,** *13* (7), 2722-2727.

269. Grim, J. Q.; Manna, L.; Moreels, I., A sustainable future for photonic colloidal nanocrystals. *Chem. Soc. Rev.* **2015,** *44* (16), 5897-914.

270. Davis, A. H.; Li, S.; Lin, H.; Chu, C.; Franck, J. M.; Leem, G.; Maye, M. M.; Zheng, W., Ligand-mediated synthesis of chemically tailored two-dimensional all-inorganic perovskite nanoplatelets under ambient conditions. *Journal of Materials Chemistry C* **2021,** *9* (40), 14226-14235.

271. Akbulatov, A. F.; Frolova, L. A.; Dremova, N. N.; Zhidkov, I.; Martynenko, V. M.; Tsarev, S. A.; Luchkin, S. Y.; Kurmaev, E. Z.; Aldoshin, S. M.; Stevenson, K. J.; Troshin, P. A., Light or Heat: What Is Killing Lead Halide Perovskites under Solar Cell Operation Conditions? *J. Phys. Chem. Lett.* **2020,** *11* (1), 333-339.

272. Vybornyi, O.; Yakunin, S.; Kovalenko, M. V., Polar-solvent-free colloidal synthesis of highly luminescent alkylammonium lead halide perovskite nanocrystals. *Nanoscale* **2016,** *8* (12), 6278-83.

273. Mosconi, E.; Azpiroz, J. M.; De Angelis, F., Ab Initio Molecular Dynamics Simulations of Methylammonium Lead Iodide Perovskite Degradation by Water. *Chemistry of Materials* **2015,** *27* (13), 4885-4892.

274. Lv, W.; Li, L.; Xu, M.; Hong, J.; Tang, X.; Xu, L.; Wu, Y.; Zhu, R.; Chen, R.; Huang, W., Improving the Stability of Metal Halide Perovskite Quantum Dots by Encapsulation. *Adv Mater* **2019,** *31* (28), e1900682.

275. Tan, C.; Chen, J.; Wu, X.-J.; Zhang, H., Epitaxial growth of hybrid nanostructures. *Nature Reviews Materials* **2018,** *3* (2).

276. de Mello Donega, C., Synthesis and properties of colloidal heteronanocrystals. *Chem Soc Rev* **2011,** *40* (3), 1512-46.

277. Toso, S.; Baranov, D.; Manna, L., Hidden in Plain Sight: The Overlooked Influence of the Cs^+ Substructure on Transformations in Cesium Lead Halide Nanocrystals. *ACS Energy Letters* **2020,** *5* (11), 3409-3414.

278. Sun, Q.; Ni, C.; Yu, Y.; Attique, S.; Wei, S.; Ci, Z.; Wang, J.; Yang, S., Design principle of all-inorganic halide perovskite-related nanocrystals. *Journal of Materials Chemistry C* **2018,** *6* (46), 12484-12492.

279. Bera, S.; Behera, R. K.; Das Adhikari, S.; Guria, A. K.; Pradhan, N., Equilibriums in Formation of Lead Halide Perovskite Nanocrystals. *J. Phys. Chem. Lett.* **2021,** *12* (49), 11824-11833.

280. Yoon, S. J.; Stamplecoskie, K. G.; Kamat, P. V., How Lead Halide Complex Chemistry Dictates the Composition of Mixed Halide Perovskites. *J. Phys. Chem. Lett.* **2016,** *7* (7), 1368-73.

281. Dutta, S. K.; Bera, S.; Pradhan, N., Why Is Making Epitaxially Grown All Inorganic Perovskite–Chalcogenide Nanocrystal Heterostructures Challenging? Some Facts and Some Strategies. *Chemistry of Materials* **2021,** *33* (11), 3868-3877.

282. Toso, S.; Baranov, D.; Manna, L., Metamorphoses of Cesium Lead Halide Nanocrystals. *Acc. Chem. Res.* **2021,** *54* (3), 498-508.

283. Shi, E.; Dou, L., Halide Perovskite Epitaxial Heterostructures. *Acc. Mater. Res.* **2020,** *1* (3), 213-224.

284. Imran, M.; Peng, L.; Pianetti, A.; Pinchetti, V.; Ramade, J.; Zito, J.; Di Stasio, F.; Buha, J.; Toso, S.; Song, J.; Infante, I.; Bals, S.; Brovelli, S.; Manna, L., Halide Perovskite-Lead Chalcohalide Nanocrystal Heterostructures. *J. Am. Chem. Soc.* **2021,** *143* (3), 1435-1446.

285. Tang, X.; Yang, J.; Li, S.; Liu, Z.; Hu, Z.; Hao, J.; Du, J.; Leng, Y.; Qin, H.; Lin, X.; Lin, Y.; Tian, Y.; Zhou, M.; Xiong, Q., Single Halide Perovskite/Semiconductor Core/Shell Quantum Dots with Ultrastability and Nonblinking Properties. *Adv. Sci. (Weinh)* **2019,** *6* (18), 1900412.

286. Chen, W.; Hao, J.; Hu, W.; Zang, Z.; Tang, X.; Fang, L.; Niu, T.; Zhou, M., Enhanced Stability and Tunable Photoluminescence in Perovskite $CsPbX_3$ /ZnS Quantum Dot Heterostructure. *Small* **2017,** *13* (21).

287. Zhu, J.; Yang, X.; Zhu, Y.; Wang, Y.; Cai, J.; Shen, J.; Sun, L.; Li, C., Room-Temperature Synthesis of Mn-Doped Cesium Lead Halide Quantum Dots with High Mn Substitution Ratio. *J. Phys. Chem. Lett.* **2017,** *8* (17), 4167-4171.

288. Ravi, V. K.; Markad, G. B.; Nag, A., Band Edge Energies and Excitonic Transition Probabilities of Colloidal $CsPbX_3$ (X = Cl, Br, I) Perovskite Nanocrystals. *ACS Energy Letters* **2016,** *1* (4), 665-671.

289. Su, Y.; Chen, X.; Ji, W.; Zeng, Q.; Ren, Z.; Su, Z.; Liu, L., Highly Controllable and Efficient Synthesis of Mixed-Halide CsPbX(3) (X = Cl, Br, I) Perovskite QDs toward the Tunability of Entire Visible Light. *ACS Appl. Mater. Interfaces* **2017,** *9* (38), 33020-33028.

290. Wang, D. H.; Wang, L.; Xu, A. W., Room-temperature synthesis of Zn(0.80)Cd(0.20)S solid solution with a high visible-light photocatalytic activity for hydrogen evolution. *Nanoscale* **2012,** *4* (6), 2046-53.

291. Oladeji, I. O.; Chow, L.; Ferekides, C. S.; Viswanathan, V.; Zhao, Z., Metal/CdTe/CdS/$Cd_{1-x}Zn_xS$/TCO/glass: A new CdTe thin film solar cell structure. *Solar Energy Materials and Solar Cells* **2000,** *61* (2), 203-211.

292. Yerok Park, D. H. S., Temperature-dependent Energy Transfer in Mn-dopedCdS-ZnS Nanocrystals. *BULLETIN OF THE KOREAN CHEMICAL SOCIETY* **2015**.

293. Srivastava, B. B.; Jana, S.; Pradhan, N., Doping Cu in semiconductor nanocrystals: some old and some new physical insights. *J. Am. Chem. Soc.* **2011,** *133* (4), 1007-1015.

294. Rumble, J. R., *CRC Handbook of Chemistry and Physics*. 99th Edition ed.; CRC Press/Taylor & Francis: **2018**.

295. Chakraborty, P.; Jin, Y.; Barrows, C. J.; Dunham, S. T.; Gamelin, D. R., Kinetics of Isovalent (Cd^{2+}) and Aliovalent (In^{3+}) Cation Exchange in $Cd_{1-x}Mn_xSe$ Nanocrystals. *J. Am. Chem. Soc.* **2016,** *138* (39), 12885-12893.

296. Zhang, J.; Di, Q.; Liu, J.; Bai, B.; Liu, J.; Xu, M.; Liu, J., Heterovalent Doping in Colloidal Semiconductor Nanocrystals: Cation-Exchange-Enabled New Accesses to Tuning Dopant Luminescence and Electronic Impurities. *J. Phys. Chem. Lett.* **2017,** *8* (19), 4943-4953.

297. Vetrone, F.; Boyer, J.-C.; Capobianco, J. A.; Speghini, A.; Bettinelli, M., Significance of Yb^{3+} concentration on the upconversion mechanisms in codoped $Y_2O_3:Er^{3+}$, Yb^{3+} nanocrystals. *Journal of Applied Physics* **2004,** *96* (1), 661-667.

298. Strohhöfer, C.; Polman, A., Relationship between gain and Yb^{3+} concentration in Er^{3+}–Yb^{3+} doped waveguide amplifiers. *Journal of Applied Physics* **2001,** *90* (9), 4314-4320.

299. Lee, W.; Oh, J.; Kwon, W.; Lee, S. H.; Kim, D.; Kim, S., Synthesis of Ag/Mn Co-Doped CdS/ZnS (Core/Shell) Nanocrystals with Controlled Dopant Concentration and Spatial Distribution and the Dynamics of Excitons and Energy Transfer between Co-Dopants. *Nano Lett* **2019,** *19* (1), 308-317.

300. Wang, C.; Xu, S.; Wang, Y.; Wang, Z.; Cui, Y., Aqueous synthesis of multilayer Mn:ZnSe/Cu:ZnS quantum dots with white light emission. *J. Mater. Chem. C* **2014,** *2* (4), 660-666.

301. Wang, C.; Xu, S.; Wang, Z.; Cui, Y., Key Roles of Impurities in the Stability of Internally Doped Cu:ZnSe Nanocrystals in Aqueous Solution. *J. Phys. Chem. C* **2011,** *115* (38), 18486-18493.

302. Xu, S.; Wang, C.; Wang, Z.; Zhang, H.; Yang, J.; Xu, Q.; Shao, H.; Li, R.; Lei, W.; Cui, Y., Aqueous synthesis of internally doped Cu:ZnSe/ZnS core-shell nanocrystals with good stability. *Nanotechnology* **2011,** *22* (27), 275605.

303. Jana, S.; Srivastava, B. B.; Pradhan, N., Correlation of Dopant States and Host Bandgap in Dual-Doped Semiconductor Nanocrystals. J. *Phys. Chem. Lett.* **2011,** *2* (14), 1747-1752.

304. Zheng, W.; Singh, K.; Wang, Z.; Wright, J. T.; van Tol, J.; Dalal, N. S.; Meulenberg, R. W.; Strouse, G. F., Evidence of a $ZnCr_2Se_4$ Spinel Inclusion at the Core of a Cr-Doped ZnSe Quantum Dot. *J. Am. Chem. Soc.* **2012,** *134* (12), 5577-5585.

305. Meulenberg, R. W.; van Buuren, T.; Hanif, K. M.; Willey, T. M.; Strouse, G. F.; Terminello, L. J., Structure and composition of Cu-doped CdSe nanocrystals using soft X-ray absorption spectroscopy. *Nano Lett.* **2004,** *4* (11), 2277-2285.

306. Liu, J.; Zhao, Q.; Liu, J.-L.; Wu, Y.-S.; Cheng, Y.; Ji, M.-W.; Qian, H.-M.; Hao, W.-C.; Zhang, L.-J.; Wei, X.-J.; Wang, S.-G.; Zhang, J.-T.; Du, Y.; Dou, S.-X.; Zhu, H.-S., Heterovalent-Doping-Enabled Efficient Dopant Luminescence and Controllable Electronic Impurity Via a New Strategy of Preparing II−VI Nanocrystals. *Adv. Mater.* **2015,** *27* (17), 2753-2761.

307. Catlow, C. R. A.; Chadwick, A. V.; Greaves, G. N.; Moroney, L. M., Direct observations of the dopant environment in fluorites using EXAFS. *Nature* **1984,** *312* (5995), 601-604.

Chun Chu

▪ 241 Lafayette Rd, Syracuse, NY 13205 ▪ (315) 395-6086 ▪ cchu06@syr.edu

Education

Ph.D. in Chemistry 2019 – 2024

Department of Chemistry, Syracuse university

M.S. in Chemistry 2007 - 2010

Beijing University of Chemical Technology, China

B.S. in Chemical Engineering 1999 - 2003

Shenyang University of Chemical Technology, China

Research/Working Experience

Research Assistant, Syracuse University 2020 - 2024

- Studied novel functional semiconductor nanomaterials by transition metal ion doping with enhanced optical properties for green energy applications.
- Developed an "atomic trap" strategy for site-specific doping by directional Mn dopant migration (*i.e.,* outward and inward) behavior in core/shell quantum dots.
- Dopant diffusion behavior in perovskite-based core/shell nanocrystals.

Application Scientist/Product Specialist, Shimadzu Scientific Instruments 2017 - 2018

- Developed new analytical methods of GC/MS and GC/MS/MS, including experimental design, method troubleshooting, data collection and interpretation in environmental, food, and material testing.

Application Scientist/Product Specialist, Polytech Instrument Ltd 2010 - 2017

- Developed analytical methods, and provided training for analytical instrument series, including GPC, SPE, GC/MS GC×GC-MS, potable MS, HPLC and peripheral products.
- Responsible in post-sale services and offering feedback to R&D department.

Scientist I, R&D Department, Lucky Film Ltd 2003 - 2007

- Designed, synthesized, and characterized new photosensitive materials.

Teaching/Mentoring Experience

Teaching Assistant (TA) in four different courses, Syracuse University 2019 – 2024

- CHE 422 Inorganic Laboratory Technique course (4 spring semesters, 2021 – 2024)
  - Developed course materials (lab manual, experiments, pre- and post-lab homework, *etc.*)
  - Provided mentorship and support for the inquiry-based labs and professional development.
  - Designed survey questions to quantitively evaluate on the impact of scaffolded, inquiry-based labs on course performance of senior undergraduate students.

- CHE 107 General Chemistry Lab I (Fall 2019)
    - Instructed general chemistry laboratories for non-chemistry undergraduate majors.
    - Provided individual and group instruction.
- CHE 117 General Chemistry Lab II (Spring 2020)
    - Presented experiments for non-chemistry undergraduate majors.
    - Provided individual and group instruction during the class and office hours.
- CHE 103 Chemistry in the Modern World (Fall 2020)
    - Provided support in lab preparation, equipment operations, troubleshooting, and experimental procedures.

Mentor, Dr. Weiwei Zheng group, Chemistry Department, SU 2020 – 2024

- Mentoring 1 undergraduate, 2 REU students, and 1 high school student.
    - Demonstrated and introduced experimental techniques (synthesis, characterization, device fabrication, *etc.*) in materials chemistry.
    - Provided mentorship for students in materials chemistry research.
    - Offered individual instruction on professional development/skills (graphing, report, and presentation).

Publications

1. **Chu, C.**; Hofman, E.; Gao, C.; Li, S.; Lin, H.; MacSwain, W.; Franck, J. M.; Meulenberg, R.W.; Chakraborty, A.; Zheng, W. Inserting an "Atomic Trap" for Directional Dopant Migration in Core/Multi-Shell Quantum Dots. *Chem. Sci.* **2023**, *14*, 14115-14123.
2. **Chu, C.**; Dewey, J.; Zheng, W. An Inorganic Chemistry Laboratory Technique Course using Scaffolded, Inquiry-Based Labs and Project-Based Learning. *J. Chem. Educ.* **2023**, *100*, 3500–3508.
3. Cai, T.; Shi, W.; Wu, R.; **Chu, C.**; Jin, N.; Wang, J.; Zheng, W. Wang, X.; Chen, O. Lanthanide Doping into All-Inorganic Heterometallic Halide Layered Double Perovskite Nanocrystals for Multimodal Visible and Near-Infrared Emission. *J. Am. Chem. Soc.* **2024**, *146*, 3200−3209.
4. Li, S.; Lin, H.; **Chu, C.**; Martin, C.; MacSwain, W.; Meulenberg R. W.; Franck, J. M.; Chakraborty, A.; Zheng, W. Interfacial B-Site Ion Diffusion in All-Inorganic Core/Shell Perovskite Nanocrystals. *ACS Nano.* **2023**, *17*, 22467–22477.
5. Lin, H.; Li, S.; Zhang, Y.; **Chu, C.**; MacSwain, W.; Meulenberg R. W.; Qiao, Q.; Zhao, D.; Zheng, W. Epitaxial Growth of Lead-Free Double Perovskite Shell for $CsPbX_3/Cs_2SnX_6$ (X = Cl, Br, and I) Core/Shell Perovskite Nanocrystals with Enhanced Photoelectric Properties and Stability. *Adv. Funct. Mater.* **2023**, 2309480.
6. Kim, S.; Kang, H. C.; **Chu, C.**; Li, S.; Yoo, K.; Wijethunga, U. K.; Zheng, W.; Yoo, C. G.; Sherman, B.; Lee, J.-J.; Leem. G. Solar Energy Driven C-C Bond Cleavage of Lignin with a D–π–A Organic Dye-Sensitized Photoanode. *Sustainable Energy Fuels,* **2023**, *7*, 2339-2348.

7. MacSwain, W.; Lin, H.; Li, Z. J.; Li, S.; **Chu, C.**; Dube, L.; Chen, O.; Leem, G.; Zheng, W. Facilitated Electron Transfer by Mn dopants in 1-Dimensional CdS Nanorods for Enhanced Photocatalytic Hydrogen Generation. *J. Mater. Chem. A*. **2023**, *11*, 7066-7076.
8. Saghy, P.; Brown, A. M.; **Chu, C.**; Dube, L.; Yang, H.; Zheng, W. Robinson, J. R.; Chen, O. Lanthanide Double Perovskite Nanocrystals with Emissions Covering the UV-C to NIR Spectral Range. *Adv. Opt. Mater.* **2023**, *11*, 2300277.
9. Davis, A. H.; Li, S.; Lin, H.; **Chu, C.**; Franck, J. M.; Leem, G.; Maye, M. M.; Zheng, W. Ligand-Mediated Synthesis of Chemically Tailored Two-Dimensional All-Inorganic Perovskite Nanoplatelets Under Ambient Conditions. *J. Mater. Chem. C.* **2021**, *9*, 14226-14235.
10. Xu, X.-Y.; Zhang, J.; Zhao, X.; Fu, H.; **Chu, C.**; Wang, P.; Wang, C.-C. Visible Light-Triggered Release of Sulfonamides in MOF/Ag-Based Nanoparticle Composites: Performance, Mechanism, and DFT Calculations. *ACS Appl. Nano Mater*. **2019**, *2*, 418-428.
11. Xu, X.-Y.; **Chu, C.**; Fu, H.; Du, X.-D.; Wang, P.; Zheng, W.; Wang, C.-C. Light-Responsive UiO-66-NH_2/Ag_3PO_4 MOF-Nanoparticle Composites for the Capture and Release of Sulfamethoxazole. *Chem. Eng. J.* **2018**, *350*, 436-444.
12. Liu, A.; Wang, C-Z.; **Chu, C.**; Chu, H-Y.; Chen, X.; Du, A.-F.; Mao, J.; Zheng, W.; Wang, C.-C. Adsorption performance toward organic pollutants, odor control and anti-microbial activities of one Ag-based coordination polymer. *Journal of Environmental Chemical Engineering* **2018**, *6*, 4961-4969.
13. **Chu, C.**; Wang, Z. Dynamics of difenoconazole residues in celery and soil. *Sci Sin Chim*. **2011**, *41(1)*, 136-142.

Presentations

1. **Chu, C.**; Zheng, W. Inserting an ‘atomic trap’ for directional dopant migration in core/multi-shell quantum dots, Oral presentation, The 6th Binghamton University Conference in Undergraduate and Graduate Chemistry Research, November 11, **2023**.
2. Vanshika; **Chu, C.**; Zheng, W. Retention and diffusion behavior of Cu dopants in core/shell QDs, Poster presentation, The 6th Binghamton University Conference in Undergraduate and Graduate Chemistry Research, November 11, **2023**.
3. **Chu, C.**; Zheng, W. Inserting an ‘atomic trap’ for directional dopant migration in core/multi-shell quantum dots, Oral presentation, ACS NERM 2022 meeting, October 4, **2022**.
4. **Chu, C.** The application of automatic sample pretreatment and sample injection in the food detection, Oral presentation, The Proceedings of the 3rd China safety testing technology and quality control of food and agricultural products Forum, China, **2014**.
5. **Chu, C.** The application of the GPC & SPE technology in the food analysis, Oral presentation, The Proceedings of the Beijing conference and exhibition on instrumental analysis, China, **2013**.
6. **Chu, C.**; Wang B. Phthalic acid esters detection in oil samples by GPC, Oral presentation, The Proceedings of the 12th chromatography congress Of Gansu, China, **2012**.

Honors and Awards

- 2024 *Outstanding Teaching Assistant Award*. Syracuse University, **2024**.
- *2023 Summer Dissertation Fellowship.* Syracuse University, **2023**.
- *Nominee of 2022-2023 Syracuse University Graduate Student Employee of the Year award*. Syracuse University, **2023**.
- *William D. Johnson Award for Outstanding Graduate Teaching Assistant*. Department of Chemistry, Syracuse University, **2022**.

Extracurricular activities

- **Event organizer** of “Materials chemistry behind table tennis” section for the *Sustainable Material Summer Workshop* in the department of chemistry at SU and SUNY-ESF for local high school students, April 20-21, **2024**.
- **Event organizer** of “Materials chemistry behind table tennis” section for the *Sustainable Material Summer Workshop* in the department of chemistry at SU and SUNY-ESF for local high school students, May 5-6, **2023**.
- **Volunteer** for the *Sustainable Material Summer Workshop* in the department of chemistry at SU and SUNY-ESF for local high school students, May 21 – 22, **2022**.
- **Laboratory instructor** of “Synthesis of perovskite nanomaterials” section for the *Sustainable Material Summer Workshop* in the department of chemistry at SU and SUNY-ESF for local high school students, June 28 – 29, **2021**.